Celestial and Underground Searches for Heavy Dark Matter

by

Javier Fernandez Acevedo

A thesis submitted to the

Department of Physics, Engineering Physics & Astronomy

in conformity with the requirements for

the degree of Doctor of Philosophy

Queen's University

Kingston, Ontario, Canada

April 2022

Abstract

This thesis investigates new signatures of heavy and composite dark matter models in both astrophysical objects and underground experiments. The first two chapters are dedicated to heavy dark matter phenomenology in compact stars: white dwarfs and neutron stars. The high density of these objects makes them prime targets for pushing the frontier of dark matter detection. We first explore how dark matter accumulation can lead to Type-Ia supernova explosions in white dwarfs, and what the overall timescale is for this ignition mechanism to proceed. The existence of massive white dwarfs that have not exploded then implies constraints on dark matter interactions with nuclei and electrons. In particular, we map these constraints to specific dark photon and Higgs portal models to illustrate their reach. We then proceed to show how the thermal evolution of old neutron stars can place leading bounds on dark matter interactions with nucleons, based on the additional energy from dark matter scattering and annihilation in their crusts. We also argue that neutron stars might be the only feasible way to detect inelastic dark matter with large mass splittings, such as the supersymmetric Higgsino. The third and final chapter, is devoted to new signatures of heavy composite dark matter states at both celestial objects and underground experiments. We show how a simple composite model with Yukawa couplings to the Standard Model can be detectable through the ionization tracks they would produce at direct detection experiments, as well as thermal radiation and induced nuclear reactions at neutrino observatories. Remarkably, these signatures arise even for extremely weak couplings, below any existing experimental or astrophysical constraints. We also discuss how these composite states could explode white dwarfs upon transit, or substantially heat planets as they accumulate in their core.

Acknowledgments

These past few years, I have been very fortunate of being surrounded by many especial and talented people.

First and foremost, I want to thank my supervisor, Joe Bramante, for the endless support, engaging discussions and solid advising throughout my doctoral studies. The encouragement he has given me is invaluable, especially for pursuing my own research ideas, and has allowed me to grow as an independent physicist. Without Joe's guidance, this thesis could not have been achieved. I cannot express how grateful I am for having been under his supervision.

It is a pleasure to thank the many wonderful people I have had the privilege to work with: Amit Bhoonah, Yilda Boukhtouchen, Alan Goodman, Joachim Kopp, Rebecca Leane, Toby Opferkuch and Nirmal Raj. All of you have made me a better physicist than I could ever hope for. I must also thank Aaron Vincent and Larry Widrow, for the many enlightening discussions I have had with them these past years.

I am thankful to Amit Bhoonah, Fede Brera and Hicham Benmansour, for making my graduate studies here so fun and memorable. I thank my parents for encouraging me to pursue a career in science. Last but not least, I am forever grateful to my girlfriend, Julieta Conti, for her unconditional love and support that kept me going throughout these years.

Statement of Co-Authorship

I hereby declare that this thesis contains material that is the result of collaborative research, and is detailed as follows,

- Chapter 2 is based on the publication: *J. Acevedo & J. Bramante, Supernovae Sparked by Dark Matter in White Dwarfs, Phys. Rev. D 100, 043020 (2019).* This project was devised by Joseph Bramante, based on his prior work. I ran the initial computations on dark matter ignition of supernovae via elastic nuclear scattering. Compared to previous results, I also added a structure function to account for a reduction in the dark matter scattering rate due to the crystalline structure of white dwarf stars. Joseph Bramante, in addition, investigated how evaporating black holes made of dark matter could ignite Type-Ia supernovae, as well as ran multiple numerical checks of my results.

- Chapter 3 is based on the publication: *J. Acevedo, J. Bramante, R. Leane & N. Raj, Warming Nuclear Pasta with Dark Matter: Kinetic and Annihilation Heating of Neutron Star Crusts, JCAP03(2020)038.* This project was based on earlier work by Joseph Bramante and Nirmal Raj (and additional collaborators not named here). I computed the dark matter capture and thermalization rates for a benchmark neutron star, ran initial estimates for the sensitivity of crustal heating by dark matter based on these rates, and wrote a preliminary version of the article. Joseph Bramante, Rebecca Leane and Nirmal Raj analyzed the case of dark matter annihilation heating in the crust. Rebecca Leane investigated how the neutron star crust sensitivity compares to various direct detection experiments, as well as how these predictions change with the neutron star properties. Nirmal Raj calculated how infrared telescopes could discern crustal heating from core heating by dark matter in an old neutron star, and added those results to the final version of the paper. Both Rebecca Leane and Nirmal Raj significantly improved the quality of the initial manuscript I wrote and ran valuable numerical checks.

- Chapter 4 is based on the publications: *J. Acevedo, J. Bramante & A. Goodman, Nuclear Fusion inside Dark Matter, Phys. Rev. D 103, 123022 (2021)*; and the follow-up work, *J. Acevedo, J. Bramante & A. Goodman, Accelerating Composite Dark Matter Discovery with Nuclear Recoils and the Migdal Effect, Phys. Rev. D 105, 023012 (2022)*. These publications are based on a novel idea I had on composite dark matter signatures via 5th force couplings to the Standard Model. Joseph Bramante provided valuable guidance on all my calculations, as well as investigated a generalized cosmological synthesis for the composite states that included dilution stages. Alan Goodman ran several numerical checks of all my calculations and estimated the capture rate of these composite states in the Earth.

Statement of Originality

I hereby certify that all of the work described within this thesis is the original work of the author. Any published (or unpublished) ideas and/or techniques from the work of others are fully acknowledged in accordance with the standard referencing practices.

Javier Fernandez Acevedo,

March 2022

Contents

List of Figures

Chapter 1

Introduction

For decades now, it has been established that the majority of the matter content of the Universe is made of an invisible substance that does not absorb nor emit light, *dark matter* [1]. Its existence is inferred from the gravitational interactions it has with visible matter: as early as the 1940s, the motion of galaxies in large clusters could only be explained by large amounts of undetected mass that provided additional gravitational binding. Later on, measurements of galaxy rotation curves indicated the presence of non-luminous matter within galaxies, which vastly surpassed the amount of visible mass they contained. Gravitational lensing in clusters have further supported the existence of dark matter. Finally, observations of the large-scale structure, and the fluctuations Cosmic Microwave Background, cemented the dark matter paradigm. Today, the dark matter abundance is estimated to be in an approximate 5:1 ratio relative to its visible counterpart.

Although theories of modified gravity also attempted to explain these phenomena, such models never successfully accounted for all the observations. Their most significant failures are the observed fluctuations in the Cosmic Microwave Background, which cannot be accounted for without introducing some form of dark matter, and the dynamics of the Bullet Cluster: a collision of galaxy clusters that, through gravitational lensing measurements of background objects, reveals a clear separation between its visible matter, in the form of x-ray emitting gas, and the total mass content responsible for the lensing, favouring the presence of large amounts of non-luminous matter. Moreover, there are significant reasons to assume that the matter content of the Universe goes beyond ordinary nuclei and electrons, which fall within the Standard Model of particle physics. Several unsolved issues of the Standard Model indicate the need for new physics, such as the strong charge-parity (CP) problem, the generation of neutrino masses, the origin of the matter-antimatter asymmetry, and the hierarchy problem. On the other hand, the particles that are currently known cannot account for all the dark matter content. At present, the only Standard Model particle that is massive, neutral and stable is the neutrino, however this particle species is too fast to explain the dark matter structures observed in the Universe. It is reasonable then to assume that dark matter must be predominantly composed of one or more undiscovered particles, and has non-gravitational interactions with the visible sector as well as potentially with itself.

1.1 The Quest for Dark Matter

Although a large amount of evidence pointing at the existence of dark matter has been collected, still very little is known about its most fundamental properties, such as mass, cosmological origin and non-gravitational interactions [2]. The discovery of dark matter, and its ultimate impact on the evolution of our Universe, has become one of the most pressing challenges of modern physics.

A myriad of dark matter models have been proposed to address this problem, and they can be classified in several ways. In terms of production, dark matter could be a thermal relic, initially in thermal equilibrium with the primordial bath of Standard Model particles, but later froze-out as the Universe expanded [3, 4, 5, 6]; or it could have been slowly produced by decays or annihilation of Standard Model particles in a freeze-in scenario [7, 8, 9, 10, 11]. Freeze-out, for example, could have occurred in the presence of an asymmetry between dark particle and antiparticle states, leading to asymmetric dark matter. This asymmetry could share a common origin with the baryon asymmetry in the early Universe [12, 13]. Alternatively, both particle and antiparticle states could be in equal abundance, in a symmetric dark matter scenario. Other production mechanisms such as phase transitions [14, 15, 16, 17] or gravitational production [18, 19] also remain open. At the end of production, dark matter could be a fundamental particle, or a larger composite object, in similar way to nucleons, nuclei and atoms being bound states of smaller constituents [20]. The non-gravitational couplings of dark matter with the Standard Model could be realized through known interactions, like the weak force, or could be mediated by new particles, the so-called "hidden-sector" dark matter theories, see *e.g.* [21] and references therein.

Perhaps most remarkably of all, the mass range of potential candidates spans almost a hundred orders of magnitude, ranging from ultra-light bosons that collectively behave as waves within galaxies, to weakly interacting massive particles at the electroweak scale, to black holes of primordial origin with masses far heavier than the Sun. For this thesis, we will primarily focus on heavy dark matter which, roughly speaking, can be considered to have masses of order $\gtrsim$ 10 - 100 TeV, above the existing production reach of the largest particle accelerators and unitarity limits for dark matter annihilation in the early universe. As we discuss here, the latter can be overcome in several ways.

Because of this large disparity in the masses of viable candidates, a gigantic experimental effort is required to constrain, discover, or rule out, all the different dark matter theories. A comprehensive review of all the detection strategies would be out of scope. Instead, we limit ourselves to provide a brief overview on various dark matter detection methods that are underway or planned. Below, we discuss the progress and challenges of searches both in terrestrial experiments as well as searches using astrophysical systems as probes for dark matter.

1.2 Terrestrial Searches

A plethora of detectors have been designed, constructed and operated to look for various dark matter candidates. Direct detection experiments, defined as those that look for dark matter interacting against some target material, are at the vanguard of sensitivity [22]. Although initially these experiments were primarily commissioned to look for the well-motivated weakly interacting massive particles, the mass range of their searches has been significantly expanded.

In particular, deep underground detectors based on liquid noble elements, such as the XENON Dark Matter Search (XENON-1T) [23, 24, 25], the Dark matter Experiment with Argon and Pulse-shape discrimination (DEAP-3600) [26, 27], the Large Underground Xenon Experiment (LUX) [28, 29, 30], the Particle and Astrophysical Xenon Detector (PandaX) [31, 32], and the Depleted Argon cryogenic Scintillation and Ionization Detection (DarkSide-50) [33], have probed extremely small cross sections in a wide dark matter mass range. The next-generation of some of these experiments is already underway, and will likely probe cross sections comparable to that of neutrino-nucleus scattering, *i.e.* the so-called neutrino floor [34, 35]. These experiments, however, are limited in the low mass range, for which transiting dark matter particles cannot impart enough energy and momentum to be detected. For such light masses, instead, detectors based on dark matter exciting low-energy collective modes in condensed matter systems, such as the Super Cryogenic Dark Matter Search (SuperCDMS) [36, 37, 38] and the Cryogenic Rare Event Search with Superconducting Thermometers (CRESST) [39, 40, 41], dominate in sensitivity, and several additional proposals are actively being designed and tested. Other interesting detection methods, that utilize advances in quantum metrology, have recently surfaced. For example, the Windchime project aims at observing the transit of ultra-heavy dark matter particles via their gravitational interactions triggering a large array of accelerometers [42].

Additionally, particle colliders, such as the Large Hadron Collider (LHC) [43], and fixed-target experiments, like the planned Light Dark Matter Experiment (LDMX) [44, 45], significantly contribute to the quest for dark matter. For instance, dark matter could be produced by the decay of particles like the Higgs boson in high energy collisions, and the reconstruction of missing momenta in these collisions can pinpoint these invisible decays [46, 47, 48]. Other searches with jets and visible recoils have also been extensively discussed in the literature, see *e.g.* [49, 50].

1.3 Astrophysical and Cosmological Searches

Several collaborations have searched for indirect dark matter signals in astrophysical systems and cosmological observables, complementing the searches discussed above [51, 52]. In fact, indirect detection may be the only feasible way to discover heavier dark matter candidates. Experiments that search for direct interactions of dark matter with their target material are ultimately limited by the overall flux of dark matter passing through them, whereas production in particle accelerators is limited by their total energy.

Dark matter could annihilate or decay to high-energy photons, neutrinos or charged cosmic rays, and a plethora of collaborations are actively looking for these signals with ground- and space-based detectors. To name a few, observatories like the X-ray Multi-Mirror Mission (XMM-Newton) [53, 54, 55], the International Gamma-ray Astrophysics Laboratory (INTEGRAL) [56, 57, 58], the Imaging Compton Telescope (COMPTEL) [59, 60] and the Fermi Large Area Telescope (Fermi-LAT) [61, 62, 63] have extensively searched for diffuse x-ray and gamma-ray signals from dark matter; experiments like Super-Kamiokande [64, 65], IceCube [66, 67, 68, 69], and the Astronomy with a Neutrino Telescope and Abyss Environmental Research (ANTARES) [70, 71, 72] have performed searches for neutrino signals; and the Payload for Anti-Matter Matter Exploration and Light-Nuclei Astrophysics (PAMELA) [73, 74] as well as the Alpha Magnetic Spectrometer (AMS-02) [75, 76] detectors have probed dark matter signals in the form of antimatter cosmic rays. In fact, numerous excesses, potentially associated with dark matter, have been reported and are still actively investigated [77]. Gravitational wave observatories like the Laser Interferometer Gravitational-wave Observatory (LIGO) and the Virgo Experiment [78, 79, 80] have also opened up new searches for dark matter, such as mergers of dark compact objects or primordial black holes. With more precise instruments devised for the future, it is likely that some of these searches will soon make new breakthroughs.

The new era of precision cosmology we have entered has also allowed to look for tiny dark matter imprints in various observables. The decay or annihilation of dark matter could produce spectral distortions, or alter the anisotropies of the Cosmic Microwave Background, potentially detectable with instruments like Planck [81, 82, 83] or the planned Primordial Inflation Explorer (PIXIE) [84]. Large-scale surveys, such as the Dark Energy Survey (DES) [85], can test our models of how structures of dark matter form in the early universe. In the near future, the redshifted 21-cm line of neutral hydrogen will allow us to probe dark matter interactions with baryonic matter during the cosmic dawn. Radio interferometers like the Hydrogen Epoch of Reionization Array (HERA) [86], the Murchinson Widefield Array (MWA) [87], or the Square Kilometer Array (SKA) [88, 89], promise to open a new observation window into this epoch.

Finally, all the above searches are overlapped with an increasing amount of research into the potential impact of dark matter on celestial objects: planets, brown dwarfs, main-sequence and red giant stars, white dwarfs and neutron stars all could capture dark matter in their interiors. This would lead to a variety of signatures, such as substantial heating through the deposition of kinetic energy by dark matter particles, stellar transients, or even the implosion of these objects from dark matter-made black holes in their interior. An overview of these search strategies can be found in *e.g.* [90, 51] (see also the various references cited throughout this document). The constraints on dark matter inferred from measuring the various properties of these astrophysical probes are, at times, competitive or even more stringent than direct detection experiments.

1.4 Structure of this Thesis

In this thesis, we will review new signatures of dark matter in compact stars as well as underground experiments. The first two chapters are dedicated to (mostly) heavy dark matter signatures in white dwarfs and neutron stars. We show how the high density of these objects allows for substantial capture of dark matter in their interiors. Even for small cross sections between the dark matter and Standard Model particles, dark matter capture in these objects could result in high-energy signatures: white dwarfs may explode as Type-Ia supernovae from dark matter accumulation, and old neutron stars may become anomalously hot from the dark matter that constantly falls onto them at semi-relativistic speeds. As we argue here, such phenomenology has the potential to either be detected in the near future, or else place competitive constraints on dark matter interactions with the visible sector. In the third and final chapter, we review novel composite dark matter signatures that have been recently uncovered. This new phenomenology manifests when the attractive force that bounds dark matter particles together is also coupled to Standard Model nuclei. Composite dark matter states that are heavy enough source an attractive force so strong that, upon transiting matter, could recoil nuclei to high energies. We show how this effect has optimistic detection prospects at direct detection experiments and large neutrino observatories, as well as discuss its implications for astrophysical systems.

Throughout this document, unless otherwise specified, we employ natural units whereby the speed of light (c), the reduced Planck constant ($\hbar$), and the Boltzmann constant (k_b) are set to unity, *i.e.* $c = \hbar = k_b = 1$. The gravitational constant (G) is set to $G = M_{pl}^{-2}$, where $M_{pl} \simeq 1.2 \times 10^{19}$ GeV is the non-reduced Planck mass. To illustrate better our results, some final quantities are scaled back to cgs or mks units, but preserving electron-volts as the basic energy unit, *e.g.* power is converted from GeV^2 to GeV s^{-1} by the end of a computation. Another quantity frequently quoted here is a solar mass, which reads $M_\odot \simeq 1.1 \times 10^{57}$ GeV in natural units.

Chapter 2

Exploding White Dwarfs with Dark Matter

Due to their high density and strong magnetic fields, yet simple structure, white dwarfs have long been predilect astroparticle laboratories. These objects are the endpoints of stellar evolution for progenitor masses $\lesssim 10\ M_\odot$, and have typical masses 0.5 - $1.4 M_\odot$, radii 6000 - 3000 km, and densities of order 10^6 - 10^9 g cm^{-3} at their core. Their composition is predominantly carbon and oxygen, which are fully ionized at such high pressures, and the free electrons, through their degeneracy, provide the stabilizing pressure against gravitational collapse of the star.

In particular, various works have investigated the impact of dark matter and other new physics on these compact objects. A remarkable property that makes white dwarfs stand out, compared to other astrophysical probes, is the fact that those close to the Chandrasekhar limit ($\simeq 1.4 M_\odot$, where $M_\odot$ is a solar mass) are highly explosive: any localized energy deposition can rapidly burn carbon and oxygen in their interior, generating a thermonuclear runaway reaction that disrupts the star, producing the Type-Ia supernovae that we observe and have used, for instance, to measure the expansion rate of the universe.

The exact ignition mechanism for these explosions is a matter of active research.

Contrary to prior expectations, recent evidence has suggested that many Type-Ia supernovae proceed from white dwarfs with masses below the Chandrasekhar mass threshold [91, 92]. Although ignition channels have been proposed to address this, such as matter accretion from a neighbouring star [93, 94, 95], binary mergers [96, 97] or helium shell ignition [98], these require binary companions, whereas some astronomical evidence indicates that Type-Ia supernovae arise from lone white dwarfs [99, 100]. In this context, various works have demonstrated that dark matter may be the cause behind a fraction of sub-Chandrasekhar Type-Ia supernovae. Proposed dark matter Type-Ia supernova ignition channels include formation and collapse of asymmetric dark matter cores [101, 102, 103], evaporation to Hawking radiation of light black holes formed from collapsed dark matter [102, 103], heavy dark matter annihilation or decay to Standard Model particles [104], pycnonuclear reactions catalyzed by the capture of charged massive particles [105], as well as the transit of primordial black holes [106, 107] or massive composite dark matter blobs [108, 109]. Here, we will review the detailed analysis of Ref. [102] on the ignition of Type-Ia supernovae via asymmetric dark matter capture followed by collapse. In Chap. 4, we will also review ignition via the transit of large composite dark matter states.

2.1 Supernova Ignition by Dark Matter

The asymmetric dark matter ignition scenario proceeds as follows: first a large quantity of dark matter accumulates inside the white dwarf over time, by scattering against nuclei or electrons within it. As the dark matter settles inside the white dwarf after repeated scatters, it will thermalize at the white dwarf's internal temperature, leading to the formation of a thermalized dark matter sphere near the center of the white dwarf. This dark matter sphere grows in mass as more dark matter is accreted and thermalized; a matter sphere composed of asymmetric dark matter [13, 12] will grow quickly, since asymmetric dark matter particles do not self-annihilate. Once such a dark matter sphere acquires a critical mass necessary for self-gravitation, its subsequent gravitational collapse releases enough energy through nuclear elastic scattering to dramatically heat the core of white dwarf stars. This heating prompts a thermonuclear runaway reaction that precedes a Type Ia supernova. The particular dynamics of dark matter accumulation and ignition have consequences for Type Ia supernova observations; intriguingly, [101] showed that the observed inverse correlation [110, 92] between Type Ia host galaxy age and Type Ia light curve stretch (and by extension a correlation to white dwarf progenitor masses [92]), could be accounted for with asymmetric dark matter, which would tend to ignite less heavy white dwarfs at later times.

Here, we explore new aspects of the dark matter Type-Ia supernova ignition mechanism, and set new bounds on the dark matter-nucleon cross section for heavy dark matter. These bounds depend on four relevant physical quantities: 1) the time it takes to accumulate a critical mass of dark matter in the center of the white dwarf, 2) the time it takes for the accreted dark matter to reach thermal equilibrium and settle to the center of the white dwarf, 3) the time it takes the dark matter sphere to collapse, 4) the energy transferred during dark matter collapse through scattering against stellar constituents. We set bounds on dark matter interactions by requiring that the first three processes take longer than the age of a known white dwarf, which has not exploded. To determine which white dwarf sets the most stringent bound, we have used the Montreal White Dwarf Database [111], and found that white dwarf

SDSS J160420.40+055542.3, a 3.3 Gyr old, $\sim 1.4 M_\odot$ mass white dwarf provides the strongest constraint; other combinations of white dwarf mass and age are detailed in Ref. [102], along with a proposal to use white dwarfs in old globular clusters to set more stringent bounds.

Besides igniting Type-Ia supernovae during collapse, we will show that, for a dark matter sphere that collapses without igniting the white dwarf, the black hole formed from the collapsed dark matter may itself ignite the white dwarf via Hawking radiation. The possibility that white dwarfs could be ignited via black hole evaporation was first mentioned in Ref. [104], which studied the ignition of white dwarfs via Standard Model particle showers produced in the decay and annihilation of very massive dark matter particles in white dwarfs. Here, we will find that in a similar fashion, small evaporating black holes formed from collapsed dark matter cores can ignite a white dwarf. This evaporative ignition will occur for dark matter heavier than $\sim 10^{11}$ GeV; such dark matter is heavy enough to collapse after a modest amount of dark matter has accumulated. This can result in the formation of a small black hole that evaporates within a few billion years.

The evaporation of this black hole will lead to Type-Ia supernova ignition via Hawking radiation, provided evaporation of the black hole occurs faster than accretion of stellar material and additional dark matter particles, because the black hole must become tiny enough for the Hawking radiation to reach temperatures suitable for ignition. For dark matter that ignites white dwarfs via black hole evaporation, the time that it takes for the dark matter sphere to collapse and form the black hole, is the limiting factor determining the constraint on dark matter interactions. We also find some region of the parameter space where the black hole formed grows, eventually leading to the destruction of the white dwarf, without producing a Type Ia supernova event – such an eventuality for white dwarf stars was first considered in Ref. [112].

2.1.1 Heavy Asymmetric Dark Matter Capture

Dark matter heavier than about $m_X \gtrsim 10^6$ GeV will require multiple scatters as it crosses the white dwarf, in order to slow down to sub-escape velocity. Once this happens, the dark matter particle becomes gravitationally bound to the white dwarf, following closed orbits and crossing it periodically, losing more energy in the process (see below). The rate at which dark matter particles are gravitationally captured, in this multi-scatter regime, has been computed for compact stars in Ref. [113], and we provide full details of this calculation in App. A. All the results reported in [102], and subsequently presented here, were obtained using the full capture rate given by Eq. (A.2). However, to give a sense of scale, we provide in the main text an approximate dark matter capture rate for a close-to-threshold ^{12}C white dwarf of mass $M \simeq 1.4 M_\odot$ and radius $R \simeq 2500$ km,

$$\dot{m}_X \approx \mathrm{Min}\left[3 \times 10^{27}\ \mathrm{GeV\ s^{-1}}, 6 \times 10^{24}\ \mathrm{GeV\ s^{-1}} \left(\frac{10^8\ \mathrm{GeV}}{m_X}\right)\left(\frac{\sigma_{nX}}{10^{-42}\ \mathrm{cm}^2}\right)\right] \times \left(\frac{\rho_X}{0.3\ \mathrm{GeV\ cm^{-3}}}\right)\left(\frac{10^{-3}}{\bar{v}}\right), \tag{2.1}$$

where this expression assumes a conservatively low, 2σ allowed dark matter halo density of $\rho_X \simeq 0.3$ GeV cm^{-3} [114], and a characteristic dark matter velocity of $\bar{v} \simeq 10^{-3}$. This approximate capture rate provides a reasonable estimate for the time it takes for the critical mass of dark matter to be captured without major computational challenges, see App. A for more details.

For ease of reference, it is convenient to introduce at this point the definition of optical depth, which is the ratio between the dark matter cross section and the saturation value for which dark matter scatters about once per star crossing,

$$\tau(\sigma_{aX}) = \frac{3\sigma_{aX}}{2\pi R^2 m_a} \tag{2.2}$$

where $m_a \simeq 12$ GeV for a pure carbon white dwarf, and R denotes its radius. In the limit of $m_X \gg m_a$, the cross section σ_{aX} is in turn written in terms of a per-nucleon cross section σ_{nX} through the relation,

$$\sigma_{aX} \simeq A^4 S(q) F^2(\langle E_R \rangle)\ \sigma_{nX}, \tag{2.3}$$

where the function F is the Helm form factor [115, 116] evaluated at the average nuclear recoil energy $\langle E_R \rangle$, see App. A for details. For dark matter capture, this is about 1 MeV, however it can substantially change during each stage of the ignition process. The Helm form factor accounts for the effects of nuclear substructure at large momentum transfers compared to the inverse nuclear radius. The additional function $S(q)$ denotes the static structure function of the white dwarf lattice, which evaluates to unity for dark matter capture, but becomes relevant as dark matter loses further energy, see below.

2.1.2 Dark Matter Thermalization

After it becomes captured and gravitationally bound, a dark matter particle will orbit through the white dwarf star, losing more kinetic energy in successive scatters.

Thermalization of the captured dark matter occurs in two stages: a stage where the dark matter orbits outside the star and a stage where it orbits entirely inside the star. Some aspects of dark matter thermalization inside a white dwarf will differ from dark matter thermalization in a main sequence star, studied in [112].

2.1.2.1 First Thermalization

In the initial thermalization stage, the dark matter particles follow a closed orbit that intersects the white dwarf, losing kinetic energy through scattering while transiting the star. Upon capture, assuming a radial path, a dark matter particle will have a turning point r as a function of energy given by

$$r = -\frac{GMm_X}{E}, \tag{2.4}$$

where $E < 0$ is the particle's initial energy after capture. The average energy loss when a dark matter particle scatters against a nucleus at a distance $\tilde{r}$ from the star center, in the kinematic limit $m_a \ll m_X$, will be

$$\Delta E = 2\frac{m_a}{m_X}\left(E + GMm_X\left(\frac{3R^2 - \tilde{r}^2}{2R^3}\right)\right), \tag{2.5}$$

where the whole factor in parenthesis is the dark matter kinetic energy, *i.e.* it is the sum of the particle's initial energy E and the potential energy inside the star. We introduce the energy loss per scatter averaged over one stellar transit ΔE_{tr}, by expressing the dark matter total energy E in terms of the turning point r using (2.4) and averaging over the star size,

$$\Delta E_{tr} = 2GMm_a \left(-\frac{1}{r} - \frac{1}{R} \int_0^R \frac{3R^2 - \tilde{r}^2}{2R^3}\, d\tilde{r} \right), \tag{2.6}$$

$$\Delta E_{tr} = 2GMm_a \left(\frac{4}{3R} - \frac{1}{r} \right). \tag{2.7}$$

The time it takes the dark matter to complete one orbit through the white dwarf is approximately the orbital period for a dark matter-white dwarf orbital radius (semi-major axis) r,

$$\Delta t_{tr} = 2\pi r^{3/2}/\sqrt{M}, \tag{2.8}$$

where the initial size of dark matter's orbit around the white dwarf, r_0 can be determined from the captured dark matter's initial kinetic energy, $r_0^{-1} \simeq \bar{v}^2/2GM$. Finally, the average energy loss during the first thermalization phase is obtained by dividing Eq. (2.7) by Eq. (2.8) and multiplying by the white dwarf optical depth τ to estimate the average number of times that the dark matter scatters as it completes a single transit through the white dwarf.

$$\frac{dE_{tr}}{dt_{tr}} = \frac{(GM)^{3/2}\tau m_a}{\pi r^{3/2}} \left(\frac{4}{3R} - \frac{1}{r} \right). \tag{2.9}$$

It is useful to make the variable substitution $\epsilon = R/r$, where this is approximately the ratio of the dark matter's initial kinetic energy GMm_X/r to its binding energy at the surface of the star GMm_X/R. The time for the dark matter to settle inside the star after repeated scatters is

$$t_1^{th} \simeq \frac{\pi m_X R^{3/2}}{\sqrt{GM} m_a} \int_{\epsilon_0}^{\epsilon_f} \frac{d\epsilon}{\tau \epsilon^{3/2} \left(\frac{4}{3} - \epsilon\right)}, \tag{2.10}$$

where the initial ratio is $\epsilon_0 \simeq R/r_0$ and the final ratio is $\epsilon_f \simeq 1$ when the dark matter lies inside the star. Note that in the above expression the optical depth τ, and by extension the dark matter-nuclear cross section σ_{aX} depend on energy, because of the Helm form factor shown in Eq. (A.4). Therefore, we have conservatively taken the Helm form factor in $\tau(\sigma_{aX})$ to be $F^2(\langle E_R \rangle) \sim 0.5$, which is its minimum value for dark matter-nuclear recoil energies during the first stage of thermalization. The recoil energies involved are still too high in this early thermalization stage for the microscopic white dwarf structure to become relevant, we leave its discussion for the following section. Inserting typical white dwarf parameters, the time to complete the first stage of thermalization, after which the dark matter particle will orbit entirely inside the star, is given by

$$t_1^{th} \lesssim 10^{-4} \text{ yrs} \left(\frac{10^{-40} \text{ cm}^2}{\sigma_{nX}}\right) \left(\frac{m_X}{10^6 \text{ GeV}}\right) \left(\frac{1.4 M_\odot}{M}\right)^{\frac{3}{2}} \left(\frac{R}{2500 \text{ km}}\right)^{\frac{7}{2}}. \tag{2.11}$$

2.1.2.2 Second Thermalization

During a second thermalization stage, the dark matter particles orbit entirely inside the white dwarf. As the dark matter particles move through the star interior, repeated scattering shrinks their orbits to a "thermal radius" r_{th}. At this radius, they have a thermal velocity distribution determined by the white dwarf core temperature T. We will now see that the structure of the star plays a critical role in this process.

At standard densities and temperatures for old massive ($\gtrsim M_\odot$) white dwarfs, atoms are completely ionized and electrons can be treated as a uniform free gas providing a neutralizing background for nuclei. Such a plasma, under high pressure and low temperature, solidifies to form a Coulomb crystal. We are considering old white dwarfs that have not exploded, with core temperatures $T \sim 10^7$ K that lie below the melting temperature of the plasma $T_m \sim 5 \times 10^8$ K [117, 118]. Therefore, we must consider a structure factor that accounts for dark matter scattering in a dense crystalline medium [119].

The structure factor of Coulomb crystals has been calculated in [120, 121]. It is normally split into two contributions corresponding to elastic Bragg scattering, and inelastic absorption or emission of phonons,

$$S(q) = S'(q) + S''(q) \tag{2.12}$$

For completeness, we first present the elastic part $S'(q)$, which will not be essential for our analysis. The elastic part is written as [119],

$$S'(q) = e^{-W(q)}(2\pi)^3 n_a \sum_{\mathbf{G}\neq\mathbf{0}} \delta(\mathbf{q} - \mathbf{G}), \tag{2.13}$$

where $\mathbf{G}$ represents the reciprocal lattice vectors, *i.e.* all nonzero vectors pointing between nuclei, $n_a = \rho_{wd}/m_a$ is the nucleus number density and $W(q)$ is the Debye-Waller factor. The Debye-Waller factor, which as we will see also appears in the inelastic structure factor, can be approximated by $W(q) \simeq \langle r_T^2 \rangle q^2/3$, where $\langle r_T^2 \rangle$ is the mean-squared nucleus displacement at a given temperature T [119]. We can estimate the mean-squared displacement by assuming each nucleus is bound by a harmonic oscillator potential, with its natural frequency given by the plasma frequency $\Omega_p^2 =$

$4\pi\rho_{wd}Z^2e^2/m_a^2$, and summing over all normal modes per ion [122],

$$\langle r_T^2 \rangle \simeq \frac{14T}{m_a\Omega_p^2}. \tag{2.14}$$

Using $q^2 = 2m_a^2E/m_X$, we conveniently recast $W(q) = E/E_{sup}$, where

$$E_{sup} \simeq \frac{Z^2e^2m_X\rho_{wd}}{Tm_a^3}, \tag{2.15}$$

is the approximate energy scale at which dark matter nuclear scattering becomes suppressed. The Bragg scattering contribution $S'(q)$ evaluates exactly to zero when the momentum transfer roughly falls below the inverse nuclear spacing $a^{-1} = (4\pi\rho_{wd}/3m_a)^{1/3}$. The sharp peaks of $S'(q)$ have a height $\lesssim 1$ close to this threshold value and quickly decay for higher momentum transfers due to the exponential suppression $e^{-W(q)}$. Because the second thermalization time will be predominantly determined by inelastic phonon scattering, the precise form of the elastic Bragg component, and its peaks around $q \sim |\mathbf{G}|$, will have a negligible contribution to the computations that follow.

The inelastic, phonon emission and absorption portion of the structure factor can be approximated by

$$S''(q) \simeq 1 - e^{-W(q)} = 1 - e^{-E/E_{sup}}. \tag{2.16}$$

This approximation is accurate when $q \gtrsim 3/a$ [121]. It also reproduces correct limits such that $S(q) \to 0$ and $S(q) \to 1$ when $q \to 0$ and $q \to \infty$ respectively. To our knowledge, this structure factor has not been accounted for in any previous work considering dark matter scattering with nuclei in white dwarfs. Here, to get a first estimate, we will exclusively apply Eq. (2.16) to account for low momentum suppression of scattering, since in the high momentum exchange limit $S(q) \simeq 1$, and can be safely neglected. On the other hand, for low momentum exchange we will find that the inclusion of the $S''(q)$ phonon structure factor results in much longer thermalization times, since momentum transfer to nuclei decreases and becomes comparable to the nuclear spacing as dark matter thermalizes.

To compute the energy loss rate, first we consider the dark matter-nucleus interaction time t_{aX},

$$t_{aX} = \frac{1}{n_a \sigma_{aX} v_{rel}}, \tag{2.17}$$

and the average energy loss per scatter, in the limit that $m_a \ll m_X$,

$$\Delta E = \frac{2m_a}{m_X} E, \tag{2.18}$$

where E is the energy of the dark matter particle and v_{rel} is the relative velocity of dark matter-nucleus system. Thus, the energy loss rate is expressed as

$$\frac{dE}{dt} = \frac{2\rho_{wd}\sigma_{aX} v_{rel} E}{m_X}. \tag{2.19}$$

After completing the first thermalization phase, dark matter particles will have an initial energy given by the binding energy at the surface of the star $\sim GMm_X/R$. For energies above E_{sup}, they are in an inertial regime where $v_{rel} \sim \sqrt{2E/m_X}$, *i.e.* their velocity dominates the scattering time t_{aX} [103]. In such inertial regime, the energy loss rate is

$$\left(\frac{dE}{dt}\right)_{in} = \frac{\rho_{wd}A^4(1-e^{-E/E_{sup}})\sigma_{nX}}{m_X}\sqrt{\frac{2E}{m_X}}E \approx \frac{\sqrt{2}\rho_{wd}A^4\sigma_{nX}E^{3/2}}{m_X^{3/2}}. \tag{2.20}$$

In the above expression, we have conservatively set $F^2(\langle E_R\rangle) \sim 0.5$ for the recoil energies involved. When the energy drops below E_{sup}, dark matter particles enter the viscous regime where scattering rate is now dominated by the thermal speed of nuclei, which we estimate[1] as $v_{rel} \sim v_{nuc} \sim \sqrt{T/m_a}$. In this new viscous regime, the energy loss rate is

$$\left(\frac{dE}{dt}\right)_{vis} = \frac{2\rho_{wd}A^4(1-e^{-E/E_{sup}})\sigma_{nX}}{m_X}\sqrt{\frac{T}{m_a}}E \approx \frac{2\rho_{wd}A^4\sigma_{nX}\sqrt{T}E^2}{m_X\sqrt{m_a}E_{sup}}, \tag{2.21}$$

where now the Helm form factor can be set to unity for the low recoil momenta. Throughout the remainder of this Chapter, we shall assume $m_a \simeq 12$ GeV, $A = 12$ and $Z = 6$ for ^{12}C nuclei. After entering the viscous regime with an approximate energy E_{sup}, the dark matter energy is reduced over time to the thermal value $E \simeq 3T/2$. We find that the time required for dark matter to reach this thermal energy in the viscous regime to be several orders of magnitude larger than the time spent in the inertial regime. Such time is estimated by integrating (2.21),

$$\begin{aligned} t_2^{th} &\simeq \frac{m_X\sqrt{m_a}E_{sup}}{2\rho_{wd}A^4\sigma_{nX}\sqrt{T}}\int_{E_{sup}}^{3T/2}\frac{dE}{E^2} \simeq \frac{m_X E_{sup}\sqrt{m_a}}{3T^{3/2}\rho_{wd}A^4\sigma_{nX}} \\ &\simeq 20 \text{ yrs}\left(\frac{10^{-40}\text{ cm}^2}{\sigma_{nX}}\right)\left(\frac{m_X}{10^6\text{ GeV}}\right)^2\left(\frac{10^7\text{ K}}{T}\right)^{\frac{5}{2}} \end{aligned} \tag{2.22}$$

[1]A more appropriate estimate is $v_{nuc} \simeq \sqrt{\Omega_p/m_a}$, since the above approximation assumes the equipartition theorem for white dwarf nuclei is applicable. However, the two expressions differ by an $\sim \mathcal{O}(1)$ factor, with the above expression yielding a more conservative result, *i.e.* longer explosion times and smaller cross sections constrained.

We remark that for typical white dwarf parameters and dark matter masses considered in this work, the time to complete the first phase of thermalization is negligible compared to the second phase. The minimum cross section for completing the first and second thermalization stages within 3 Gyrs are plotted in Fig. 2.1.

2.1.3 Dark Matter Collapse

After being captured and thermalized through repeated scatterings with white dwarf particles, the dark matter particles settle into a gravitationally bound configuration. The radius of this thermalized sphere of dark matter in the center of the white dwarf, r_{th}, can be computed using the virial theorem, equating the dark matter thermal energy at temperature T with the dark matter's gravitational potential energy inside a white dwarf with density ρ_{wd}

$$r_{th} = \sqrt{\frac{9T}{4\pi G \rho_{wd} m_X}} \simeq 30 \text{ m} \left(\frac{10^6 \text{ GeV}}{m_X}\right)^{\frac{1}{2}} \left(\frac{10^9 \text{ g cm}^{-3}}{\rho_{wd}}\right)^{\frac{1}{2}} \left(\frac{T}{10^7 \text{ K}}\right)^{\frac{1}{2}} \tag{2.23}$$

Unless the dark matter is asymmetric [13, 12], or equivalently has very small self-annihilation interactions [123], the dark matter sphere will be prohibited from substantially growing by annihilation. Therefore, throughout this work we will consider asymmetric dark matter that does not possess self-annihilation interactions.

Dark matter collected into a sphere of radius r_{th} at the center of the white dwarf will collapse under its own weight, so long as two criteria are met:

1. Dark matter must be self-gravitating, so that its gravitational binding energy decreases during collapse. If the gravitational potential of the white dwarf is much larger than the dark matter's self-gravity, then the binding energy of the

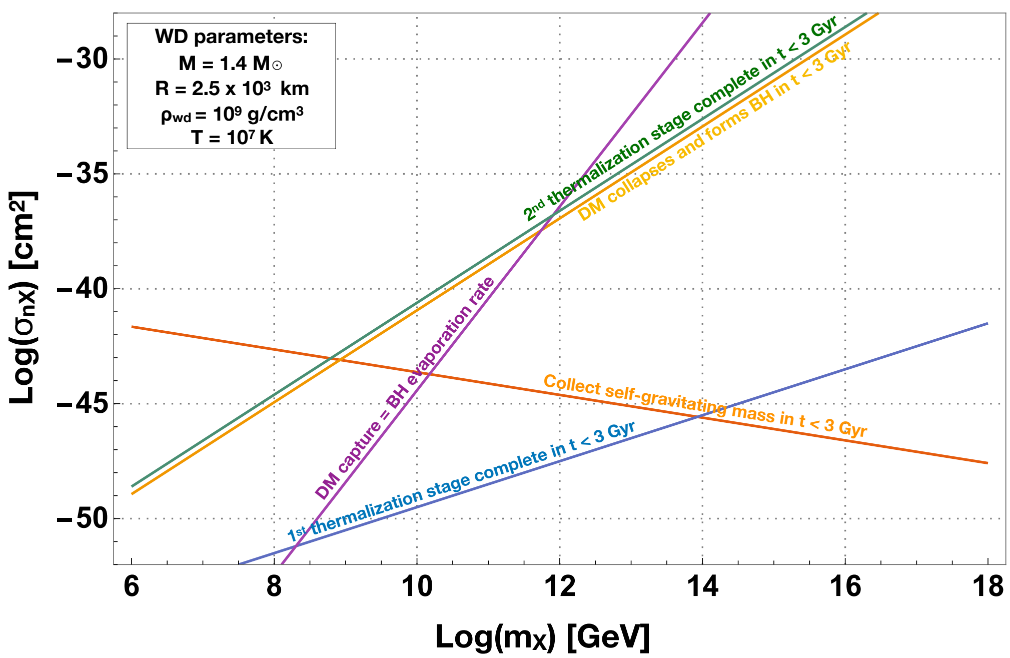

Figure 2.1: Minimum dark matter-nucleon cross section σ_{nX} as a function of m_X, in a log-log plot, for dark matter to thermalize with the white dwarf (green and blue) and accumulate critical mass for self-gravitation (orange) within 3 Gyrs. The minimum cross section for the thermalized dark matter sphere to collapse to a black hole (yellow) within 3 Gyrs, and for dark matter accumulation to preclude complete black hole evaporation (purple) are also shown. A dark matter halo density $\rho_X \simeq 0.3$ GeV/cm^3 at the location of the white dwarf is assumed. The upper-left box shows the white dwarf parameters used, where the mass and age of the white dwarf were determined by the oldest massive white dwarf in the Montreal White Dwarf Database [111], SDSS J160420.40+055542.3.

dark matter sphere with mass M_X has the form of a harmonic oscillator potential, $E \sim -GM_X\rho_{wd}r_{th}^2$. Under the influence of the white dwarf's gravitational potential alone, the dark matter sphere's potential energy would increase as the dark matter sphere shrank in size. As a consequence, without self-gravitation, the minimum energy configuration of the dark matter sphere will be at radius r_{th}, and collapse will not occur. Therefore, we require the density of the dark matter sphere to roughly exceed the white dwarf density, in order for collapse to occur.

2. The dark matter sphere must satisfy a Jeans instability condition.

The first self-gravitation condition is met so long as the dark matter density equals or exceeds the white dwarf density within the thermalization radius, r_{th}. This defines a critical self-gravitating mass $M_{crit} = 4\pi\rho_{wd}r_{th}^3/3$. The number of dark matter particles required is

$$N_{sg} = \frac{M_{crit}}{m_X} \simeq 6 \times 10^{37} \left(\frac{10^6 \text{ GeV}}{m_X}\right)^{\frac{5}{2}} \left(\frac{10^9 \text{ g cm}^{-3}}{\rho_{wd}}\right)^{\frac{1}{2}} \left(\frac{T}{10^7 \text{ K}}\right)^{\frac{3}{2}}. \tag{2.24}$$

In Fig. 2.1, the minimum dark matter-nucleon cross section required to collect a self-gravitating clump of dark matter in a white dwarf in 3 Gyrs is shown.

To determine whether the dark matter sphere is unstable, we perform a simple Jeans mass analysis, requiring that the sound-crossing time exceed the free-fall time of the dark matter sphere. The free-fall time is given by

$$t_{ff} = \sqrt{\frac{3\pi}{32G\rho_X}} \simeq 0.03 \text{ s} \left(\frac{10^9 \text{ g cm}^{-3}}{\rho_{wd}}\right)^{\frac{1}{2}} \left(\frac{r}{r_{th}}\right)^{\frac{3}{2}} \tag{2.25}$$

Where ρ_X is the density of the dark matter sphere which will be greater than the white dwarf density after collapse begins. The rightmost expression is obtained when $\rho_X = \rho_{wd}$, *i.e.* when enough dark matter has been collected to achieve self-gravitation.

The sound-crossing time, on the other hand, is given by the time a sound wave crosses the radius of the dark matter sphere. In a standard Jeans mass collapse analysis, if the sound-crossing time is longer than the free-fall time, a gravitationally bound configuration of gas will be unstable to small perturbations and will collapse.

A self-thermalized dark matter sphere will have a short sound-crossing time. For our purposes, we will consider the dark matter sphere to be self-thermalized, since such a sphere will be most stabilized against collapse. If the dark matter is self-thermalized, it will have a sound speed given by, $c_X \sim \sqrt{T/m_X}$. In such case,

$$t_{sound} = \frac{r}{c_X} \lesssim \frac{r_{th}}{c_X} \simeq 0.10 \text{ s} \left(\frac{10^9 \text{ g cm}^{-3}}{\rho_{wd}}\right)^{\frac{1}{2}}, \tag{2.26}$$

By setting $r = r_{th}$, we have assumed that the dark matter sphere has just reached the point of self-gravitation, *i.e.* that it has the same density as the white dwarf. Comparing to Eq. (2.25), the sound-crossing time for a self-thermalized dark matter sphere turns out to be longer than the free-fall time for a self-gravitating sphere of dark matter, for the white dwarf parameters considered here. For lighter and correspondingly less dense white dwarfs and particular dark matter models, which will be treated in future work, it will be necessary to determine whether additional dark matter must be captured to satisfy the Jeans criterion.

Before continuing, we briefly consider two relevant timescales: the time between dark matter self-interactions, and the time between dark matter interactions with nuclei, prior to collapse. For much of the dark matter model space considered, the free-fall time in Eq. (2.25) is longer than the time it takes for a dark matter particle to interact with another dark matter particle, just prior to collapse,

$$\begin{aligned} t_{XX} &= \frac{1}{n_X \sigma_{XX} \sqrt{T/m_X}} = \frac{m_X}{\rho_{wd} \sigma_{XX} \sqrt{T/m_X}} \\ &\simeq 0.04 \text{ s} \left(\frac{10^{-30} \text{ cm}^2}{\sigma_{XX}}\right) \left(\frac{m_X}{10^6 \text{ GeV}}\right)^{\frac{3}{2}} \left(\frac{10^9 \text{ g cm}^{-3}}{\rho_{wd}}\right) \left(\frac{10^7 \text{ K}}{T}\right)^{\frac{1}{2}} \end{aligned} \tag{2.27}$$

where $n_X = \rho_{wd}/m_X$ is the dark matter number density just before collapse and σ_{XX} is the dark matter self-interaction cross-section. This shows that, in order for the dark matter to be self-thermalized on timescales faster than the collapse timescale, its self-interaction cross section must exceed $\sim 10^{-30}$ cm^2. In Sec. 2.2 we will see that this condition is fulfilled for some explicit vector- and scalar-portal dark matter models.

At the onset of collapse, the time it takes for dark matter to interact with a nucleus in the white dwarf is

$$\begin{aligned} t_{aX} &= \frac{1}{n_a \sigma_{aX} v_{nuc}} \simeq \frac{3 m_a T}{2 \rho_{wd} A^4 E_{sup} \sigma_{nX} \sqrt{2 E_{sup}/m_a}} \\ &\simeq 10 \text{ s} \left(\frac{10^{-40} \text{ cm}^2}{\sigma_{nX}} \right) \left(\frac{m_X}{10^6 \text{ GeV}} \right)^{\frac{3}{2}} \left(\frac{10^7 \text{ K}}{T} \right)^{\frac{5}{2}} \end{aligned} \tag{2.28}$$

where we conservatively set the Helm form factor to unity in σ_{aX}, and also evaluated the structure factor (2.16) at the thermal energy $3T/2$ of the dark matter. Comparing this to the free-fall time t_{ff}, we see that the above Jeans instability requirement was justified in neglecting dark matter-nuclear interactions.

The capture rate, thermalization rate, and conditions for dark matter collapse, all depend on the dark matter-nucleon cross section. Using the Montreal White Dwarf Database [111], we find that most of the single white dwarfs in the mass range $1.2 M_\odot < M < 1.4 M_\odot$ have cooling ages that lie below 3 Gyrs. The oldest $M \sim 1.4 M_\odot$ white dwarf present in the sample has an age of approximately 3.3 Gyrs. Therefore, we will conservatively constrain the cross section by requiring both thermalization and accumulation of the critical mass to be completed within 3 Gyrs. Fig. 2.1 summarizes the minimum cross section in a log-log plot for all relevant processes to be completed for an $M \sim 1.4 M_{\odot}$ white dwarf of typical parameters within that time.

2.1.4 Ignition via Coherent Dark Matter-Nucleus Scattering

Once the dark matter sphere begins to implode it will scatter with nuclei as it collapses, and can transfer enough energy to heat a small central region of the white dwarf to the point that nuclear fusion begins, resulting in a Type Ia supernova explosion [101]. The major requirements for dark matter ignition via elastic scattering during dark matter collapse are as follows

1. The dark matter must heat the white dwarf faster than it cools (mostly via electron conduction cooling).
2. The dark matter must heat a portion of the white dwarf to a critical temperature (around 10^{10} K).

Below we will find that for dark matter elastically scattering with nucleons, satisfying the first criterion guarantees satisfying the second.

2.1.4.1 Dark matter heating versus white dwarf cooling

To begin, we note that Helm form factor coherence drops for higher energy scatters of dark matter against nuclei, whereas the structure factor, Eq. (2.16), evaluates to unity. As the dark matter sphere collapses, the dark matter will move faster and faster, resulting in higher energy collisions. This allows us to determine a collapse radius past which dark matter energy transfer via elastic scattering with nuclei becomes suppressed (as we will see, the Helm form factor becomes relevant in this fashion for dark matter masses $m_X \gtrsim 10^8$ GeV). In future work, energy transfer via high energy dark matter-nucleus inelastic scattering may be considered; here we conservatively require that dark matter ignite white dwarfs during collapse purely through elastic scattering.

First, we calculate the velocity of the dark matter particles in the collapsing sphere, assuming a homogeneous density profile and applying the virial theorem

$$v_{vir} = \sqrt{\frac{3}{5}\frac{GN_{sg}m_X}{r}} \simeq 6 \times 10^{-7} \left(\frac{10^6 \text{ GeV}}{m_X}\right)^{\frac{3}{4}} \left(\frac{10^9 \text{ g cm}^{-3}}{\rho_{wd}}\right)^{\frac{1}{4}} \left(\frac{T}{10^7 \text{ K}}\right)^{\frac{3}{4}} \left(\frac{r_{th}}{r}\right)^{\frac{1}{2}} \tag{2.29}$$

The Helm form factor, on the other hand, begins to suppress energy exchanges at speeds $v \sim 0.02$. Combining this with the previous expression, we obtain a radius at which the energy transferred per dark matter-nuclear collision begins decreasing,

$$r_{min} \simeq 10^{-5} \text{ cm } \left(\frac{10^6 \text{ GeV}}{m_X}\right)^{\frac{3}{2}} \left(\frac{10^9 \text{ g cm}^{-3}}{\rho_{wd}}\right)^{\frac{1}{2}} \left(\frac{T}{10^7 \text{ K}}\right)^{\frac{3}{2}}. \tag{2.30}$$

We will use this radius as a benchmark collapse position, for which the dark matter elastic scattering energy transfer to white dwarf nuclei is maximized.

To determine whether dark matter sparks nuclear fusion that leads to a Type Ia supernova, we follow the analysis of [124, 101] and require the heating of a central mass of carbon and oxygen to a certain critical temperature T_c. Because the dark matter sphere encloses a small radius, we will mostly consider the heating of a microgram ($1\ \mu$g) mass sample of white dwarf material composed of predominantly ^{12}C nuclei. As determined in [124], a microgram of white dwarf material must be heated to a temperature $T_c \sim 10^{10}$ K (~ 1 MeV) in order to spark a supernova. This amount of white dwarf material will be enclosed in a radius

$$r_{\mu g} \simeq 7 \times 10^{-6} \text{ cm} \left(\frac{10^9 \text{ g cm}^{-3}}{\rho_{wd}} \right)^{\frac{1}{3}}. \tag{2.31}$$

For dark matter heavier than $m_X \gtrsim 10^6$ GeV, we see that the radius of maximum coherent elastic scattering heating r_{min} is smaller than the radius that encloses a microgram of white dwarf material; hence it will be convenient to simply consider how much the dark matter heats a microgram of white dwarf material. For $m_X \lesssim 10^6$ GeV, where $r_{\mu g} < r_{min}$, we have independently verified that that the cross-section required for dark matter to accumulate to a critical mass within $\sim$ 3 Gyrs, is sufficient to prompt Type Ia ignition, see also Ref. [101]. Therefore, we consider dark matter collapsing to radius r_{min}, which is smaller than the radius enclosing a microgram sample. For high dark matter masses, $m_X \gtrsim 10^8$ GeV, we will also see how increasing the dark matter-nucleon cross section beyond the cross section required to accumulate a critical mass of dark matter, allows for ignition during collapse. Compared to prior results in [101], this will improve the cross section bound obtained.

To determine the cross section required to ignite the sample, we analyze four relevant quantities: the energy transfer rate of the dark matter sphere to nuclei via elastic scattering $\dot{Q}_{DM}$, the conduction rate at which the white dwarf sample cools down $\dot{Q}_{\text{cond}}$, the heat capacity of the white dwarf sample C_v, and the latent heat absorbed Q_{lat} when the white dwarf material melts from heating.

To calculate the energy transfer rate, we first consider the average energy exchange between a dark matter particle and a nucleus of mass m_a in a single scatter. In the limit $m_a \ll m_X$ this energy exchange is simply $\Delta E \simeq m_a v_{vir}^2$. Using the time it takes for a dark matter particle to interact with a nucleus t_{aX}, we write the energy transfer rate as

$$\dot{Q}_{DM} = \frac{N_{sg}\ \Delta E}{t_{aX}} \simeq 10^{37}\ \text{GeV s}^{-1}\ \left(\frac{\sigma_{nX}}{10^{-40}\ \text{cm}^2}\right)\left(\frac{10^6\ \text{GeV}}{m_X}\right)^{\frac{5}{2}}\left(\frac{\rho_{wd}}{10^9\ \text{g cm}^{-3}}\right)^{\frac{1}{2}}\left(\frac{T}{10^7\ \text{K}}\right)^{\frac{3}{2}} \tag{2.32}$$

The rightmost expression has been evaluated when $v_{vir} \approx 0.02$, *i.e.* when the energy transfer rate is approximately at its maximum before becoming suppressed by the Helm form factor. At such point, the scattering rate is dominated by the dark matter velocity, so the dark matter-nucleus scattering time is also evaluated as $t_{aX} = (n_a \sigma_{aX} v_{vir})^{-1}$. The structure factor given by Eq. (2.16), on the other hand, evaluates to unity at such high energy exchanges. We note that $\dot{Q}_{DM}$ decreases with m_X. For higher dark matter masses, fewer particles need to be captured for the dark matter sphere to self-gravitate and collapse, so the resulting collapsing dark matter sphere will have fewer particles scattering with nuclei.

Next, we consider the rate at which heat is diffused out of the sample. The conductive diffusion rate of a white dwarf material sphere of radius r_s at temperature T_s is given by [122]

$$\dot{Q}_{\text{cond}} = \frac{4\pi^2 T_s^3 (T_s - T_{wd})\ r_s}{15 \kappa_c \rho_{wd}} \simeq 10^{25}\ \text{GeV s}^{-1}\ \left(\frac{\rho_{wd}}{10^9\ \text{g cm}^{-3}}\right)^{\frac{4}{15}} \tag{2.33}$$

Where $\kappa_c \sim 10^{-9}\ \text{cm}^2\ \text{g}^{-1}\ (T_c/10^7\ \text{K})^{2.8}\ (10^9\ \text{g cm}^{-3}/\rho_{wd})^{1.6}$ is the conductive opacity of the white dwarf, which for densities above $\sim 10^7\ \text{g cm}^{-3}$ is dominated by relativistic electron conduction [125, 101]. In (2.33), $T_{wd} \sim 10^7$ K denotes the core equilibrium temperature. On the right hand side of Eq. (2.33), we have set $T_s = T_c$ and $r_s = r_{\mu g}$ to indicate the scaling of the diffusion rate $\dot{Q}_{\text{cond}}$, since diffusion will be maximized at the highest temperatures. Put another way, the choice $T_s = T_c$ yields the highest possible diffusion rate for the sample of white dwarf material just before reaching the ignition point.

In order to be ignited, the dark matter must heat the white dwarf faster than it can cool itself. The sample of white dwarf material can be ignited so long as the energy transfer rate (2.32) exceeds the diffusion rate (2.33),

$$\dot{Q}_{DM} > \dot{Q}_{\rm cond}. \tag{2.34}$$

This condition ensures that the white dwarf material can be heated to 10^{10} K, given the conductive electron diffusion in the white dwarf. For dark matter with a mass in the range $m_X \sim 10^8$ - 3×10^{12} GeV, Eq. (2.34) places the most stringent restriction on the dark matter-nucleon cross section. This is because, for dark matter masses below $m_X \sim 10^8$ GeV, the cross section on nucleons required to accumulate a self-gravitating mass of dark matter is sufficient to prompt white dwarf ignition when the dark matter sphere collapses. On the other hand, for dark matter masses above $m_X \sim 3 \times 10^{12}$ GeV, ignition via black hole evaporation is guaranteed, as will be explained shortly in Sec. 2.1.5.2. For dark matter in the mass range $m_X \sim 10^8$ - 3×10^{12} GeV, the ignition cross section increases with higher dark matter masses, since fewer dark matter particles will compose the collapsing dark matter sphere (see Eq. (2.24)), and therefore, the overall rate for dark matter scattering against nuclei declines, resulting in a lower energy transfer rate for a fixed dark matter-nucleon scattering cross section. Consequently, the constraint on the cross section associated with ignition has a positive slope.

We make the following remark about possible quantum mechanical effects: comparing the mean de Broglie wavelength of the dark matter particles $\lambda_{dB} = 1/m_X v_{vir}$

to the mean dark matter particle separation $\sim r/N_{sg}^{1/3}$, we find that the dark matter sphere must collapse to a radius

$$r_{qm} \simeq \frac{1}{G m_X^3 N_{sg}^{1/3}} \simeq 10^{-6}\ \mathrm{cm}\ \left(\frac{10^6\ \mathrm{GeV}}{m_X}\right)^{\frac{13}{6}} \left(\frac{\rho_{wd}}{10^9\ \mathrm{g\ cm^{-3}}}\right)^{\frac{1}{6}} \left(\frac{10^7\ \mathrm{K}}{T}\right)^{\frac{1}{2}}, \quad (2.35)$$

in order for quantum mechanical effects to become relevant. This radius is much smaller than either r_{min} or the Schwarzchild radius in the case of black hole evaporative ignition (see below), for the dark matter masses considered here. Therefore, we do not consider the effects of fermion degeneracy or boson condensation in the dynamical collapse of dark matter inside the white dwarf.

2.1.4.2 Dark matter collapse and heating to critical temperature

To determine the total amount that dark matter heats the white dwarf, we first determine the timescale for dark matter to collapse to r_{min}. We compute this by integrating the ratio between the rate at which the dark matter sphere sheds gravitational energy and the rate at which energy is transferred to the white dwarf. Collapse of the dark matter sphere will be again divided in two regimes, depending on whether the energy of the dark matter particles lies above or below the suppression scale E_{sup}. During the initial stages of collapse, dark matter is moving very slowly resulting in low momentum transfers and a high suppression of nuclear interactions, as we saw above. Dark matter exits this regime when it has collapsed to a radius

$$r_{sup} \simeq \frac{G N_{sg} m_X^2}{E_{sup}} \simeq 10^{-3}\ \mathrm{cm} \left(\frac{10^6\ \mathrm{GeV}}{m_X}\right)^{\frac{3}{2}} \left(\frac{10^9\ \mathrm{g/cm^3}}{\rho_{wd}}\right)^{\frac{3}{2}} \left(\frac{T}{10^7\ \mathrm{K}}\right)^{\frac{5}{2}}, \quad (2.36)$$

such that the nuclear scattering suppression is lost. We note that $r_{min} \ll r_{sup} \ll r_{th}$ always across the parameter space under consideration. Once the dark matter sphere collapses to r_{sup}, it will continue to collapse at a much faster rate. We find the collapse timescale to be determined by the time spent during this first regime, which we obtain by integrating Eq. (2.21) from an initial energy $GN_{sg}m_X^2/r_{th}$ to an energy $GN_{sg}m_X^2/r_{sup}$,

$$t_{col} \simeq \frac{\sqrt{m_a}E_{sup}r_{th}}{2\sqrt{T}GN_{sg}m_X\rho_{wd}A^4\sigma_{nX}} \simeq 10 \text{ yrs} \left(\frac{10^{-40} \text{ cm}^2}{\sigma_{nX}}\right)\left(\frac{m_X}{10^6 \text{ GeV}}\right)^2\left(\frac{10^7 \text{ K}}{T}\right)^{\frac{5}{2}} \tag{2.37}$$

In the rightmost expression, we have set the Helm form factor to unity. The minimum cross section for the dark matter sphere to collapse within 3 Gyrs is identical to that required for completing the second thermalization phase, and is displayed in Fig. 2.1.

The final requirement for ignition we now address, is that enough total energy should be transferred to the white dwarf material, so that it is heated to a temperature of 10^{10} K [124]. We will see that sufficient ignition heating for a microgram of white dwarf is guaranteed for the dark matter masses and cross sections we consider, so long as Eq. (2.34) is satisfied. The heat capacity of the sample is largely governed by the heat capacity of the degenerate white dwarf's ion lattice [122],

$$C_v = \frac{3}{2}\left(\frac{4}{3}\pi r_{\mu g}^3 n_a\right) \simeq 746 \text{ GeV K}^{-1}. \tag{2.38}$$

Note that in our treatment the heat capacity does not scale with the core density, since we have fixed the sample mass to 1 μg. Then the total energy that has to be imparted to a microgram of white dwarf material is simply $C_v T_c \sim 10^{13}$ GeV.

The critical temperature for ignition lies above the melting temperature $T_m \sim 8.5 \times 10^8$ K of the white dwarf material, so we must also consider the latent heat absorbed when the microgram material undergoes a solid-liquid phase transition. The amount of latent heat absorbed in the case of heating a microgram of white dwarf material is

$$Q_{lat} \simeq T_m \left(\frac{4}{3} \pi r_{\mu g}^3 n_a \right) \simeq 6 \times 10^{11} \text{ GeV} \tag{2.39}$$

We see that dark matter ignition of the white dwarf is not limited by the amount of potential energy the dark matter has available to be transferred: both Q_{lat} and $C_v T_c$ are much smaller than either $\dot{Q}_{DM}$ or $\dot{Q}_{\text{cond}}$ multiplied by the collapse timescale over which dark matter potential energy is transferred.

We make one final comment on the ignition of Type Ia supernovae by coherent dark matter-nucleus scattering. It has been noted that many deflagration and detonation models of ignition [126], require that the heated white dwarf material to have a temperature profile with a high degree of homogeneity. The time scale for energy diffusion is

$$t_{\text{cond}} = \frac{\kappa_c \rho}{r_{\mu g} T_c^3} \simeq 1.4 \times 10^{-28} \text{ s } \left(\frac{10^9 \text{ g cm}^{-3}}{\rho_{wd}} \right)^{2.27} \tag{2.40}$$

We note that t_{cond} is shorter than the time scale for energy transfer to the white dwarf material. This shows that energy diffusion within the microgram sample is sufficiently fast to ensure an homogeneous temperature profile of the sample during the heating process.

2.1.5 Ignition via Microscopic Black Hole Evaporation

We now consider the possibility that the dark matter sphere collapses to form a black hole, which then ignites the white dwarf as it evaporates into Hawking radiation. This will occur for heavier dark matter, for a fixed dark matter-nucleon cross-section, since the number of dark matter particles and the power transferred to the white dwarf both decrease as the dark matter mass m_X increases, *cf.* Eq. (2.32). We also analyze the parameter space region in which the black hole formed does not evaporate, but rather grows by accretion of both dark matter and stellar material, eventually consuming the white dwarf.

2.1.5.1 Black hole formation from collapsing dark matter

The mass of dark matter required to form a black hole will depend on the spin of the dark matter field and its self-couplings [127, 128, 129]. In the case of a Higgs portal dark matter model examined in Sec. 2.2, the dark matter self-interactions are attractive and do not preclude the black hole formation. Self-interactions via a vector boson present a more complex case, as they can be either attractive or repulsive. In the absence of a detailed study of these interactions, we conservatively use the maximum mass stabilized against non-relativistic gravitational collapse by Fermi-degeneracy pressure for dark matter fermions

$$M_{BH,min}^{ferm} = \frac{M_{pl}^3}{m_X^2} \simeq 2 \times 10^{37}\ \text{GeV} \left(\frac{10^{10}\ \text{GeV}}{m_X}\right)^2 \tag{2.41}$$

and the maximum mass stabilized against non-relativistic gravitational collapse by quantum pressure for bosons with an order unity quartic self-coupling ($\lambda_\phi \sim 1$ for

$V(\phi) \supset \lambda_\phi \phi^4$) [127]

$$M_{BH,min}^{boson} = \frac{\sqrt{\lambda_\phi} M_{pl}^3}{m_X^2} \simeq 2 \times 10^{37} \text{ GeV} \left(\frac{10^{10} \text{ GeV}}{m_X} \right)^2 \left(\frac{\lambda_\phi}{1} \right)^{\frac{1}{2}} . \tag{2.42}$$

Comparing these minimum black hole masses to the mass required for dark matter to self-gravitate obtained from Eq. (2.24),

$$M_{crit} \simeq 6 \times 10^{37} \text{ GeV} \left(\frac{10^{10} \text{ GeV}}{m_X} \right)^{\frac{3}{2}} \left(\frac{10^9 \text{ g cm}^{-3}}{\rho_{wd}} \right)^{\frac{1}{2}} \left(\frac{T}{10^7 \text{ K}} \right)^{\frac{3}{2}} , \tag{2.43}$$

we find that if dark matter heavier than 10^{10} GeV collapses under its own weight at the center of a white dwarf with the parameters specified, it will be massive enough to form a black hole.

The critical mass for dark matter collapse can be used to compute the final black hole's Schwarzchild radius

$$r_s = 2GM_{crit} \simeq 10^{-14} \text{ cm} \left(\frac{10^{10} \text{ GeV}}{m_X} \right)^{\frac{3}{2}} \left(\frac{10^9 \text{ g cm}^{-3}}{\rho_{wd}} \right)^{\frac{1}{2}} \left(\frac{T}{10^7 \text{ K}} \right)^{\frac{3}{2}} . \tag{2.44}$$

We remark that the Schwarzschild radius is much smaller than the radius of the white dwarf enclosing a microgram of material, $r_s \ll r_{\mu g}$ for all $m_X > 10^{10}$ GeV, which will be relevant for calculating white dwarf ignition via black hole evaporation.

The time required for the black hole to be formed is obtained from Eq. (2.37). This timescale imposes the most stringent constraint on σ_{nX}, for most of the mass range considered, when setting a bound on dark matter cross section using old white dwarfs that have not exploded yet. The minimum cross section for dark matter collapsing and forming a black hole within 3 Gyrs is displayed in Fig. 2.1. Below we will see, for dark matter masses from $m_X \sim 10^{12}$ - 10^{16} GeV, all black holes formed from dark matter with $r_s \lesssim 10^{-14}$ cm will ignite $M \lesssim 1.4 M_\odot$ white dwarfs as they evaporate.

2.1.5.2 Black hole evaporative ignition of white dwarfs

After formation, the growth and evaporation of the black hole is governed by

$$\dot{M}_{bh} = \frac{4\pi \rho_{wd} (G M_{bh})^2}{c_{wd}^3} - \frac{1}{15360\pi (G M_{bh})^2} + f_X m_X C_X. \tag{2.45}$$

The first term on the right hand side is the Bondi accretion rate, where $c_{wd} \simeq 0.03$ is the sound speed at the core of the white dwarf, which has been computed using a polytropic equation of state [122]. The second term accounts for mass loss through the emission of Hawking radiation. The third term governs the growth of the black hole from the infall of additional dark matter inside the white dwarf [123]. Dark matter masses $m_X \gtrsim 10^{10}$ GeV form black holes formed in white dwarfs with initial masses $M_{crit} = N_{sg} m_X$ such that the Bondi accretion rate is negligible compared to the Hawking term. Therefore, for the parameter space of interest, the dark matter capture rate compared to the Hawking radiation rate will determine whether the black hole evaporates or grows.

The dark matter capture rate on a small black hole at the center of the white dwarf will depend on a number of factors. If the dark matter is self-thermalized, the capture rate can be obtained by calculating the sound speed of the dark matter and determining its Bondi accretion rate on the black hole. If the dark matter cannot be modelled as an ideal gas, simulations or analytic estimates [130] of the capture rate using individual particle trajectories would be necessary. Here we will conservatively assume that the dark matter efficiently feeds the small black hole, *i.e.* that $f_X = 1$ in Eq. (2.45). This will be a conservative assumption for obtaining bounds using black hole evaporation ignition, because dark matter feeding the black hole can prevent the black hole from evaporating, which reduces its temperature and power output, thus inhibiting black hole evaporative ignition of the white dwarf.

The time for a black hole with an initial mass M_{crit} (*i.e.* the self-gravitating mass) to evaporate, when neglecting the Bondi accretion rate and setting $f_X = 1$ in Eq. (2.45), is

$$t_{bh} = \frac{M_{crit}}{m_X C_X} - \frac{a^2 \text{ArcTanh}\left[\sqrt{m_X C_X} M_{crit}/a^2\right]}{(m_X C_X)^{3/2}}, \tag{2.46}$$

where we define a Hawking evaporation constant $a^2 = (G\sqrt{15360\pi})^{-1}$. It can be shown that $\sqrt{m_X C_X} M_{crit} < a^2$ implies a rapid black hole evaporation time. In this limit, $\sqrt{m_X C_X} M_{crit} \ll a^2$, Eq. (2.46) approximates to

$$t_{bh} = 15360\pi G^2 M_{crit}^3 \simeq 10^9 \text{ yrs } \left(\frac{10^{10}\text{ GeV}}{m_X}\right)^{\frac{9}{2}} \left(\frac{10^9 \text{ g cm}^{-3}}{\rho_{wd}}\right)^{\frac{3}{2}} \left(\frac{T}{10^7\text{ K}}\right)^{\frac{9}{2}}. \tag{2.47}$$

This is the usual solution obtained when the Hawking radiation term dominates alone. On the righthand side of this expression we have used the self-gravitating dark matter mass (2.43) to determine how quickly the black hole formed in a white dwarf star evaporates. In practice, the solution (2.46) converges very quickly to (2.47) in the limit mentioned above. The condition we require therefore is that black hole evaporation exceed dark matter capture onto the black hole,

$$\frac{1}{15360\pi(GM_{crit})^2} > m_X C_X. \tag{2.48}$$

This requirement is shown in Fig. 2.2. For masses $m_X \gtrsim 10^{11}$ GeV, the capture of dark matter cannot prevent black hole evaporation for any given cross section. This is because the Hawking evaporation rate lies above the saturation value for the capture rate, *cf*. Eq. (2.1), so Eq. (2.48) is always fulfilled. Therefore, black holes formed from dark matter with mass $m_X \gtrsim 10^{11}$ GeV will inevitably evaporate.

Of course, dark matter of a mass smaller than $m_X \sim 10^{12}$ GeV can also form evaporating black holes. We see from Eq. (2.47) that black hole evaporation will occur in less than a billion years for $m_X \gtrsim 1.5 \times 10^{10}$ GeV, so long as the dark matter-nucleus cross section is small enough to satisfy Eq. (2.48). Therefore, we adopt $m_X = 1.5 \times 10^{10}$ GeV as a lower bound on the dark matter mass that can cause white dwarf evaporative black hole ignition for the white dwarf parameters given in Fig. 2.2.

We now analyze black hole evaporative heating of a microgram-sized sample of white dwarf material, and determine when the conditions for ignition are met. First, the energy transfer rate of the black hole must exceed the rate at which heat diffuses out of the sample. So long as dark matter capture on the black hole is sufficiently small, the mass evolution will be completely determined by Hawking radiation emission. The Hawking radiation rate will increase as the black hole shrinks in size

$$\dot{M}_{bh} \simeq 10^{30} \text{ GeV s}^{-1} \left(\frac{10^{33} \text{ GeV}}{M_{bh}}\right)^2 \tag{2.49}$$

Here we have normalized to a black hole mass $M_{bh} \sim 10^{33}$ GeV, which corresponds to an initial black hole mass for dark matter mass $m_X \sim 10^{13}$ GeV, *cf*. Eq. (2.43). For black hole evaporation bounds derived here, we require all formed black holes to evaporate completely. Therefore, for dark matter masses less than and greater than $m_X \sim 10^{13}$ GeV, this black hole evaporation heating rate will be matched and surpassed since we set bounds only on parameter space where the black holes evaporate completely, and the initial black hole mass shrinks with increasing dark matter mass (again see Eq. (2.43)). Comparing Eq. (2.49) to the heat diffusion rate in a white dwarf, Eq. (2.33), we see that the first requirement for black hole evaporative white dwarf ignition is satisfied, so long as a sizable portion of this energy is deposited in the white dwarf.

The second condition for evaporative black hole ignition of the white dwarf, is that the radiation emitted must effectively heat a sample of white dwarf materials to $\sim 10^{10}$ K. This will depend on the amount of energy deposited by Hawking emitted particles as they propagate across the microgram-containing region of white dwarf material. We find that this condition is satisfied for all black holes evaporating inside the white dwarf, so long as the mass of the black hole is large enough, $M_{bh} \gtrsim 10^{16}$ GeV. This condition is satisfied for all the dark matter parameters we consider.

The temperature of the black hole depends on its mass M_{bh}. As the black hole evaporates, its temperature and radiated power increase according to

$$T_{bh} = \frac{1}{8\pi G M_{bh}} \simeq 6325 \text{ GeV } \left(\frac{m_X}{10^{13} \text{ GeV}}\right)^{\frac{3}{2}} \left(\frac{\rho_{wd}}{10^9 \text{ g cm}^{-3}}\right)^{\frac{1}{2}} \left(\frac{10^7 \text{ K}}{T}\right)^{\frac{3}{2}}. \qquad (2.50)$$

After it is formed from collapsing dark matter in the white dwarf, it is evident that the black hole's temperature will increase as it evaporates. In the rightmost expression we made the replacement $M_{bh} = M_{crit}$, *i.e.* we take the black hole initial mass to be the critical mass for self-gravitation of the captured dark matter. The energy and composition of the radiated particles will depend on this temperature [131, 132]. While a detailed simulation of black hole emission propagation through white dwarf material is beyond the scope of this work, we will find that emitted color-charged particles alone are enough to ignite the white dwarf (*i.e.* emission of gluons and quarks which become mesons and hadrons during propagation). We will neglect contributions from, *e.g.*, emitted neutrinos and leptons, as these will not alter the results of our analysis. Our conclusions in this regard match the findings of Ref. [104], which presented a detailed study of Standard Model particle showers produced in the decay and annihilation of very heavy dark matter particles in white dwarfs.

At the temperatures relevant for ignition, *cf*. Eq. (2.50), all the particles present in the Standard Model are emitted relativistically. Each type of particle (where each helicity state counts as a separate particle) is emitted roughly equally up to percent level corrections [133, 134], so long as each particle's mass is less than the black hole temperature. For the temperature indicated in Eq. (2.50), we will only need to consider emitted particles that carry color charge. At these temperatures, more than half the black hole evaporation power is emitted in relativistic color-charged particles [133, 134].

Black hole radiated color-charged particles with energies $\gtrsim 10^3$ GeV, have a kinetic energy above carbon's nuclear binding energy $E_{bind} \sim 10$ MeV. To analyze the interactions of these color-charged particles (quarks, gluons which create hadrons, mesons) with carbon nuclei in the white dwarf, we follow the standard procedure for estimating hadronic showering in materials [135]. We take the inelastic carbon scattering cross-section for the high energy particles to be the geometric cross-section of the carbon nucleus, $\sigma_C \sim 10^{-25}$ cm^2. Each time a high-energy particle hits a carbon nucleus over a mean free path $l_{had} \sim (n_C \sigma_C)^{-1} \sim 10^{-7}$ cm, it fractures the carbon nucleus and creates ~ 2 - $3 \sim e$ high energy hadrons/mesons (e here is Euler's number). Each of these inelastic by-products in turn strikes a carbon nucleus, and after

N_i such interactions, the resulting showered particles each have final energies E_f of the order

$$E_f = \frac{E_i}{e^{N_i}}, \tag{2.51}$$

where E_i is the initial particle energy and $N_i \sim n_C \sigma_C l_{sh}$ is the number of inelastic scattering interactions the hadronic shower has undergone over a length l_{sh} with a carbon number density n_C. Although the initial carbon fission and subsequent showering processes are endothermic, the total heat deposition is vast enough to satisfy the ignition conditions as the black hole reaches its final stages of evaporation. The total mean free path of the emitted hadronic shower will be

$$\begin{aligned} l_{sh} &= \frac{1}{n_C \sigma_C} \ln\left(\frac{E_i}{E_f}\right) \\ &\approx 3 \times 10^{-6}\ \text{cm}\ \left(\frac{5 \times 10^{31}\ \text{cm}^{-3}}{n_C}\right)\left(\frac{10^{-25}\ \text{cm}^2}{\sigma_C}\right) \text{Ln}\left[\left(\frac{E_i}{10^3\ \text{GeV}}\right)\left(\frac{10^{-3}\ \text{GeV}}{E_f}\right)\right], \end{aligned} \tag{2.52}$$

where we have normalized the carbon density to a typical white dwarf core density of 10^9 g cm^{-3}. At each showering stage, the emitted hadrons scatter inelastically against nuclei, the resulting hadrons produced in the collision split the initial energy. At the relevant ignition energies ($\sim$ MeV), the majority of the final showered by-product particles are pions. Note that the length of the shower depends only logarithmically on the energy E_{in} of the initial color-charged particle.

We see that the mean free path for a high-energy color-charged particle is much less than the radius of white dwarf enclosing a microgram of material $l_{had} \lesssim r_{\mu g} \simeq 7 \times 10^{-6}$ cm, whereas the showering length is $l_{sh} \lesssim r_{\mu g} \simeq 7 \times 10^{-6}$ cm. Note that these statements hold even for the smallest black holes formed by dark matter in this study: for $m_X \sim 10^{17}$ GeV, $M_{bh} \sim 10^{27}$ GeV, and $l_{sh} \sim 6 \times 10^{-6}$ cm. This implies that the color-charged particles emitted from the black hole travel a short distance, compared to the sample size, before scattering inelastically against nuclei. The showers produced have a somewhat larger energy deposition length, heating a $\sim \mu$g white dwarf region to MeV temperatures roughly uniformly during subsequent showering. Therefore, we find that color-charged particles emitted from the black hole constitute an efficient, isothermal heating mechanism that will prompt white dwarf ignition. We remark that, although the highest energy color-charged Hawking particles induce fission in nuclei upon collision, the final output particles in the hadronic shower (which exponentially outnumber the higher energy input particles) lack the energy to produce further fission. Therefore, we can safely assume that the critical temperature T_c for ignition remains unchanged, as the majority of the $\sim \mu$g mass white dwarf sample preserves its composition as it heats up.

Finally, while they are not necessary for ignition, we briefly comment on the emission of non-color-charged particles, and photons. The emitted photons scatter inelastically against nuclei, producing hadronic showers. At these energies, this is the dominant mechanism involved. The inelastic scatters generate these photonuclear showers after a somewhat longer mean free path, since they couple to nuclei through the electromagnetic rather than the strong force. Similarly, emitted electrons scatter inelastically via the exchange of a virtual photon. The difference compared to the previous cases discussed, is that the electron survives the interaction. Both electronuclear and photonuclear showers will contribute less to white dwarf heating than the black hole's hadronic emission, since for the black hole temperatures we consider, there is more emission of strongly-coupled particles.

We have now established that black holes with masses $M_{bh} \sim 10^{27}$ - 10^{33} GeV, formed from collapsing dark matter in white dwarfs, will quickly and uniformly heat a microgram of white dwarf material to ignition via Hawking evaporation. It remains to point out that the large masses of these black holes imply that the energy they impart to the microgram mass vastly exceeds the $\sim 10^{13}$ GeV required for ignition, *cf*. Eq. (2.38) and surrounding discussion. Thus, we find that the white dwarf is ignited by dark matter collapsing and forming a black hole in its interior, for dark matter masses $m_X \gtrsim 1.5 \times 10^{10}$GeV, so long as the black hole evaporates, which in turn depends on how much the black hole is fed by accreted dark matter. For this parameter space, the most restrictive constraint on the cross section comes from the requirement that the dark matter collapses and forms a black hole in less than a few gigayears.

2.1.5.3 Black hole destroying the white dwarf

In addition to the previous analysis, there is a region of the parameter space where the black hole, fed by dark matter and white dwarf material, grows over time to consume the white dwarf star. Comparing the Bondi accretion rate to the Hawking evaporation rate, we see that a newly-formed black hole needs a minimum mass

$$M_{bondi} = \left(\frac{c_{wd}^3}{61440\pi^2 \rho_{wd} G^4} \right)^{1/4} \simeq 5 \times 10^{37} \text{ GeV} \left(\frac{10^9 \text{ g cm}^{-3}}{\rho_{wd}} \right)^{\frac{1}{4}}, \tag{2.53}$$

for the accretion of stellar material to exceed the evaporation rate. The initial mass of the black hole will be larger than this mass for dark matter masses $m_X \lesssim 10^{10}$ GeV, *cf*. Eq. (2.43). In that case, for cross sections below those necessary for ignition via nuclear scattering, any black hole formed will accrete both dark matter and stellar material, quickly consuming the star in a short timescale. For heavier dark matter masses 10^{10} GeV $\lesssim m_X \lesssim 10^{12}$ GeV, the initial black hole mass is small enough that the Hawking evaporation rate dominates over accretion of stellar material. However, if the dark matter-nuclear cross section is large enough such that the black hole is fed efficiently, *cf.* Eq. (2.48), captured dark matter feeds the black hole preventing it from evaporating. We find for all green-shaded parameter space in Fig. 2.2 that the black hole reaches a mass (2.53) in less than a few billion years before consuming the white dwarf.

To summarize: if the dark matter-nucleon cross section is below that necessary for ignition via nuclear scattering, but at the same time large enough to prevent black hole evaporation, dark matter of mass $m_X \lesssim 10^{12}$ GeV will collapse forming a black hole that quickly destroys the star. In particular, the capture rate not only determines the time it takes to form a self-gravitating dark matter sphere, but also the rate at which the black hole is fed, preventing evaporation. Using an old white dwarf that has not exploded, we set bounds on the dark matter-nucleon cross section by requiring a self-gravitating dark matter sphere to be formed and collapse in no less than 3 Gyrs, as well as requiring that the black hole so formed destroys the white dwarf either through dark matter accretion, Bondi accretion of baryons, or both. This yields the additional green exclusion zone plotted in Fig 2.2.

2.2 Constraints Inferred from Massive White Dwarf Lifetime

The final constraints on σ_{nX}, inferred from the existence of an isolated white dwarf that has not exploded yet, are plotted in Fig. 2.2 for all the dark matter mass range considered here. A sizable region below the Xenon-1T results [23] is excluded, which has some overlap with bounds derived from neutron star implosions [136]. The constraints in Fig. 2.2 were drawn utilizing a generic per-nucleon cross section to characterize how dark matter is captured, thermalized, and eventually explodes the white dwarf from within. However, they can be applied to specific models of dark matter capable of igniting white dwarfs.

We now turn to investigate two specific models of asymmetric heavy dark matter where the interaction to the Standard Model is mediated by light particles and $\mathcal{O}(1)$ gauge coupling constants. Specifically, we consider below vector- and scalar-mediated interactions through a dark photon and Higgs portal, respectively. Both models imply dark-matter self-interactions, mediated by the Yukawa couplings of the vector and scalar mediators, *i.e.* the same mediators (V_μ or ϕ) that couples dark matter to the visible sector. For a scalar ϕ, this self-interaction is purely attractive. Alternatively, for a vector ϕ, XX and $\bar{X}\bar{X}$ interactions are repulsive, while $X\bar{X}$ interactions are attractive. A detailed analysis of the self-interaction cross section for this potential, both in the perturbative and non-perturbative regime, is given in [138]. In Sec. 2.1.4 we studied how strongly self-interacting dark matter might affect whether the dark matter sphere at the center of a white dwarf collapses. We found that, even assuming the dark matter is self-thermalized and has the sound speed of an ideal gas (which would correspond to dark matter with substantial self-interactions), a self-gravitating dark matter sphere will satisfy the Jeans instability criterion and collapse at the center of a white dwarf. Therefore, sizable dark matter self-interactions should not substantially alter white dwarf explosion bounds.

We also briefly comment on the cosmology of these models. With late-decaying

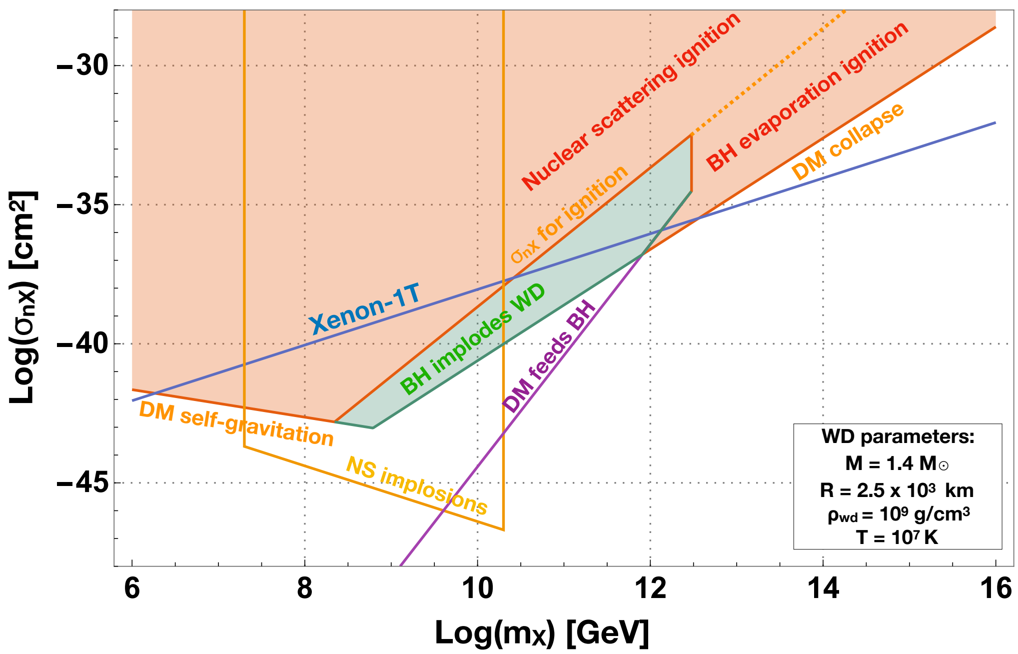

Figure 2.2: Constraints on the dark matter-nucleon cross section σ_{nX}, as a function of m_X, for Type Ia supernova ignition within 3 Gyrs, by either nuclear scattering or black hole evaporation (orange). Lines labelled "DM self-gravitation" (orange/green) and "σ_{nX} for ignition" (orange), denote the minimum σ_{nX} for white dwarf ignition by nuclear scattering, either from requiring that enough dark matter is captured so that it "self-gravitates", or that collapsing dark matter scatters frequently enough to ignite the white dwarf. The line labelled "DM collapse" (orange/green) limits the parameter space where dark matter will not ignite the white dwarf during collapse, but instead collapses and forms a black hole. Complete evaporation of this black hole via Hawking radiation ignites the white dwarf. The line "DM feeds BH" (purple) denotes the limiting region where black hole evaporation is potentially stalled by further dark matter capture (see Fig. 2.1). The region "BH implodes WD" (green) is the parameter space where a black hole that consumes the white dwarf would be formed. A dark matter halo density $\rho_X \simeq 0.3$ GeV cm^{-3} at the location of the white dwarf is assumed. All bounds were obtained using the parameters displayed in the lower right, taken from an old white dwarf (SDSS J160420.40+055542.3) selected to provide the most stringent bound for $m_X \lesssim 10^8$ GeV, out of all single white dwarfs listed in the Montreal White Dwarf Database [111]. See [102] for an extended discussion of bounds obtained from different white dwarfs, including those in old globular clusters [137]. Also displayed are the bounds obtained from the Xenon-1T experiment (blue) [23] and neutron star implosions (yellow) [136].

fields that deplete the late-time abundance of asymmetric dark matter, super-heavy asymmetric dark matter cosmologies have been constructed in Ref. [113] (see also Chap. 4). Using various methods that deplete late-time relic particle abundances, it would be possible to construct a cosmology for the dark matter models considered here, though precise model parameters satisfying these cosmologies will depend on a number of factors, for example the late-time energy density of decaying fields. A detailed treatment has been left for future investigation. Both of the above dark sector mediators, and their respective mixing mechanisms allow V_μ and ϕ to decay in the early Universe, and constraints on the mixing parameters can be obtained from requiring Big-Bang nucleosynthesis to be unaffected by these decays and the resulting dilution of baryon density [139]. These constraints have been accounted for in the results below.

2.2.1 Dark Photon Portal

The first explicit dark matter model is a Dirac fermion X as dark matter, which is charged under a new $U(1)_D$ gauge group with gauge coupling constant α_X. The vector mediator V_μ of this gauge group mixes with the Standard Model photon, see *e.g.* [140, 141, 139]. For this mixed-vector mediator model, often called "hidden photon" or "vector portal" dark matter, the coupling to the Standard Model is mediated through the following mixing terms in the Lagrangian

$$\mathcal{L}_{mix} = \frac{\epsilon_\gamma}{2} V_{\mu\nu} F^{\mu\nu} + \kappa^2 V_\mu Z^\mu. \tag{2.54}$$

Here $V_{\mu\nu} = \partial_\mu V_\nu - \partial_\nu V_\mu$ is the $U(1)_D$ field-strength tensor, the first term is the dark-visible photon kinetic mixing term with mixing coupling ϵ_γ, while the second term gives the mass mixing between the $U(1)_D$ vector boson and the Standard Model Z boson with dimensionful coupling parameter κ. The dark matter-nucleon scattering cross section against protons in this case is [139]

$$\sigma^p_{nX} \simeq 2 \times 10^{-39}\ \mathrm{cm}^2 \quad \left(\frac{\alpha_X}{10^{-1}}\right) \left(\frac{\mathrm{GeV}}{m_\gamma}\right)^4 \left(\frac{\epsilon_\gamma}{10^{-5}}\right)^2 \tag{2.55}$$

This dark photon model presents a much faster thermalization time as it allows dark matter to lose energy through repeated scatterings against electrons in the white dwarf. The energy loss rate for scattering against unbound electrons is [142],

$$\left(\frac{dE}{dt}\right)_{e^-} \simeq \left(\frac{8\pi\alpha_X\alpha_{em}\epsilon_\gamma^2 m_e^2 \Delta E n_e v_{rel}}{(m_\gamma + q^2)^2}\right) \mathrm{Min}\left[\frac{q}{p_F}, 1\right]. \tag{2.56}$$

We note that although Eq. (2.56) is valid for unbound electrons, this can be reasonably applied to white dwarfs since electrons in the interior can be treated as a nearly free gas [122]. We have also added a Pauli blocking factor $\mathrm{Min}[q/p_F, 1]$ accounting for the fact that electrons are degenerate within the white dwarf medium, with a Fermi momentum $p_F \sim (3\pi^2 n_e)^{1/3} = (18\pi^2 n_a)^{1/3} \sim 5$ MeV. This energy loss mechanism is far more efficient than nuclear scattering when the latter is suppressed by the structure factor, leading to much shorter thermalization and collapse times. For instance, the final phase of thermalization (where nuclear scattering is suppressed, *cf*. Eq. (2.21)) would be completed through electron scattering in a time

$$t^{th}_{e^-} \simeq \frac{p_F E_{sup}}{2\pi\alpha_X\alpha_{em}\epsilon_\gamma^2 n_e} \simeq 10^{-5}\ \mathrm{s} \left(\frac{m_X}{10^6\ \mathrm{GeV}}\right) \left(\frac{\rho_{wd}}{10^9\ \mathrm{g\ cm^{-3}}}\right)^{\frac{1}{3}} \left(\frac{10^7\ \mathrm{K}}{T}\right) \tag{2.57}$$

In the rightmost expression, we conservatively chose $\alpha_X \simeq 0.1$, a dark photon mass $m_\gamma \simeq 10^{-12}$ eV and mixing parameter $\epsilon_\gamma \simeq 10^{-7}$. Note that this implies a much

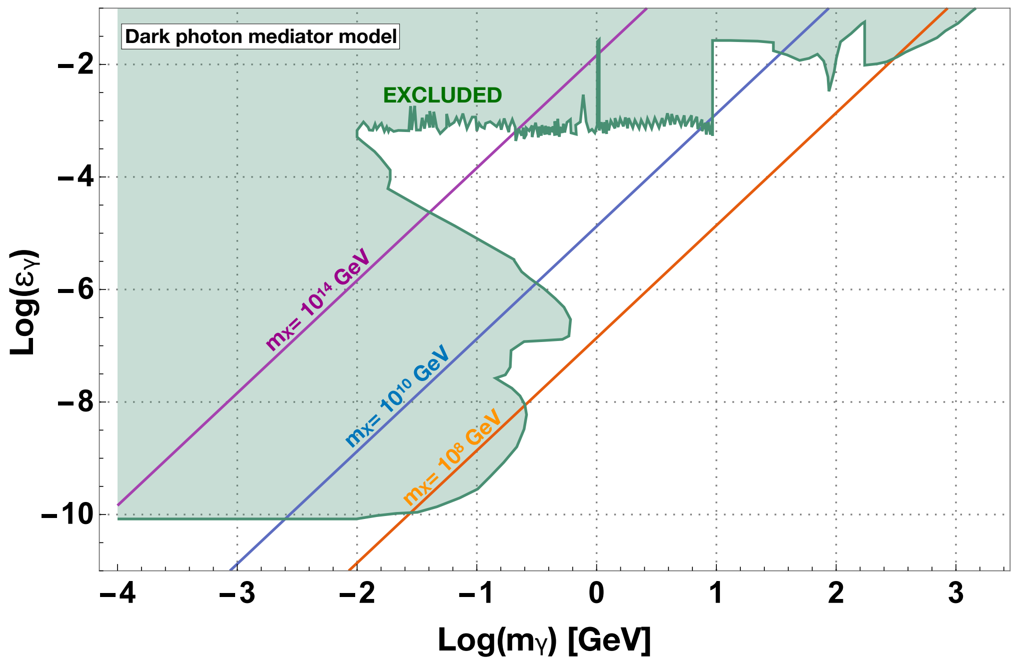

Figure 2.3: Constraints on the mixing parameter ϵ_γ for vector-mediated interactions as a function of its mass m_γ, in a log-log plot. We fix $\alpha_X = 10^{-1}$ (note the linear dependence of the cross section on this parameter). The different colors correspond to different dark matter masses, as labeled. Regions above the solid lines are excluded by observations of the old white dwarf SDSS J160420.40+055542.3. Shaded regions denote parameter space bounded by supernova cooling and particle colliders [143, 144, 145, 146, 147, 148, 149]. We have omitted constraints on dark photons that would decay during, and thereby alter primordial nuclear abundances from big bang nucleosynthesis [150].

smaller dark photon mass than is shown in Fig. 2.3. Consequently, we see that a vector portal model coupled through a very light dark photon can be constrained using old white dwarfs that have not exploded, given the efficient transfer of dark matter kinetic energy via electron scattering, for a sufficiently low mass dark photon. The resulting constraints obtained by relating the above timescale to the cooling age of SDSS J160420.40+055542.3 [111] are shown in Fig. 2.3, for various dark fermion masses.

2.2.2 Higgs Portal

Next, we consider a dark matter model, which couples to the Standard Model via a Yukawa interaction with a scalar mediator ϕ that in turn mixes with the Higgs boson [151]. Again, we take the dark matter to be a Dirac fermion X. For this "Higgs portal" dark matter model, the real scalar field ϕ mixes with the Higgs boson H through terms of the form

$$\mathcal{L}_\phi = -\alpha_\phi \phi X \bar{X} - (a\phi + b\phi^2)\,|H|^2\,, \tag{2.58}$$

where H is the Standard Model Higgs doublet and a, b are coupling constants, with a having dimensions of mass and b being dimensionless. In the limit $a, m_\phi \ll v, m_h$, where $v \approx 246$ GeV is the Higgs vacuum expectation value after electroweak symmetry breaking, the mixing angle is $\epsilon_h \simeq av/m_h^2$, with the following term describing the resulting coupling of ϕ to Standard Model fermions

$$\mathcal{L}_{int} = -\frac{m_f}{v} f\bar{f}\phi \tag{2.59}$$

For the case of a scalar mixed with the Higgs boson, the nucleon scattering cross-section is

$$\sigma_{nX} \simeq 2 \times 10^{-38}\ \mathrm{cm}^2 \quad \left(\frac{\alpha_\phi}{10^{-1}}\right) \left(\frac{30\ \mathrm{MeV}}{m_\phi}\right)^4 \left(\frac{\epsilon_h}{10^{-5}}\right)^2 \tag{2.60}$$

Using the white dwarf explosion bounds obtained for the dark matter-nucleon cross section yields the bounds on this Higgs portal dark matter model, shown in Fig. 2.4. Additional constraints on the mixing parameters from meson decay experiments are

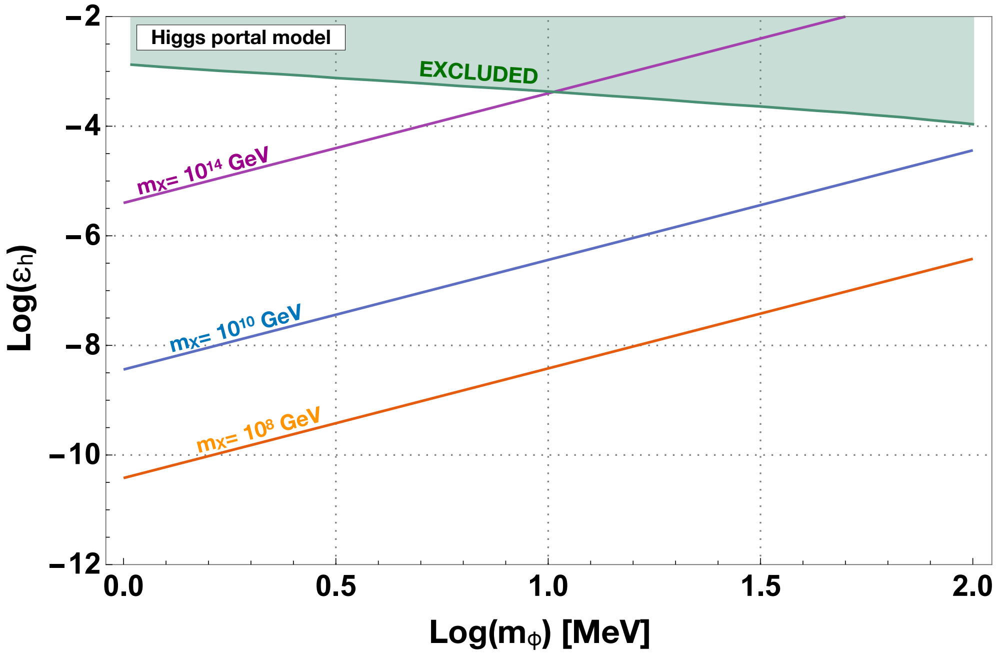

Figure 2.4: Constraints on the mixing parameter ϵ_h for scalar ϕ as a function of its mass m_ϕ, in a log-log plot. We fix $\alpha_\phi = 10^{-1}$ (note the linear dependence of the cross section on this parameter). The different colors correspond to different dark matter masses; regions above these coloured lines are excluded by observation of the old white dwarf SDSS J160420.40+055542.3. Shaded parameter space is excluded by non-observation of anomalous meson decays at the CHARM experiment [152]. There are additional constraints on the Higgs portal scalar from cosmological considerations, including contributions to relativistic degrees of freedom, distortions of the cosmic microwave background, and primordial nucleosynthesis abundances [153].

also shown in the same plot for comparison. We fix $\alpha_\phi = 0.1$ and the dark matter mass, then solve for the value of ϵ_h corresponding to the per-nucleon cross-section that would cause the 3 Gyr old white dwarf SDSS J160420.40+055542.3 [111], to explode.

Chapter 3

Old Neutron Stars as Dark Matter Probes

Unlike white dwarfs, neutron stars are forged in the core of more massive stars that end their lives as core-collapse supernovae. The precise conditions for which a progenitor star leaves behind a neutron star rather than a black hole are, however, subject to uncertainty. Neutron stars have typical masses in the range 1 - 2.4 $M_\odot$ and are extremely compact, with radii of order 10 - 15 km. Their central densities can exceed $\sim 10^{15}$ g cm^{-3}, comparable to the density of an atomic nucleus, making these objects the densest in the universe, and a highly attractive target to discover new physics.

Various works in the past have demonstrated that neutron stars are a promising probe for dark matter [154, 155, 156, 157, 158, 159, 160, 161, 162, 123, 163, 164, 165, 112, 137, 166, 101, 106, 167, 104, 168, 169, 170, 171]. For instance, cold neutron stars have the potential to serve as excellent next-generation thermal detectors of dark matter, heated by the scattering and annihilation of dark matter accelerated to relativistic speeds in their deep gravitational wells. While a $\sim$ Gyr neutron star can have temperatures as low as $\sim$ 100 K, dark kinetic heating alone may raise this temperature to $\sim$ 1700 K, even for very small dark matter-nucleon cross sections. In fact, it was recently shown that measuring the effective temperature of a nearby old neutron star with next-generation infrared telescopes, such as the newly-launched James Webb, would place leading bounds on dark matter interactions with nucleons in a wide dark matter mass range [172], based on this effect. The identification of old neutron stars as close as ~ 50 pc could be done by detecting their faint radio emission with radio facilities like FAST [173], and this in turn would allow measuring their temperature in a feasible exposure time with infrared telescopes.

A question remains, however, pertaining the nature of the neutron star itself: What is the exact composition of the core? The existing uncertainty about this extremely dense region makes it difficult at present to unequivocally compute dark matter scattering and its associated heating. By contrast, the physics of the thin outer layer of the neutron star, the crust, is by far more robustly understood. In this Chapter[1], we show how dark matter scattering solely with the low-density crust still kinetically heats neutron stars to infrared temperatures detectable by forthcoming telescopes, as proposed in Ref. [174]. For both spin-independent and spin-dependent scattering on nucleons, the crust-only cross section sensitivity reaches 10^{-43} - 10^{-41} cm^2 for dark matter masses of 100 MeV - 1 PeV, with the best sensitivity arising from dark matter scattering with a crust constituent called nuclear pasta (including gnocchi, spaghetti, and lasagna phases). For dark matter masses from 10 eV - 1 MeV, the sensitivity is 10^{-39} - 10^{-34} cm^2, arising from exciting collective phonon modes in a neutron superfluid in the inner crust. Furthermore, for any s-wave or p-wave annihilating dark matter, we demonstrate that dark matter can efficiently annihilate by thermalizing just with the neutron star crust, regardless of whether the dark matter ever scatters with the neutron star core. This implies efficient annihilation in neutron

[1]For clarity, we follow in this Chapter the notation used in [174]: we will use DM instead of an X sub-index to denote the dark matter properties, *e.g.* $m_X \to m_{\rm DM}$.

stars for any electroweakly interacting dark matter with inelastic mass splittings of up to 200 MeV, including Higgsinos.

3.1 Neutron Star Crust Structure

The crust of a neutron star, about 1 km thick, spans over 10 orders of magnitude in density and consists of several distinct layers corresponding to different phases of nuclear matter. Although it is reasonably understood, the breadth of physics required to fully describe its structure places the crust among the most complex astrophysical objects.

The neutron star atmosphere and ocean, with density $< 10^4$ g/cm^3 and depth $\mathcal{O}(\mu\text{m})$, and made of a thin plasma layer, affect the star's thermal spectrum, and are influenced by the star's magnetic field. The outer crust (density 10^4 - 10^{11} g/cm^3) is a crystalline lattice of neutron-rich nuclei, along with degenerate free electrons [175, 176, 177]. The inner crust begins below the "neutron drip line" marked by density $\rho_{\rm ND} \simeq 4.2 \times 10^{11}$ g/cm^3 [177]. Here, it is energetically favourable for neutrons to be liberated from nuclei, and so the inner crust begins as a mixture of a dripped neutron fluid and nuclei in the form of "clusters" arranged in a lattice [178, 179, 180]. Further down, the inner crust density approaches the nuclear saturation point $\rho_0 \simeq 2 \times 10^{14}$ g/cm^3, and intricate competition between nuclear attraction and Coulomb repulsion forms extended non-spherical "pasta" phases of nuclear matter; as the density increases, gnocchi, then spaghetti, and then lasagna pasta phases become more prevalent [181, 182, 183, 184].

In the deepest layer of the inner crust there are "inverted pasta phases" where nuclear density material predominates over sparser, sub-nuclear density voids. This

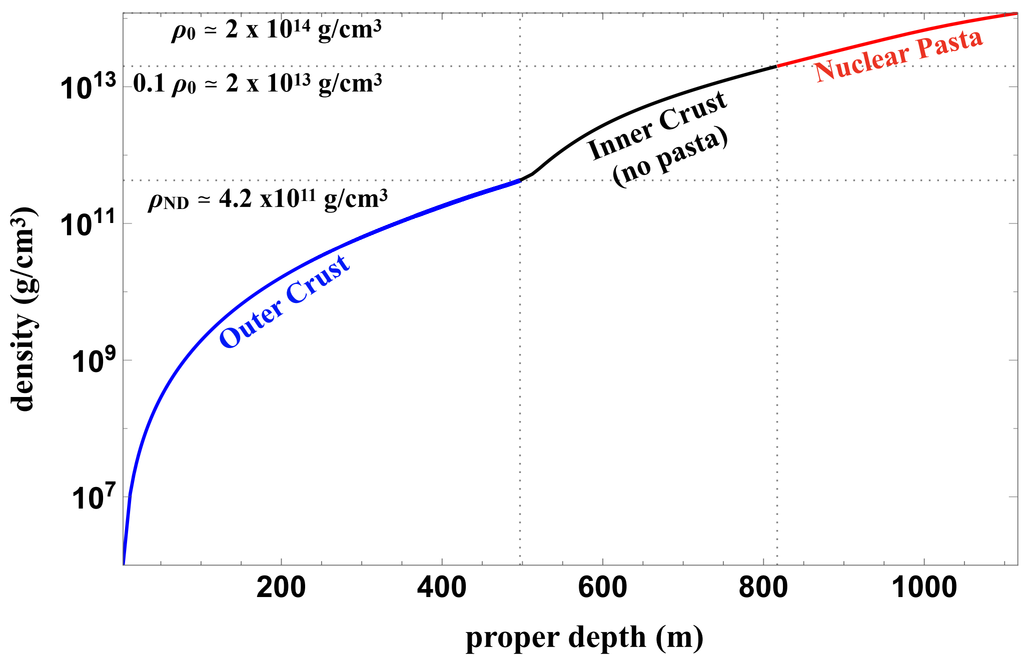

Figure 3.1: The density of neutron star crust as a function of proper depth, obtained using a benchmark high-density equation of state BsK21, for a benchmark scenario of a 1.8 $M_\odot$ mass, 12.5 km radius neutron star. The densities at the transitions between various layers as described in the text are marked.

includes bucatini (anti-spaghetti) and swiss cheese (anti-gnocchi) phases. The crust terminates at densities around ρ_0. Beyond this lies the outer core (densities 0.5 - 2 ρ_0) and inner core (densities 2 - 10 ρ_0). Fig. 3.1 shows the density of the crust as a function of the proper depth using a representative equation of state, BsK21 [177, 185, 186], for representative benchmark neutron star parameters, with mass 1.8 $M_\odot$ and radius 12.5 km. We also consider other similar equations of state below to test how our sensitivity predictions change with the crust thickness and layering. Additionally, Fig. 3.2 shows the number of bound and free nucleons as a function of the crust density, computed for the same equation of state previously mentioned. The information contained in both figures will be repeatedly used below to compute optical depths for the dark matter scattering in the crust. For further details of the interior of a neutron star crust, we refer the reader to Ref. [174] and references therein.

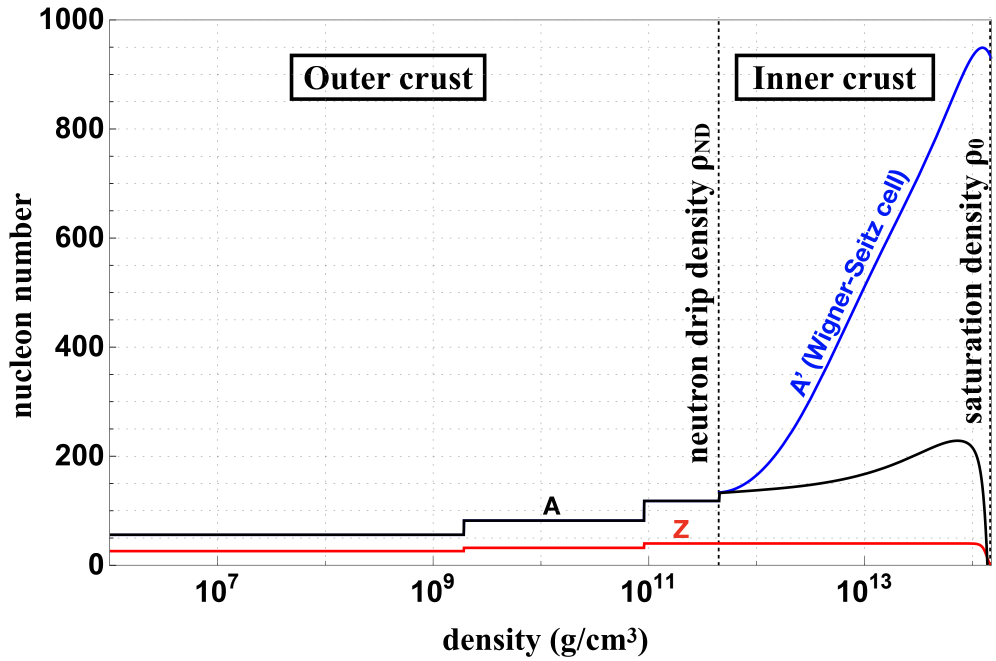

Figure 3.2: Bound and free nucleon number as a function of neutron star crust density. The different transition densities are indicated with vertical lines. See text for details.

Before proceeding, we briefly comment as well on the core of a neutron star. This high-density phase of matter is currently plagued with uncertainties [187]. It has been hypothesized that the core could consist of meson and hyperon condensates [188, 189, 190, 187], or deconfined *ud* quark matter [191] or *uds* quark matter [192, 193, 194, 195, 196, 197]; the latter could exist in a color flavor locked phase [198, 199] and may co-exist with confined states [200, 201, 202]. While the existence of any additional degrees of freedom in the neutron star generally lead to softer equations of state, and therefore predict a reduced neutron star mass, the heaviest found neutron stars to date, i.e., PSR J0740+6620 at $2.14^{+0.10}_{-0.09}\, M_\odot$ [203], still permit exotic cores [204, 197, 205, 206]. Dark matter scattering on these phases may for instance be kinematically forbidden [165]. Therefore, the crust becomes especially relevant when establishing robust sensitivity projections for dark matter based on neutron star heating.

3.2 Neutron Star Crusts as Robust Targets for Dark Matter

Based on the above considerations, we show here how dark matter scattering proceeds on each of the crust layers. In particular, we demonstrate below that the inner crust and the pasta phases play a key, non-trivial role in dark matter capture, and have important implications for telescope searches for dark matter heating of neutron stars.

3.2.1 Dark Kinetic Heating

We first provide a brief overview of the dynamics of dark matter capture and kinetic heating in neutron stars. The steep gravitational potential of a neutron star accelerates non-relativistic dark matter particles falling into it to relativistic speeds. The kinetic energy of the dark matter of mass $m_{\rm DM}$ at the neutron star surface, in the stellar rest frame, is given by

$$E_{\rm DM} = m_{\rm DM}(\gamma - 1) \ , \tag{3.1}$$

where $\gamma = (1-v_{\rm esc}^2)^{-1/2}$, with the escape velocity at the star surface $v_{\rm esc} = \sqrt{2GM_\star/R_\star}$, and $M_\star$ and $R_\star$ are the mass and radius of the star. As mentioned before, for our study, we adopt the benchmark values

$$M_\star = 1.8\ M_\odot, \quad R_\star = 12.5\ \text{km}, \tag{3.2}$$

so that we have $v_{\rm esc} = 0.65$ and $\gamma = 1.32$. These parameters are chosen to represent realistic and conservative neutron star values; we will see shortly that for neutron star crust capture, less massive stars tend to capture more dark matter. A dark matter particle is captured, *i.e.* becomes gravitationally bound to the star, if it loses its halo kinetic energy through one or more scatters with stellar constituents. The total dark matter mass capture rate is given by [154, 172]

$$\dot{M}_{\rm DM} = \rho_{\rm DM} v_{\rm halo} \times \pi b_{\rm max}^2 \times f, \tag{3.3}$$

where $\rho_{\rm DM} = 0.42$ GeV/cm^3 and $v_{\rm halo} \simeq 230$ km/s [207] are the best-fit halo dark matter density and average speed respectively, and $b_{\rm max} = \gamma R_\star \times v_{\rm esc}/v_{\rm halo}$ is the maximum impact parameter for dark matter to intersect the neutron star [172]. The factor f is the fraction of dark matter particles captured after passing through the neutron star, given by

$$f = \mathrm{Min}\left[1, \frac{\sigma_{\rm T\chi}}{\sigma_{\rm T\chi}^{\rm cap}}\right] \,, \tag{3.4}$$

where $\sigma_{\rm T\chi}$ is the cross section for dark matter scattering on a target (*e.g.*, nucleon, lepton) in the star, and $\sigma_{\rm T\chi}^{\rm cap}$ is the minimum cross section required for dark matter to capture. The rate of dark matter kinetic energy transfer to the neutron star is

$$\dot{\mathcal{E}}_k = \dot{M}_{\rm DM}(\gamma - 1) \times \kappa \,, \tag{3.5}$$

where κ is the fraction of the dark matter kinetic energy that is deposited into stellar constituents. This kinetic energy deposited by dark matter could be the predominant heat source for an old neutron star [172]. Over the timescales of interest, the neutron star will rapidly attain thermal equilibrium, and so $\dot{\mathcal{E}}_k$ is also the rate at which the neutron star radiates heat. Assuming black body radiation, this luminosity equals $4\pi R_\star^2 \sigma_{\rm SB} T_{\rm eff}^4$, where $\sigma_{\rm SB}$ is the Stefan-Boltzmann constant and $T_{\rm eff}$ is the "effective" (surface) temperature of the neutron star. For a distant observer, $T_\infty = T_{\rm eff}/\gamma$. Thus for the benchmark star parameters given in Eq. (3.2) and $\kappa = 1$ in Eq. (3.5), we have the dark matter kinetic heating temperature

$$T_\infty = 1730 \text{ K}. \tag{3.6}$$

Without this heating mechanism, an isolated 10^9 year-old neutron star would cool down to $\mathcal{O}(100)$ K [208, 209]. Other than dark matter heating, neutron stars may also be reheated by other astro-nuclear model-dependent internal heating mechanisms [210] and the accretion of interstellar medium, which may be deflected by the star's magnetic fields and preferentially heat its poles [172]. In the case of extremely fast-rotating (sub-7 ms period) neutron stars and for certain equations of state, rotochemical heating should also be considered [211]. However, for most neutron stars after 10^9 years, all these heating processes with the exception of dark matter kinetic heating are expected to be negligible.

3.2.2 Framework for Neutron Star Crusts

First, we will take the trajectory of dark matter through the crust to be a straight line that passes through the center of the star. This is a conservative choice, since any other trajectory implies a longer path for dark matter through the crust and hence more scattering targets along its path. The optical depth of a dark matter particle in the crust is

$$\tau_{\rm DM} = \int_{\rm crust} n_{\rm T} \sigma_{{\rm T}\chi} dz \ , \tag{3.7}$$

where n_{T} is the number density of scattering targets, $\sigma_{\mathrm{T}\chi}$ is the cross section for dark matter scattering on a target, and the integration variable $z = (R_\star - r)\gamma$ is the proper distance traveled by dark matter in the crust, where r is the Schwarzschild radial co-ordinate. Note that z integrates over every crustal layer twice, to account for dark matter both entering and exiting the neutron star. The integral in Eq. (3.7) can be conveniently recast in terms of the crust density by using the light-and-thin crust approximation [212, 213], valid for neutron stars of typical mass and radius such as the one we have considered. Since the mass and thickness of the crust is $\lesssim 10\%$ of the star's total mass and radius, the equation for the hydrostatic equilibrium of the neutron star can be written in a simplified form [212, 213],

$$\frac{dP}{dz} = g_s \rho, \tag{3.8}$$

where P is the pressure and $g_s = GM_\star\gamma/R_\star^2$ is the acceleration due to gravity at the star surface. If the equation of state, *i.e.* P as a function of the density ρ, is known, it is helpful to use Eq. (3.8) to rewrite Eq. (3.7) as

$$\tau_{\mathrm{DM}} = \frac{1}{g_s}\int_{\mathrm{crust}} n_{\mathrm{T}}\sigma_{\mathrm{T}\chi}\frac{1}{\rho}\frac{dP}{d\rho}d\rho \ , \tag{3.9}$$

where $dP/d\rho$ may in practice be computed from analytical representations of the equation of state, see [174] for further details on this procedure.

We will assume that scattering is isotropic in the dark matter-target center-of-momentum frame, which results in a flat spectrum of energy transfers:

$$\frac{d\sigma}{d\Delta E} = \frac{\sigma_{\mathrm{T}\chi}}{\Delta E_{\mathrm{max}}} \ , \tag{3.10}$$

where $\Delta E_{\rm max}$ is the maximum energy transferred. For this spectrum the average energy transferred $= \Delta E_{\rm max}/2$; for dark matter recoiling against a single nucleon this is [172]

$$\Delta E_{\rm ave} = \frac{m_{\rm n} m_{\rm DM}^2 \gamma^2 v_{\rm esc}^2}{(m_{\rm n}^2 + m_{\rm DM}^2 + 2\gamma m_{\rm n} m_{\rm DM})}. \tag{3.11}$$

This transferred energy exceeds the dark matter halo kinetic energy $m_{\rm DM} v_{\rm halo}^2/2$ for $m_{\rm DM} \lesssim 10^6$ GeV. Consequently, a single scatter in the crust suffices to capture dark matter in this mass range, which will be the focus here. For higher dark matter masses multiple scatters will be required for capture; a careful treatment of dark matter capture via multiple scattering in the crust is left for future study.

Once a dark matter particle is gravitationally captured, it oscillates around the star in an orbit that rapidly shrinks as it transits the crust multiple times, until it is completely contained within the star. This stage of thermalization occurs on a short timescale. To see this, first note that the average energy lost by dark matter for each transit through the crust is

$$\Delta E_{\rm cross} \simeq \tau_{\rm DM} \times \Delta E_{\rm ave} \ , \tag{3.12}$$

where $\tau_{\rm DM}$ is the optical depth given by Eq. (3.7) and ΔE is the energy lost per scatter, given by Eq. (3.11). Next, consider the radial trajectory of a dark matter particle oscillating across the neutron star. This trajectory is equal to an ellipse with eccentricity 1 and semi-major axis $r/2$, where r is the "apastron", the maximum distance of the particle from the centre of the star, given in terms of the particle energy by

$$r(E) = \frac{2GM}{1-(E/m_{\rm DM})^2} \ . \tag{3.13}$$

The orbital period $t_{\rm orb}$ for this particle is then the same as that of a circular orbit of radius $r/2$, hence from Kepler's Third Law we have

$$t_{\rm orb} = \eta^{-1} \frac{\pi r^{3/2}}{\sqrt{2GM_\star}} \ , \tag{3.14}$$

where $\eta = \sqrt{2}$ accounts for the particle trajectory through a homogeneous sphere [214]. From Eqs. (3.12) and (3.14) the rate of energy loss is

$$\frac{dE}{dt} \simeq \frac{2\sqrt{GM_\star}}{\pi r(E)^{3/2}} \ \Delta E_{\rm cross} \ . \tag{3.15}$$

The total (proper) time for thermalization can now be obtained by using Eq. (3.13) to integrate Eq. (3.15) from an initial energy $m_{\rm DM} + m_{\rm DM} v_{\rm halo}^2/2$ to a final energy $m_{\rm DM}\gamma^{-1}$, which is the gravitational binding energy at the star surface. Performing this integration for $M_\star = 1.8 M_\odot$ and $R_\star = 12.5$ km, we have for $m_{\rm DM} \gg m_{\rm n}$ the thermalization timescale,

$$\tau_{\rm therm} \simeq 5 \times 10^4 \ {\rm s} \left(\frac{10^{-42} \ {\rm cm}^2}{\sigma_{{\rm n}\chi}} \right) \left(\frac{m_{\rm DM}}{10^6 \ {\rm GeV}} \right) \ , \tag{3.16}$$

which is normalized to the largest $m_{\rm DM}$ we consider and the net capture cross section of the crust for $m_{\rm DM} \gtrsim 1$ GeV. This is a very short timescale, and could be shorter for $m_{\rm DM} = \mathcal{O}(100 \ {\rm MeV})$ due to the coherent response of the pasta phases. As for $m_{\rm DM} \ll m_{\rm n}$, it can be seen from Eq. (3.11) that a single scatter deposits most of the dark matter kinetic energy into the crust.

The total energy deposited by a dark matter particle through the thermalization process $\simeq m_{\rm DM}(1 - \gamma^{-1})$. An additional, small amount of energy will be deposited as the dark matter orbit shrinks further through the crust. Using the fact that the crust thickness $d_{\rm crust} \ll R_\star$, and taking the difference in the binding energies at the top and bottom of the crust, we find,

$$\begin{aligned}\Delta E_{\rm crust} &= m_{\rm DM}\left(\sqrt{1-\frac{2GM_\star}{R_\star}}-\sqrt{1-\frac{2GM_\star}{R_\star-d_{\rm crust}}}\right)\\ &\simeq m_{\rm DM}\frac{(1-\gamma^{-2})}{2\gamma}\frac{d_{\rm crust}}{R_\star}+\mathcal{O}\left(\left(\frac{d_{\rm crust}}{R_\star}\right)^2\right)\,,\end{aligned} \tag{3.17}$$

which is a small fraction of the dark matter kinetic energy at the star surface, $m_{\rm DM}(\gamma-1)$. Here we have used the expression for the binding energy at the star surface for the interior as well. Even though the metric in this region deviates from the typical Schwarzschild metric for a concentrated mass, this is a good approximation since the crust is very thin compared to the star.

The net energy that dark matter deposits in the crust during this process is

$$\Delta E_{\rm orbit} = (m_{\rm DM} + m_{\rm DM} v_{\rm halo}^2/2) - (m_{\rm DM}/\gamma)\ , \tag{3.18}$$

where the term in the first parentheses is the energy of the particle far away from the star, and the term in the second parentheses is its gravitational binding energy at the star surface. Eqs. (3.1) and (3.18) imply that the fraction of dark matter kinetic energy deposited in the crust $\Delta E_{\rm orbit}/E_{\rm DM}$ (with $v_{\rm halo}^2 \ll 1$ neglected) is given by

$$\kappa_{\rm crust} = \frac{1}{\gamma}\ . \tag{3.19}$$

The neutron star crust then radiates heat from the surface at a rate equal to the kinetic heating rate, with $\kappa = \kappa_{\rm crust}$ in Eq. (3.5). The dark matter heating temperature obtained from this luminosity is

$$T_\infty^{\rm crust} = 1620\ {\rm K}. \tag{3.20}$$

This is again much greater than the $\mathcal{O}(100)$ K temperatures expected without dark matter heating. In an optimal scenario, it may be possible to discern between crust vs. core heating using a population of old neutron stars, see [174] for details.

So far, we have only discussed the energetics of the dark matter capture process. Below, we investigate in detail dark matter scattering on the components of the various layers of the neutron star crust previously outlined. We then proceed to estimate the associated sensitivity to dark matter capture for each of these layers.

3.2.3 Scattering with the Outer Crust

In the outer crust, where nuclei form an ordered lattice, dark matter scattering on individual nucleons in the nuclei can result in dark matter capture. The nuclear binding energy per nucleon is roughly the same as that measured at laboratory densities: $E_{\rm bind} \lesssim 10$ MeV [215], which decreases deeper into the crust, where nuclei become heavier and richer in neutrons. For $m_{\rm DM} \gtrsim 10$ MeV, dark matter would scatter on these weakly bound nucleons by transferring energies greater than $E_{\rm bind}$. To calculate the per-nucleon capture cross section in the outer crust, we integrate Eq. (3.9) over the outer crust densities, which are from 10^6 g/cm^3 to $\rho_{\rm ND} \simeq 4.2 \times 10^{11}$ g/cm^3.

The per-nuclear cross section for dark matter scattering on a nuclear species T is given by

$$\sigma_{{\rm T}\chi}(q) = \left(\frac{\mu_{{\rm T}\chi}}{\mu_{{\rm n}\chi}}\right)^2 A^2 F^2(q) S_{\rm T}(q) \sigma_{{\rm n}\chi}, \tag{3.21}$$

where $\mu_{\mathrm{T}\chi}$ ($\mu_{\mathrm{n}\chi}$) is the nucleus-dark matter (nucleon-dark matter) reduced mass, q is the momentum transferred to the nucleus, $F(q)$ is the Helm form factor [115, 116], and $S_{\mathrm{T}}(q)$ is the static structure function per nucleus [119], which has been computed for dense astrophysical plasmas [120, 216]. To calculate the per-nuclear capture cross section in the outer crust, we substitute Eq. (3.21) into Eq. (3.9) and integrate over the outer crust densities, which are from 10^6 g/cm^3 to $\rho_{\mathrm{ND}} \simeq 4.2 \times 10^{11}$ g/cm^3. Here the number density in Eq. (3.9) is simply $n(\rho) = \rho/m_n$.

Scattering on the nuclei in the outer crust is unlikely to result in dark matter capture, due to the interplay of two factors,

- When the inverse momentum exchange q^{-1} is less than the nuclear radius r_a, there is loss of coherence over a nucleus, captured by the form factor $F(q)$ which suppresses $\sigma_{\mathrm{T}\chi}$.
- When the inverse momentum exchange q^{-1} is greater than the inter-nuclear separation a, there is loss of coherence among the relative amplitudes of dark matter scattering on multiple nuclei, captured by $S_{\mathrm{T}}(q)$, which suppresses $\sigma_{\mathrm{T}\chi}$ [213].

This can be seen explicitly by considering the relevant parameters for neutron stars: Nuclear radii in the outer crust are approximated by the standard formula $r_a \simeq (1.25 \text{ fm } A^{1/3}) \gtrsim 0.04 \text{ GeV}^{-1}$ [178]. The inter-nuclear separation for nuclear species with mass m_{T} in the outer crust is $a \sim (\rho/m_{\mathrm{T}})^{1/3} \gtrsim 0.02 \text{ GeV}^{-1}$. The average momentum transfer $\langle q \rangle \sim m_{\mathrm{DM}} \gamma v_{\mathrm{esc}}$ for $m_{\mathrm{DM}} \ll m_{\mathrm{T}}$, where $m_{\mathrm{T}} \sim 50$ - 200 GeV; see Fig. 3.2. Comparing the above distance scales to $\langle q \rangle^{-1}$, we find that for $m_{\mathrm{DM}} \gtrsim 30$ MeV, the scattering cross section is suppressed by $F(q)$, whereas for lighter dark matter, it is suppressed by $S_{\rm T}(q)$. For $m_{\rm DM} \gtrsim m_{\rm T}$, $\langle q \rangle \sim m_{\rm T}\gamma v_{\rm esc} \gtrsim r_a^{-1}$, so that the cross section is suppressed again by $F(q)$. Thus, the product $F^2(q)S_a(q)$ in Eq. (3.21) suppresses $\sigma_{{\rm T}\chi}$ for practically all dark matter masses. Therefore, in the outer crust, dark matter capture occurs mostly via scattering on individual nucleons, and not via scattering on nuclei.

3.2.4 Scattering with the Inner Crust

In the inner crust, dark matter capture can occur via scattering in two different ways: with nucleons weakly bound in nuclei, and with superfluid neutrons.

For interactions with nucleons, the greater densities in the inner crust imply that the binding energy per nucleon is even smaller than in the outer crust. Once again, therefore, dark matter scattering on weakly bound nucleons can result in capture for $m_{\rm DM} \gtrsim 10$ MeV. To calculate the capture cross section via scattering on nucleons in the inner crust, we again integrate Eq. (3.9), but now integrate over inner crust densities, which are from $\rho_{\rm ND}$ to 0.1 ρ_0. We will expect the capture cross section here to be 1 - 2 orders of magnitude smaller than the outer crust, due to the greater densities of the inner crust, which make it optically thicker. We note that like the outer crust, in the inner crust dark matter scattering with whole nuclei is suppressed. This can be seen by applying the outer crust arguments in the previous section with parameters for nuclei in the inner crust, where nuclear radii are instead well-approximated by $r \propto Z^{1/3}$.

In the inner crust, dark matter could also be captured by depositing energy on the free/dripped neutrons, which form a superfluid phase at the low stellar temperatures ($\mathcal{O}(10^3$ K$)$) that we consider. This phase has an energy gap of $\Delta_F \simeq 1$ MeV [217];

therefore for $m_{\rm DM} \gtrsim 10$ MeV, scattering on individual nucleons can unquestionably proceed. One might also consider dark matter capture through the breaking of neutron Cooper pairs [218], formed by spin-paired neutrons in superfluid neutron matter in the inner crust [219, 165, 220]. The pairing energies are expected to be ~ 0.01 - 0.1 MeV, although the dynamics and energy gaps for Cooper pairs in superfluid neutron matter are uncertain as they depend on many factors such as polarization contributions to the spin interactions of neutrons [221]. This is a topic of active research [222], and so to be conservative we leave a detailed treatment of dark matter capture via breaking inner crust neutron Cooper pairs to future work.

For dark matter masses much less than the energy or pairing gaps, dark matter can still deposit energy by exciting neutron superfluid quasi-particles such as phonons. Prior work specifically considered light dark matter's effect on the thermal conductivity of young, hot ($T \gtrsim 10^7$ K) neutron stars [167]. Here we will only provide a rough estimate of dark matter capture by phonon modes. Single-phonon emission in the low momentum regime with a linear dispersion relation is described by a static structure function, which relates the per-nucleon cross section to the phonon excitation cross-section [165, 167]:

$$S_{\rm phonon}(q) = \frac{q}{2 m_{\rm n} c_{\rm s}}, \tag{3.22}$$

where $c_{\rm s}$ is the speed of the superfluid phonon which at leading order is the neutron Fermi speed equal to $(3\pi^2 n_{\rm n})^{1/3}/m_{\rm n}$, where $\simeq\ 0.04\ c$ at the neutron drip density. We note that this linear regime, valid for sufficiently low momentum dark matter, does not account for possible contributions from higher energy excitations (*e.g.* maxons, rotons). For this reason, we will only consider low mass (and correspondingly low momentum) dark matter parameter space. Put another way, we require that

$S_{\rm phonon}(q)$ in Eq. (3.22) is much less than unity, which for $q \simeq \gamma v_{\rm esc} m_{\rm DM} \simeq m_{\rm DM}$ is valid for $m_{\rm DM} \lesssim 10^{-3}$ GeV. Future work could be undertaken to compute higher mass dark matter capture via phonon excitations, although this will depend on the specifics of the crust model. Finally, we note that we have been conservative in our choice of sound speed $c_{\rm s} \simeq 0.04\ c$. While we have neglected possible mixing between the superfluid phonons and nuclear lattice phonons, including this effect would tend to decrease the sound speed of the lowest lying modes by up to a factor of 4 [223], and result in capture cross sections proportionally smaller. We leave the full treatment of these effects to a future study as well.

Where Eq. (3.22) is valid, the energy deposited by dark matter via exciting phonons is $\sim qc_{\rm s}$. For dark matter masses much less than the neutron mass, the momentum transfer q is about $m_{\rm DM}\gamma v_{\rm esc}$. This means that this deposited energy is much greater than the dark matter kinetic energy $\gamma m_{\rm DM} v_{\rm halo}^2/2$, and so dark matter will be captured via excitation of a single phonon. Therefore, accounting for the factor $S_{\rm phonon}(q)$, the capture cross section for scattering via phonon emission is equal to 10^{-39} cm^2 (1 MeV$/m_{\rm DM}$) for dark matter masses less than the energy gap $\Delta_F = 1$ MeV.

3.2.5 Scattering with Nuclear Pasta

We now discuss our "*penne trap*" [224] for dark matter. The cross section for dark matter scattering on nuclear pasta is given by

$$\sigma_{\rm pasta}(q) = S_{\rm pasta}(q)\ \sigma_{{\rm n}\chi}\ , \tag{3.23}$$

where $S_{\rm pasta}(q)$ is a structure or response function accounting for correlations between nucleons in the pasta. Here we have neglected the per-proton cross section on the right hand side of the equation since the contribution to $S_{\rm pasta}(q)$ from neutron-neutron correlations will dominate over neutron-proton and proton-proton correlations as neutrons outnumber protons in nuclear pasta by $\mathcal{O}(100)$; see for instance Fig. 3.2.

Nuclear pasta has important implications for the properties of neutron stars and core collapse supernovae. For example, neutrino-pasta interactions impact neutrino opacity in supernovae, and electron-pasta interactions impact properties such as the neutron star shear viscosity, thermal and electrical conductivity. As such, the static response functions of neutrino and electron scattering with pasta have been previously calculated in several simulations [225, 226, 227, 228, 229, 230, 231, 232]. We apply the Quantum Molecular Dynamics (QMD) simulation results [233], as these are relevant for our stellar temperatures and dark matter momentum transfers.

The QMD results of Ref. [233] provide the low-temperature structure factor for several densities (and so several pasta phases) with a proton fraction of $Y_p = 0.3$, and only the gnocchi phase when the proton fraction is $Y_p = 0.1$. We note that the proton fraction of beta-equilibrated matter in a cold inner crust is about 0.1, which is the type of crust relevant for our calculation. However, as we consider only the neutron-neutron correlations, a 0.1 - 0.3 variation in proton fraction is expected to yield comparable results. As the gnocchi scattering structure factor is provided at both densities, we have checked that dark matter-gnocchi scattering cross sections with 0.1 and 0.3 proton fractions produce the same results. Given this, we expect that lasagna and spaghetti scattering will also be similar for 0.1 and 0.3 proton fractions, and so use the available $Y_p = 0.3$ proton fraction results for those pasta phases.

In any case, it is important to note that the treatment of pasta structure factors only significantly impacts the nucleon scattering enhancement visible in Fig. 3.3 for dark matter masses 0.1 - 1 GeV. This is because for most of the parameter space, capture occurs through inelastic ejection of nucleons out of nuclear pasta; this process is insensitive to the coherent pasta scattering enhancement. Ideally, we would sample several datasets to examine the variations in this coherent pasta-scattering enhancement, but as these datasets are not available, we provide estimates here. Neglecting this pasta coherent enhancement altogether would simply result in no dip in the nucleon pasta sensitivity curve around DM masses 0.1 - 1 GeV.

The QMD simulations capture the coherence effects of interacting with the whole pasta structure. Thus, σ_{pasta} must be interpreted as a *per-nucleon* cross section.

For sub-nuclear densities, the response $S_{\text{pasta}}(q)$ can be roughly divided into three regimes in q [233]:

- $q \lesssim 40$ MeV: The response function $S_{\text{pasta}}(q) \ll 1$, as the scattering is incoherent due to density fluctuations, which results in destructive interference of scattering amplitudes. In this region it is given by $S_{\text{pasta}} \to T(\partial\rho/\partial P)_T$, where T is the pasta temperature. For example, at $T = 1000$ K, $S_{\text{pasta}}(q)$ is $\mathcal{O}(10^{-6})$.
- $q \simeq 60$ MeV: The response function $S_{\text{pasta}}(q)$ peaks, due to coherent enhancement from scattering on multiple nucleons.
- $q \gtrsim 200$ MeV: The response function $S_{\text{pasta}}(q) \to 1$, corresponding to quasi-elastic scattering on weakly bound individual neutrons.

To calculate the dark matter-pasta scattering sensitivities, we modify Eq. (3.9) for the pasta layers as

$$\tau_{\rm DM} = \frac{\sigma_{\rm n\chi}}{g_s} \int_{\rm pasta} \langle S_{\rm pasta}(q) \rangle_q \, \frac{n_{\rm n}(\rho)}{\rho} \frac{dP}{d\rho} d\rho \ , \tag{3.24}$$

where $n_{\rm n}$ is the nucleon number density. The q-averaged structure function is given by

$$\langle S_{\rm pasta}(q) \rangle_q = \frac{1}{q_{\rm max}} \int_0^{q_{\rm max}} S_{\rm pasta}(q) \ dq \ , \tag{3.25}$$

with the maximum momentum transfer

$$q_{\rm max} = \sqrt{\frac{4\mu_{\rm n\chi} m_{\rm DM}^2 m_{\rm n} \gamma^2 v_{\rm esc}^2}{m_{\rm DM}^2 + m_{\rm n}^2 + 2 m_{\rm DM} m_{\rm n} \gamma}} \ . \tag{3.26}$$

We then integrate Eq. (3.24) over the pasta layer densities, which extend from 0.1 ρ_0 to 0.3 ρ_0. This range is a conservative choice, as various pasta structures are expected to appear near the saturation density ρ_0, which may contribute to dark matter capture via quasi-elastic scattering on individual nucleons. Thus our range of integration includes nuclear spheres (gnocchi), cylinders (spaghetti) and slabs (lasagna), but not cylindrical (bucatini) and spherical (Swiss cheese) voids [227, 229].

3.2.6 Projected Constraints on Dark Matter Interactions

3.2.6.1 Optical depths

We first present the optical depth of each layer by integrating over the appropriate density ranges, as laid out in Eq. (3.9),

$$
\begin{aligned}
\tau_{\mathrm{DM}}^{\mathrm{outer}} &\simeq \left(\frac{\sigma_{\mathrm{n}\chi}}{2\times 10^{-40}\ \mathrm{cm}^2}\right) , \\
\tau_{\mathrm{DM}}^{\mathrm{inner}} &\simeq \left(\frac{\sigma_{\mathrm{n}\chi}}{7\times 10^{-42}\ \mathrm{cm}^2}\right) , \\
\tau_{\mathrm{DM}}^{\mathrm{pasta}} &\simeq \left(\frac{\sigma_{\mathrm{n}\chi}}{10^{-42}\ \mathrm{cm}^2}\right) .
\end{aligned} \tag{3.27}
$$

We have normalized the per-nucleon cross sections so that the optical depth is unity, which corresponds to the spin-independent cross section required for dark matter capture in each layer, for dark matter masses 10 - 10^6 GeV, as seen in Fig. 3.3.

3.2.6.2 Layer by Layer Results

Fig. 3.3 summarizes our results for dark matter capture in neutron star crusts. In the top panel, we have plotted the per-nucleon capture cross section for $m_{\mathrm{DM}} \lesssim 1$ MeV, and in the bottom panel where $m_{\mathrm{DM}} \gtrsim 10$ MeV, we have plotted the same accounting for scattering in all the layers of the crust. Our results can be summarized as follows:

- <u>$m_{\mathrm{DM}} \gtrsim 90$ MeV:</u>

  This is the mass range in which capture could occur in all crustal layers. In general, the sensitivity to dark matter capture is driven by the pasta layers. This is mainly because, even though the pasta layers are very thin, their enormous densities give them enormous optical thickness.

  For 100 MeV $\lesssim m_{\mathrm{DM}} \lesssim 1$ GeV, dark matter-pasta scattering is coherently enhanced, which improves capture sensitivity by as much as an order of magnitude.

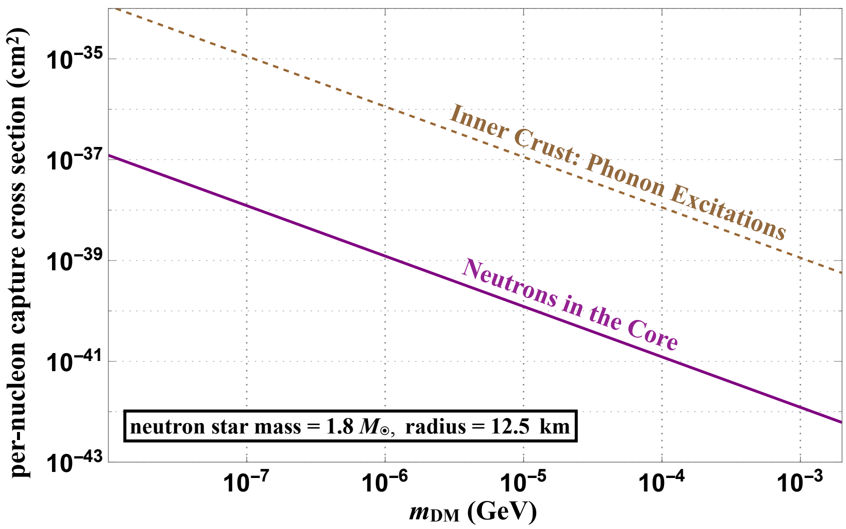

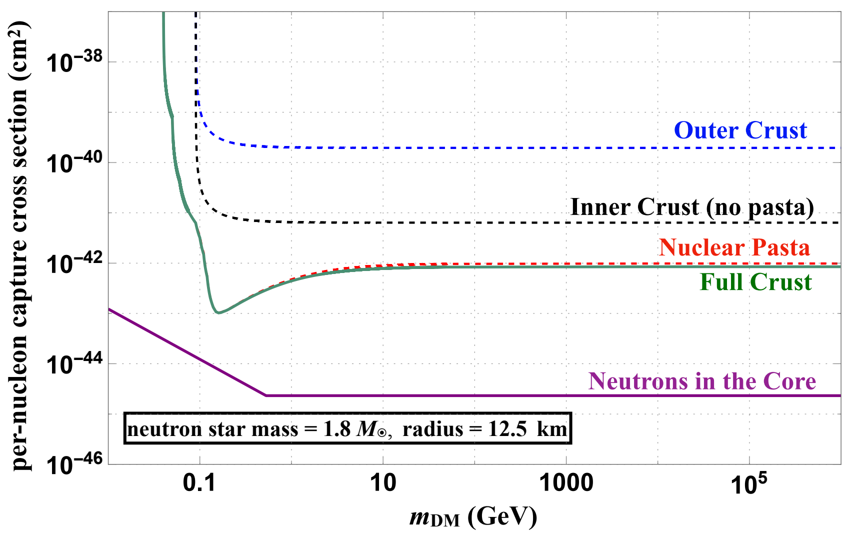

Figure 3.3: Dark matter-nucleon scattering cross section for capture by neutron star layers as a function of dark matter mass $m_{\rm DM}$, for a neutron star of mass 1.8 $M_\star$ and radius 12.5 km. **Top:** For $m_{\rm DM} \lesssim$ MeV, dark matter captures by scattering on superfluid neutrons in the inner crust and exciting collective modes (phonons) via low momentum transfers. **Bottom:** For $m_{\rm DM} \gtrsim 100$ MeV, dark matter captures by exciting weakly bound nucleons in the nuclei of the outer and inner crust, as well as in nuclear pasta at the bottom of the inner crust. In the inner crust, scattering on free neutrons also contributes to capture. Also shown is an estimate of the capture cross sections for dark matter scattering with the neutron star core assuming degenerate neutron matter; however the dynamics of the core are not reliably known.

For 90 MeV $\lesssim m_{\rm DM} \lesssim$ 400 MeV, a fraction of scatters can occur with energy transfer greater than 10 MeV (the nuclear binding energy of nucleons), as determined from the spectrum in Eq. (3.10). Thus the capture cross section decreases with $m_{\rm DM}$ in this mass range. Finally, for $m_{\rm DM} \gtrsim$ 400 MeV, almost all scatters occur with energy transfer greater than the nuclear binding energy 10 MeV, so that the capture cross sections of the outer crust and pasta-free inner crust are $m_{\rm DM}$-independent in this mass range.

- <u>10 MeV $\lesssim m_{\rm DM} \lesssim$ 90 MeV:</u>

  Dark matter capture by pasta is suppressed by incoherent scattering due to density fluctuations, so that the net capture sensitivity is driven by dark matter scattering on nucleons in the inner crust. The outer crust sensitivity is weaker than these layers' by 1 - 2 orders of magnitude simply because it is much less dense.

  In this mass range, there are no scatters with energy transfer greater than the nuclear binding energy 10 MeV, as seen from Eqs. (3.10) and (3.11). Therefore, capture via scattering on weakly bound nucleons shuts off, seen as vertical lines in the bottom panel of Fig. 3.3.

- <u>10 eV $\lesssim m_{\rm DM} \lesssim$ 1 MeV:</u>

  Sensitivity to dark matter capture in the crust is driven solely by the excitation of collective modes (phonons) in the neutron superfluid phase of the inner crust. In this region, both the crust and core sensitivities scale as $m_{\rm DM}^{-1}$ since the cross sections for both phonon excitation in the inner crust (Eq. (3.22)) and neutron excitation in the degenerate core contain a factor of the momentum transfer proportional to the dark matter mass. Our estimates of capture in this region are valid down to $m_{\rm DM} \simeq 10$ eV, for which dark matter evaporation may become important for a 1000 K-hot neutron star [234].

Note that we do not show sensitivities in the mass range 1 MeV - 10 MeV. The capture calculations in this range are much more complicated than our current, conservative treatment; this is a region where the dark matter masses are greater than the superfluid energy gap $\simeq 1$ MeV, and less than the per-nucleon binding energy $\simeq 10$ MeV. We leave a detailed treatment of this mass range for future investigation.

Remarkably, we see from the dark matter-core scattering bounds in Fig. 3.3, that the cross section sensitivity of neutron star crusts to dark matter kinetic heating is at most only 3 orders of magnitude weaker than that of the neutron star core. The latter scales as $m_{\rm DM}^{-1}$ for $m_{\rm DM} \lesssim 1$ GeV due to Pauli-blocking of degenerate neutrons [172]. Indeed, because of a structure factor enhancement in the pasta phase, the crust sensitivity is only a factor of 10 below the core sensitivity for $m_{\rm DM} \simeq 100$ MeV.

The separation of 3 orders of magnitude between the sensitivities of the pasta (without coherent enhancement) and core layers can be understood simply from their respective optical depths. From Fig. 3.1 and the discussion in Sec. 3.1, we see that the inner crust is $\mathcal{O}(10)$ less dense and $\mathcal{O}(10^2)$ thinner than the core, so that its optical depth is $\mathcal{O}(10^3)$ smaller. Similarly we see from Fig. 3.1 that the inner crust excluding pasta is $\mathcal{O}(10)$ less dense than, but about as thick as the pasta layer; therefore the inner crust optical depth is $\mathcal{O}(10)$ smaller, which is reflected in Fig. 3.3. Furthermore, the densest part of the outer crust is 1 - 2 orders of magnitude less dense than the inner crust on average, while of comparable thickness; therefore its optical depth (and hence cross section sensitivity in Fig. 3.3 is 1 - 2 orders of magnitude smaller.

It is important to keep in mind that any of the crust layers could be responsible for the capture of dark matter, due to the order in which it would encounter the layers in its first transit through the crust. Thus if the dark matter-nucleon cross section $\sigma_{n\chi}$ happens to exceed twice the outer crust capture cross section, then dark matter capture is effected by the outer crust; if $\sigma_{n\chi}$ is between twice the capture cross sections of the outer crust and a deeper layer, capture is effected by that deeper layer.

It is also important to note that our knowledge of neutron star structure becomes more theoretical and less empirical deeper into the star. Consequently, our cross section sensitivities are more robust for shallower layers, so that the outer crust sensitivity at about 10^{-40} cm^2 is the most robust. This is simply because we understand less well how matter should behave at higher densities and pressures. For example, while almost all equations of state predict a pasta phase, there are uncertainties in the types of pasta present, as well as the density at which they appear [235].

Here we have used the pasta structure function as given in Ref. [233], which computed it for neutron stars in the low temperature regime relevant in this study. Importantly, even in a scenario with no pasta structure function enhancement, there would still be densely packed nuclear material, whose nucleons dark matter would still scatter on quasi-elastically. We emphasize that the only region in which the pasta uncertainties are relevant is for dark matter masses of about 0.1 - 1 GeV, where scattering is enhanced by the structure function. Neglecting pasta altogether would simply remove the dip in sensitivity around these masses, evident in Fig. 3.3. This would weaken the predicted dark matter-nucleon scattering sensitivity in the 0.1 - 1 GeV mass range by less than an order of magnitude. For dark matter masses greater than a GeV, scattering on the nuclear pasta layers occurs predominantly through inelastic scattering with nucleons, as given by Eq. (3.39), which does not depend on the nuclear pasta structure function.

The results we have presented have an important consequence for weakly interacting (WIMP) dark matter candidates: as they have electroweak-sized scattering cross sections of about 10^{-39} cm^2 and GeV - TeV masses, they are guaranteed to be captured in neutron stars irrespective of the composition of the interior below the outer crust. Below, we revisit this aspect of capture in the context of inelastic dark matter, with a case study of supersymmetric Higgsino dark matter in Sec. 3.3.1.

3.2.6.3 Comparison with Direct Detection Limits

Fig. 3.4 directly compares our net crust sensitivity to constraints from underground experiments searching for dark matter in nuclear recoils, for both spin-independent and spin-dependent scattering [236, 237, 238, 239, 24]. We also show the xenon neutrino floor [34, 35], which denotes the cross section sensitivity below which neutrino backgrounds are expected to affect direct detection searches. The shaded "Full Crust" band denotes the uncertainties in capture cross section arising from varying the neutron star mass, radius, rotation frequency $f_{\rm rot}$, and equation of state (EoS). We did not consider neutron stars of mass $< 1.4 M_\odot$ as our equations of state predict for them a crust thickness $>$ 10% the size of the star, invalidating the light-and-thin crust approximation that we apply here. Neglecting this stellar mass range only leads to conservative results, as a thicker crust implies greater optical depth and hence stronger sensitivities. We find that the weakest sensitivity is provided by $\{M_\star = 2.3\ M_\odot,\ R_\star = 11.5\ \text{km},\ f_{\rm rot} = 716\ \text{Hz},\ \text{EoS} = \text{BsK21}\}$, and the strongest sensitivity by $\{M_\star = 1.4\ M_\odot,\ R_\star = 11.75\ \text{km},\ f_{\rm rot} = 0\ \text{Hz},\ \text{EoS} = \text{BsK20}\}$. We obtain these extremal parameter values from the mass-radius relations derived in [177] using the analyitic representations of the BsK equations of state.

We have estimated the spin-dependent capture cross section shown in Fig. 3.4 by

1. Scaling the spin-independent capture cross section by a factor of

$$\left[\frac{4}{3}\frac{J_n+1}{J_n}(\langle S_n\rangle + \langle S_p\rangle)^2\right]^{-1} \quad , \tag{3.28}$$

   where $J_n = 1/2$, $\langle S_n\rangle = 1/2$ and $\langle S_p\rangle = 0$ for scattering on neutrons, and

2. To calculate pasta scattering we have used the pasta structure factor in Eq. (3.24) but have imposed $S_{\text{pasta}}(q) \leq 1$, since we expect spin-dependent scattering to not be coherent over pasta nucleons, and

3. To calculate quasi-elastic scattering on nucleons in the inner and outer crust, we follow the same procedure as spin-independent scattering, since in this case scattering occurs with individual nucleons.

Although the PICO-60 limit applies to spin-dependent scattering on protons, we display it as it provides the current best sensitivity to spin-dependent dark matter interactions with nucleons at low dark matter masses. Furthermore, most spin-dependent models predict roughly equal rates of neutron and proton scattering.

For spin-independent scattering, we see that neutron crust heating is clearly more sensitive than direct detection for low dark matter masses ($m_{\text{DM}} \lesssim$ GeV); crustal capture easily proceeds for these masses, *cf*. Eq. (3.11), but at terrestrial experiments it is difficult to detect soft nuclear recoils above energy thresholds. Direct detection experiments benefit from an A^2 enhancement in cross section from nuclear coherence, which helps them surpass neutron star crust sensitivity in some range of m_{DM}. For spin-dependent scattering, we see that neutron crust heating is more sensitive than current direct detection searches for nearly all dark matter masses. We note that these statements hold true for sub-MeV dark matter masses as well, where neutron star crust heating occurs through phonon excitations, see Fig. 3.3. For complementary bounds on dark matter-nucleon scattering at low dark matter masses, see Refs. [240, 241, 242, 243, 244, 142].

For both spin-independent and dependent scattering, we have also shown the approximate optimistic reach of dark crustal heating. As old neutron stars are expected to be around 100 K-hot, assuming future optimistic experimental sensitivity, the neutron star would have to be heated by dark matter to higher than about 100 K to have a differentiable signal. This optimistic reach is shown as the dotted "100 K neutron star" curve.

3.2.6.4 Comparison with Outer Core Scattering

Lastly, we remark on dark matter capture via scattering with the outer core of the neutron star. This is the region marked by densities 0.5 - $2\rho_0$, to distinguish it from the inner core with densities $> 2\rho_0$, where exotic phases of matter are usually thought to appear. It is not clear that exotic phases do not appear at outer core densities as well [245, 122, 246, 247, 191]. In addition, the neutrons (protons) in the outer core are expected to exist in a superfluid (superconducting) phase, so that dark matter could only scatter by exciting collective modes at low momentum transfers.

Therefore, while scattering on the outer core is subject to the same uncertainties

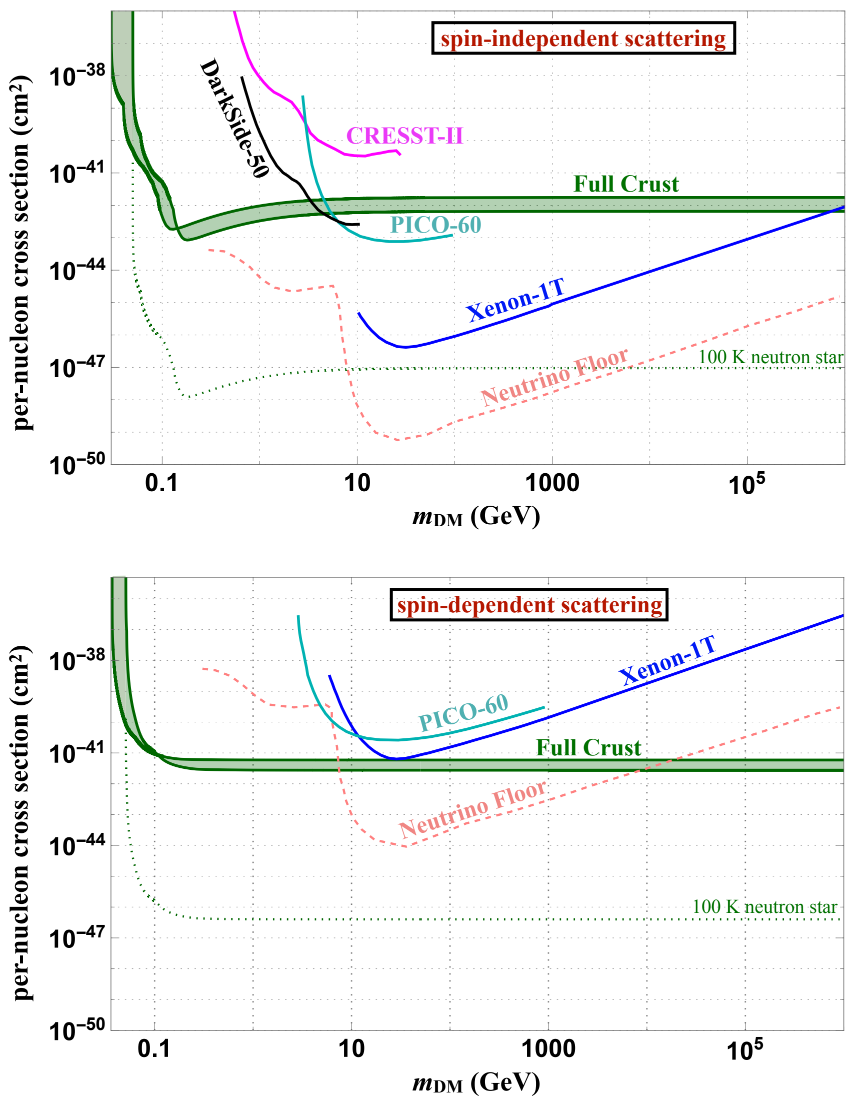

Figure 3.4: Comparison of net per-nucleon capture cross sections of neutron star crusts with constraints from underground dark matter direct detection searches, for spin-independent (**top**) and spin-dependent (**bottom**) scattering. Also shown are the xenon neutrino floors as a rough estimate of the ultimate sensitivity of direct detection experiments [34, 35]. The "Full Crust" shaded band spans the range of capture cross sections obtained by varying key properties of neutron stars, with the weakest sensitivity provided by {mass, radius, rotational frequency, high-density equation of state} = $\{2.3\ M_\odot$, 11.5 km, 716 Hz, BsK21}, and the strongest sensitivity by $\{1.4\ M_\odot$, 11.75 km, 0 Hz, BsK20}. "Full Crust" shows the cross-section for which all dark matter passing through the neutron star crust is captured, resulting in kinetic heating to ~ 1620 K; the cross-section for which DM kinetic heating leads to a "100 K neutron star" is also indicated. This is roughly the full optimistic reach.

as the inner core that were detailed previously, nevertheless for completeness' sake we estimate the capture cross section for the outer core with average density $\rho_{\rm OC}$ and thickness $d_{\rm OC}$ as

$$10^{-44}\ \mathrm{cm}^2 \left(\frac{1.5\rho_0}{\rho_{\rm OC}}\right)\left(\frac{5\ \mathrm{km}}{d_{\rm OC}}\right) \mathrm{Min}\left[1, \frac{p_{\rm Fermi}}{m_{\rm DM}\gamma v_{\rm esc}}\right]\ , \tag{3.29}$$

where the last term contains a Pauli-blocking factor for low momentum transfers, with $p_{\rm Fermi}$ the neutron Fermi momentum $\simeq 0.45$ GeV [172]. Because this estimate will be affected by any novel nuclear dynamics in the outer core, for the rest of this paper we will focus on dynamics in the sub-nuclear crust. We leave a thorough exposition of the outer core, and associated uncertainties, to future work.

3.3 Dark Annihilation Heating

As illustrated by Eq. (3.16), captured dark matter thermalizes through repeated scattering with the crust, and becomes confined to the volume underneath it, in a very short timescale. At this point, it will continue to oscillate in the stellar interior at semi-relativistic speeds. If the dark matter particles annihilate to Standard Model products, their mass energy is deposited into the star, heating it to temperatures even higher than that induced by kinetic heating. For instance, the temperature of our benchmark neutron star, *cf*. Eq. (3.2), due to dark matter kinetic-and-annihilation heating is

$$T_\infty = 2470\ \mathrm{K}\ . \tag{3.30}$$

This would have a significant effect on observational prospects at imminent infrared telescopes, in particular reducing the observation time by a factor of $\sim$10 and affecting the optimal choice of filters to be used. In this Section, we explore the possibility of dark matter annihilation post crustal capture in some detail, and show that hitherto-elusive scenarios such as supersymmetric Higgsino dark matter may be cornered thanks to this phenomenon.

The number of dark matter particles contained in the star evolves according to

$$\frac{dN}{dt} = C_{\rm DM} - \frac{\langle \sigma_{\rm ann} v \rangle N^2}{V} , \tag{3.31}$$

where $C_{\rm DM}$ is the capture rate given by $\dot{M}_{\rm DM}/m_{\rm DM}$ from Eq. (3.3), $\langle \sigma_{\rm ann} v \rangle$ is the thermally averaged dark matter annihilation cross section, and V is the volume in which annihilation occurs, which we conservatively take to be the volume of the star. The solution to the above is given by

$$N(t) = \sqrt{\frac{C_{\rm DM} V}{\langle \sigma_{\rm ann} v \rangle}} \tanh\left(\frac{t}{\tau_{\rm eq}}\right) , \tag{3.32}$$

where

$$\tau_{\rm eq} = \sqrt{\frac{V}{C_{\rm DM} \langle \sigma_{\rm ann} v \rangle}} \tag{3.33}$$

is the characteristic timescale at which capture and annihilation equilibrate, after which $N(t)$ achieves a steady state. For $t > \tau_{\rm eq}$ the net luminosity of the neutron star,from both kinetic and annihilation heating, is $(\dot{M}_{\rm DM} + \dot{E}_{\rm ann}) \propto C_{\rm DM} m_{\rm DM} \gamma$.

$\langle\sigma_{\rm ann}v\rangle$ can be expanded in terms of its partial wave contributions:

$$\langle\sigma_{\rm ann}v\rangle = (\sigma v)_0 \sum_{\ell=0}^{\infty} a_\ell v_{\rm rel}^{2\ell} \ , \tag{3.34}$$

where $v_{\rm rel}$ is the relative velocity of the annihilating dark matter particles, and $\ell = 0, 1, 2$ correspond respectively to the leading contributions from s-wave, p-wave, d-wave modes. For illustration we will consider scenarios where $\langle\sigma_{\rm ann}v\rangle$ is dominated by a single mode such that the coefficients $a_\ell = 1$ for that mode and $a_\ell = 0$ for all other modes. Note that the average relative velocity of dark matter particles oscillating within the star is approximately just the escape velocity, which is of order 0.1. Using the approximate scaling $C_{\rm DM} \propto R_\star^2$ from Eq. (3.3) and $V \propto R_\star^3$, we see from Eq. (3.33) that for annihilations dominated by the mode ℓ,

$$\tau_{\rm eq} \propto R_\star^{(3+\ell)/2} \ . \tag{3.35}$$

Fig. 3.5 shows τ_{eq} as a function of the radius of our benchmark 1.8 $M_\odot$ neutron star, for s-wave and p-wave dark matter annihilation. We limit the plot to radii $\lesssim$ 13 km since above that radius neutron stars are predicted to have masses $\lesssim M_\odot$, which are expected to have more massive and larger crusts, invalidating the light-and-thin crust approximation assumed throughout this work. We also remark that lighter neutron stars will be more efficient at capturing dark matter in their crusts since these have a greater optical depth. Here we fix $m_{\rm DM} = 1$ TeV and $(\sigma v)_0 = 3\times10^{-26}$ cm^3/s in Eq. (3.34), and assume a dark matter-nucleon cross section greater than 10^{-40} cm^2 so that all transiting dark matter is captured by the crust, as shown in Fig. 3.3. As borne out by the scaling relation in Eq. (3.35), the timescales shown would be shorter

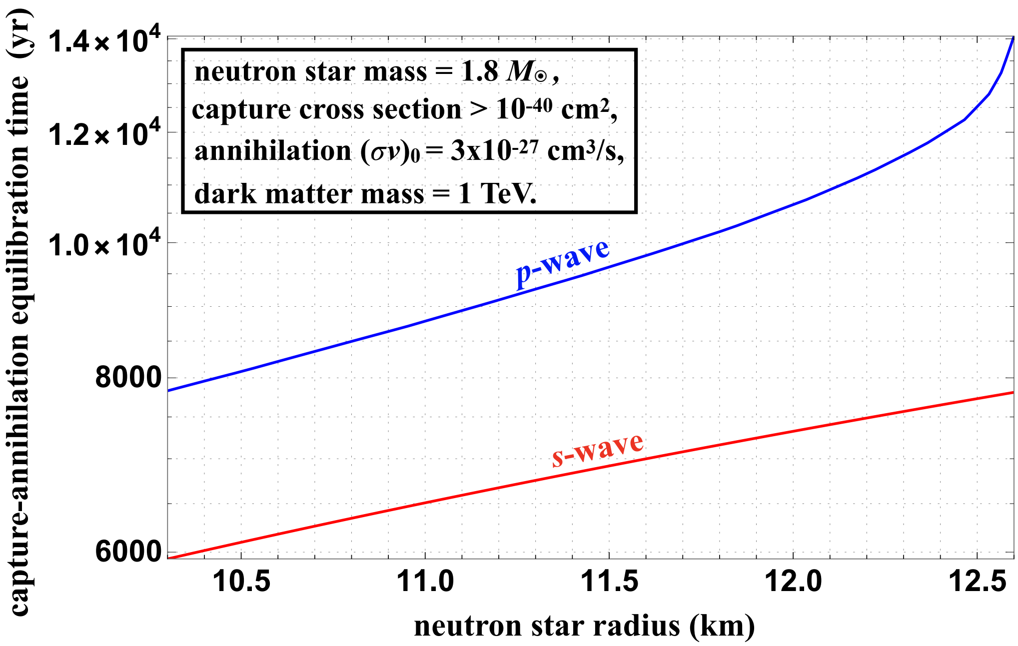

Figure 3.5: Capture-annihilation equilibrium timescale as a function of neutron star radius, for dark matter that fails to scatter and thermalize with the core of the star. The timescale for both s-wave- and p-wave-dominated annihilations are shown. Here we take the dark matter mass to be 1 TeV and a per-nucleon scattering cross section $> 10^{-40}$ cm^2, so that dark matter is guaranteed to capture in the crust (see Fig. 3.3); the scaling cross section $(\sigma v)_0$ in Eq. (3.34) is set to 3×10^{-27} cm^3/s.

for smaller neutron stars, and for annihilation dominated by smaller partial wave modes.

We now note that were dark matter to scatter and even just partially thermalize with the core of the star, $\tau_{\rm eq}$ for s- and p-wave annihilations would be even smaller than that predicted by crust-only thermalization. To see this, consider a partially thermalized ensemble of dark matter particles that is confined to a volume of radius $r_{\rm PT} < R_\star$. From the fact that the star's gravitational potential at this radius is $(3GM_\star/2R_\star)(1 - r_{\rm PT}^2/3R_\star^2)$, the typical dark matter speed scales as $v_{\rm rel} \propto r_{\rm PT}$. Using this and $V \propto r_{\rm PT}^3$ in Eq. (3.33), for dark matter annihilations dominated by the mode ℓ we have

$$\tau_{\rm eq} \propto r_{\rm PT}^{(3-2\ell)/2} \ . \tag{3.36}$$

Therefore for $\ell \leqslant 2$, the capture-annihilation equilibrium timescale scales positively with $r_{\rm PT}$: the smaller the thermalization volume, the quicker the equilibration. Conversely, for $\ell \geqslant 2$, this equilibration could take significantly longer for d-wave and higher-order modes. We could also, of course, verify this statement in the limit of fully thermalized dark matter. In that case, for a core density $\rho_{\rm NS}$ dark matter would settle into a "thermal volume" of radius $\ll$ the size of the star [112]:

$$r_{\rm thermal} = \sqrt{\frac{9T}{4\pi G \rho_{\rm NS} m_{\rm DM}}} \lesssim 10^{-2}\,{\rm km} \left(\frac{10^{15}\ {\rm g/cm^3}}{\rho_{\rm NS}}\right)^{1/2} \left(\frac{10^3\ {\rm GeV}}{m_{\rm DM}}\right)^{1/2} \left(\frac{T}{1000\ {\rm K}}\right)^{1/2} . \tag{3.37}$$

Since $v_{\rm rel} \propto \sqrt{T}$, the above equation implies $v_{\rm rel} \propto r_{\rm thermal}$ such that the scaling in Eq. (3.36) is once again true.

Some comments are in order regarding whether dark matter annihilation products efficiently heat the neutron star. So far we have assumed that this is the case. However, one might consider whether this holds if the annihilation products were neutrinos, whose mean free path in neutrons at saturation density $n_{\rm n} = 10^{37}$ cm^{-3} is [248]

$$L_\nu = (n_{\rm n} G_{\rm F}^2 E_\nu^2)^{-1} \simeq 10^{-1}\ {\rm m}\ \left(\frac{100\ {\rm MeV}}{E_\nu}\right)^2 , \tag{3.38}$$

where $G_{\rm F}$ is Fermi's constant and E_ν is the incident neutrino energy, equal to the dark matter mass for prompt $2 \to 2$ annihilations. From this we see that we should expect dark matter annihilation to neutrinos, for the masses we have considered, to result in efficient neutron star heating. Certainly for $m_{\rm DM} \gtrsim 100$ MeV these neutrinos do not escape the star, but rather scatter on the pasta layers of the inner crust and contribute to annihilation heating. In the future, it will also be interesting to consider dark matter annihihations to long-lived mediators [249, 250, 251, 252, 253, 254, 255, 256, 257, 258, 259, 260, 261, 262] or a second component of (nucleophilic) dark matter [263, 264, 265], which may also heat the crust rather than the core.

3.3.1 Discovery Prospects of Inelastic Higgsinos

Previously, we showed that dark matter capture by the neutron star crust alone is sufficient for capture-annihilation equilibrium to be attained within the lifetime of the star, for electroweak-sized annihilation cross sections. This means that the crust provides sensitivity to certain dark matter models that are difficult to probe at terrestrial experiments, such as dark matter that only scatters inelastically [266], and dark matter that scatters through velocity-suppressed interactions [267]. We remark that there has also been a recent complementary treatment of neutron star core capture of inelastic dark matter given in Ref. [268]. In this sub-section we illustrate this crust sensitivity to the supersymmetric Higgsino. This is a especially appealing dark matter model, as it originates from the supersymmetric extension of the Standard Model, and shares the same gauge symmetries and Yukawa couplings. As we detail below, after electroweak symmetry breaking, its lightest mass eigenstates that arise are stable and only interact through the weak force, they are thermally produced in the early universe, and furthermore their mass must be $\sim$ TeV to match the observed relic density of dark matter. This candidate can easily evade terrestrial detection, since its elastic scattering cross section against nucleons must be significantly smaller than the reach of direct detection experiments, whereas inelastic scattering is kinematically forbidden at the accessible phase space on Earth.

For inelastic scattering on nucleons in the crust (we neglect coherent scattering on pasta for the moment), dark matter of mass $m_{\rm DM}$ must scatter to an excited state of mass $m_{\rm DM} + \delta$, with the inelastic cross section given by

$$\sigma_{\rm n\chi} = \sigma^0_{\rm n\chi}\sqrt{1 - \frac{\delta}{\delta_{\rm max}}}, \tag{3.39}$$

where $\sigma^0_{\rm n\chi}$ is the (elastic) scattering cross section at vanishing mass splitting δ, and $\delta_{\rm max}$ is the maximum mass splitting for inelastic scattering to proceed, given by

$$\delta_{\rm max} = \frac{\mu_{\rm n\chi} v^2}{2}\ , \tag{3.40}$$

with $\mu_{\rm n\chi}$ the neutron-dark matter reduced mass and $v \simeq v_{\rm esc}$. For our benchmark star parameters, Eq. (3.2), we have $\delta_{\rm max} = 200$ MeV for $m_{\rm DM} \gg m_{\rm n}$. Note that at terrestrial detectors $v \simeq 10^{-3}$, so that for a 100 GeV-heavy scattering target and a heavier dark matter projectile, $\delta_{\rm max} \simeq 50$ keV. Thus neutron star crustal capture improves the "inelastic frontier" of dark matter direct detection by $2 - 3$ orders of magnitude.

Higgsinos are the fermionic supersymmetric partners of the Standard Model Higgs field, which undergo mass mixing with the superpartners of the weak gauge bosons ("binos" and "winos") after electroweak symmetry breaking. If the bino and wino are decoupled from the Higgsino by setting their mass parameters, denoted by M_1 and M_2 respectively, much greater than the Higgsino mass parameter μ, then a nearly pure Higgsino is a candidate for dark matter. Being an electroweak doublet, there are two neutral states at the mass scale μ, denoted by χ_1 (the dark matter state) and χ_2 (an excited state), as well as a charged Higgsino pair, $\chi^{\pm}$ (also potentially excited states). For expressions of the mass splittings between χ_1 and $\{\chi_2, \chi^{\pm}\}$ in terms of electroweak and supersymmetric parameters, see Ref. [172]. For Higgsino mass $\mu = 1.1$ TeV, Higgsino dark matter could be produced at the observed relic abundance, $\Omega_\chi h^2 = 0.11$, via thermal freeze-out from s-wave annihilations with $\langle \sigma_{\rm ann} v \rangle \simeq 3 \times 10^{-27}$ cm^2 [269].

When kinematically allowed, the Higgsino χ_1 can scatter inelastically to an excited state (by exchanging a Z or $W^{\pm}$ boson) with an electroweak-sized cross section $\sigma^0_{{\rm n}\chi} \simeq 10^{-39}$ cm^2 in Eq. (3.39). From Fig. 3.3, this implies that thermal Higgsino dark matter of mass 1.1 TeV will

1. be captured by the outer crust whose capture cross section $\simeq 10^{-40}$ cm^2; as mentioned in Sec. 3.2.6, as the outer crust is the most empirically understood layer, this is a robust prediction for electroweak dark matter such as the thermal Higgsino, and

2. further scatter with and deposit energy in the inner crust (including the pasta layer), whose capture cross section $\simeq 10^{-41}$ cm^2.

The above stages of capture would occur for most values of the mass splitting $\delta < \delta_{\rm max}$ in Eq. (3.39), and any deviations would only occur for δ within 1% of $\delta_{\rm max}$. Therefore, most of the thermal Higgsino parameter space corresponds to the curve in Fig. 3.5 denoting s-wave annihilations for $m_{\rm DM} = 1$ TeV, *i.e.* crustal capture implies that capture-annihilation equilibrium is expected in timescales of less than

10^4 years. This in turn implies that thermal Higgsino dark matter with inelastic mass splitting less than 200 MeV is practically guaranteed to give rise to both kinetic and annihilation heating of neutron stars, significantly increasing the prospects of its discovery.

As detailed throughout this Chapter, this result provides a key motivation for treating neutron star crusts as dark matter captors. Even if the stellar core were not exotic, dark matter scenarios like the supersymmetric Higgsino may never thermalize with the core through repeated scattering. This can happen for a number of reasons:

- As the Higgsino loses kinetic energy, $\delta_{\rm max}$ decreases (see Eq. (3.40)), so that inelastic scattering eventually becomes forbidden.

- In addition to inelastic scattering, Higgsino dark matter can also scatter *elastically* ($\chi_1 n \to \chi_1 n$) via a higher-order amplitude, however the cross section for this process is currently unknown, and only an upper bound has been computed [270, 271]: $\sigma(\chi_1 n \to \chi_1 n) \lesssim 10^{-48}$ cm^2 for $m_{\rm DM} = 1.1$ TeV.

As no lower bound exists on this cross section, the Higgsino might in principle never thermalize with the core within the present age of the universe. As a result, Higgsino dark matter may annihilate in a volume much larger than the thermal volume given by Eq. (3.37), *i.e.* much less efficiently. However, we have established that Higgsinos will annihilate anyway: even in the limit of capture in the crust and no thermalization with the core, capture-annihilation equilibrium is attained very quickly as shown in Fig. 3.5, so that annihilation proceeds at its maximal rate.

Chapter 4

Nuclear Recoil Signatures of Composite Dark Matter

Composite dark matter theories, whereby dark matter is an object made of smaller fundamental constituents, have gained increasing interest in recent times. A plethora of models have been proposed and are undergoing close scrutiny. Such candidates include fermionic dark matter blobs [272, 273, 274, 275, 276, 108, 109], glueballs [277, 278], dark quark nuggets [279, 280], massive compact mini-halos [281], bound axionic states [282, 283, 284, 285, 286, 287, 288], boson stars [289, 127, 290, 291, 292], massive compact mini-halos [281] and Q-balls [293]. Furthermore, some composite dark matter theories are even becoming the specific target of several experimental searches [42, 294, 295, 296, 27].

In this Chapter, we will review new signatures of composite dark matter recently uncovered in [108, 109]. These signatures arise from the strong binding field sourced by composite states which, when coupled to Standard Model nucleons, creates sizable nuclear recoils and a variety of related collisional processes in matter. These can range from sizeable heat dissipation and ionization, to even thermonuclear reactions, depending on the coupling strength. Moreover, this novel phenomenology can arise for unconstrained coupling values between the dark and visible sector, unlocking new parameter space to be tested by both experiments and astrophysical probes. While here we limit ourselves to one of the simplest existing models, these results could easily be generalized in the future to other composite dark matter theories.

4.1 Bound States of Dark Matter Fermions

The simplest model of composite dark matter that has been studied in [273, 297, 275, 274, 108], consists of a dark matter fermion (X) coupled to a real scalar field (ϕ) that provides an attractive force that binds the dark fermions together. The Lagrangian for this dark matter sector is

$$\mathcal{L}_D = \bar{X}(i\gamma^\mu \partial_\mu - m_X)X + g_X \bar{X}\phi X + \frac{1}{2}m_\phi^2 \phi^2 + \frac{1}{2}\partial_\mu \phi \, \partial^\mu \phi, \tag{4.1}$$

where the bound states we are interested in are composed of X (and not $\bar{X}$) particles, *i.e.* the dark matter is asymmetric [13, 12].

An attractive interaction is a necessary ingredient to form bound states in the early universe, as we discuss shortly. Note that while we restrict our attention to the Lagrangian above for simplicity, much of the work we will do could be easily extended to the case that there is an additional repulsive vector coupling between X, or even pseudo-scalar and pseudo-vector interactions. Such interactions would tend to alter the formation and structure of the dark matter composites, see *e.g.* [298]. In what follows we shall also assume a zero temperature limit for our composites, but point out that the results outlined here can be generalized to a finite temperature using appropriate thermal distribution functions, see *e.g.* [299].

We have recently shown that this dark matter model leads to a whole new phenomenology if the same scalar that binds the composite together has a small Yukawa coupling to Standard Model particles [108, 109]. As we review below, sufficiently massive composites will be in a saturated state; the binding field inside the saturated composites takes on a classical value $\langle\phi\rangle \propto m_X$, where m_X is the mass of the constituent dark matter fermion, here ranging from GeV - EeV. For a wide range of couplings, these dark matter composites will source a large scalar field value, which implies a large corresponding scalar potential $V \sim \langle\phi\rangle$ inside the composite. Nuclei and other Standard Model particles coupled to ϕ will undergo accelerative processes at the composite boundary. It follows that the composite's Yukawa potential will cause nuclei (or other Standard Model particles if also coupled) to scatter, ionize, and undergo other dynamic processes at the boundary and inside the dark matter composite.

4.1.1 Saturated Composite States

In general, the physical properties of bound states with a low number of particles pose a complex physical problem. However, when the number of constituents is large, one can apply relativistic mean field theory [274], and approximate the binding field by a classical uniform value $\phi(x) \to \langle\phi\rangle$. In this limit, simple scaling relations in terms of the constituent number N_X are recovered. The scalar field value inside the composite is determined by minimizing the energy density,

$$\varepsilon = \frac{1}{2}m_\phi^2\langle\phi\rangle^2 + \frac{1}{\pi}\int_0^{p_F} dp\; p^2\left(p^2 + m_*^2\right)^{1/2}. \tag{4.2}$$

In this expression, $m_* = m_X - g_X\langle\phi\rangle$ is the fermion effective mass inside the composite, which accounts for the X self-interactions. The upper integration limit is the Fermi momentum p_F, which implicitly depends on the scalar field expectation value in the composite, $\langle\phi\rangle$, via the chemical potential $\mu = (p_F^2 + m_*^2)^{1/2}$. In order to determine $\langle\phi\rangle$ by minimizing Eq. (4.2), the chemical potential must in turn be related to the energy density via $\mu = \varepsilon/n_X$, where $n_X = p_F^3/3\pi^2$ is the constituent number density. This is equivalent to requiring a vanishing pressure, since $p = -(\partial E/\partial V)_{N_X} = \mu\varepsilon - n_X$. In the limit $m_* \ll p_F$, simple scaling relations for the effective mass and chemical potential are recovered,

$$m_* \simeq (6\pi^2)^{1/2}\left(\frac{m_\phi}{g_X}\right), \tag{4.3}$$

$$\mu \simeq p_F \simeq (6\pi^2)^{1/2}\left(\frac{m_\phi}{g_X}\right)^{1/2}\left(\frac{m_X}{g_X}\right)^{1/2}. \tag{4.4}$$

It can be seen from the above expressions that $\mu \simeq p_F \gg m_*$, and so the constituents are effectively relativistic while in the bound state. This is especially relevant for computing nucleus-constituent scattering, see Sec. 4.1.4 below. The binding energy per constituent is set by the difference $m_X - \mu$, and related to the total composite mass via

$$M_X = N_X m_X - N_X(m_X - \mu) = N_X\mu. \tag{4.5}$$

Using a standard "liquid drop" model, the total composite mass is made up of a bulk and surface contribution $M_X = N_X\bar{m}_X + N_X^{2/3}\epsilon_{\rm surf}$, where $\bar{m}_X$ is the amount of composite mass per constituent, which accounts for their binding energy, and $\epsilon_{\rm surf}$ is a coefficient associated with the decrease of interactions near the composite boundary. This relation implies that the chemical potential scales as $\mu = \bar{m}_X + N_X^{-1/3}\epsilon_{\rm surf} \simeq \bar{m}_X$ in the limit of large N_X. Thus, from here onward we will take the composite mass as

$M_X \simeq N_X \bar{m}_X$, and because the constituents are relativistic, the mass they contribute to the composite is simply $\bar{m}_X \simeq \mu$, which for relativistic constituents will be their Fermi momentum, $\bar{m}_X \simeq (6\pi^2 m_\phi m_X)^{1/2}/g_X$ as given by Eq. (4.4). The composite radius is consequently,

$$R_X = \left(\frac{9\pi N_X}{4\bar{m}_X^3}\right)^{1/3}, \tag{4.6}$$

where the scaling indicates that the composite volume is proportional to the composite mass. Therefore, the addition of an extra particle simply enlarges the composite so that the number density remains constant. This saturation number density is

$$n_X = \frac{\bar{m}_X^3}{3\pi^2} \simeq 10^{41}\ \mathrm{cm}^{-3}\ \left(\frac{\bar{m}_X}{5\ \mathrm{GeV}}\right)^3. \tag{4.7}$$

Composites with a number density exceeding the above expression will be well-described by the mass and radius relations given above. Of course it is often preferable to quantify the minimum number of dark matter constituents which render the above approximations to be accurate. As discussed extensively in [274], the saturation regime can be defined as the limit where the composite length scale R_X becomes comparable to the mediator range m_ϕ^{-1}, implying that a composite state must contain a minimum

$$N_X \simeq \left(\frac{\bar{m}_X}{m_\phi}\right)^3 \simeq 10^{10}\ \left(\frac{\alpha_X}{0.3}\right)^{\frac{3}{4}} \left(\frac{m_X}{\mathrm{TeV}}\right)^{\frac{3}{2}} \left(\frac{m_\phi}{\mathrm{MeV}}\right)^{-2} \tag{4.8}$$

of dark matter constituents for it to be saturated. Shortly, we will see that by the time that the cosmological synthesis of these composites ceases, the typical particle numbers N_X are well above this saturation threshold.

4.1.2 Early Universe Synthesis

The cosmological formation of large asymmetric composite states has been explored in previous works [297, 300, 275, 108]. In the case of the composite dark sector indicated by Eq. (4.1), composite synthesis occurs in the early universe when the dissociation of two-body bound states by ϕ-scattering becomes inefficient as the universe cools. Formation of two-body bound states will occur provided that [297]

$$\alpha_X^2 m_X \gtrsim m_\phi, \tag{4.9}$$

and

$$\alpha_X \gtrsim 0.3 \left(\frac{m_X}{10^7\,\mathrm{GeV}}\right)^{\frac{2}{5}} \left(\frac{\zeta}{10^{-6}}\right)^{\frac{1}{5}}, \tag{4.10}$$

with $\alpha_X = g_X^2/4\pi$. The parameter $\zeta \ll 1$ is a dilution factor that ensures the observed dark matter relic abundance is attained at the end of synthesis. We specify its origin a few lines below. Once two-body bound states are formed, synthesis of larger composites proceeds via inelastic fusion processes, with cooling of the final composite usually occurring via ϕ emission. In the strong binding regime $\bar{m}_X \ll m_X$, the composites will build up in size via dark fusion reactions of the form ${}^{N_X}X + {}^{N_X}X \to {}^{2N_X}X + \phi$, until their rate drops below the expansion rate of the universe. For masses $m_X \gtrsim$ TeV, this results in an overabundance of dark matter. However, the correct relic abundance can be recovered assuming the excess is subsequently depleted by the decay of a metastable field [113], as was recently shown in [108]. Such a late-time relic density depletion via decaying fields is present in many models of high-scale baryogenesis [301, 302]. The amount of asymmetric dark matter (and baryons) that is depleted, is given by $\Omega_X^{\mathrm{dep}} = \Omega_X \zeta$, where $\zeta = s_{\mathrm{after}}/s_{\mathrm{before}}$ is the entropy ratio before and after the field decays. Conversely, the abundance of dark matter constituent particles X after freeze-out is in excess of the standard value by a factor of ζ^{-1}, leading to the formation of large composite states. The number of dark matter of particles contained in a composite formed by this process is [108],

$$\begin{aligned} N_c &= \left(\frac{20\sqrt{g^*_{ca}} T_r T_{ca}^{3/2} M_{pl}}{\bar{m}_X^{7/2} \zeta} \right)^{6/5} \\ &\simeq 10^{27} \left(\frac{g^*_{ca}}{10^2} \right)^{\frac{3}{5}} \left(\frac{T_{ca}}{10^5\,\mathrm{GeV}} \right)^{\frac{9}{5}} \left(\frac{5\,\mathrm{GeV}}{\bar{m}_X} \right)^{\frac{21}{5}} \left(\frac{10^{-6}}{\zeta} \right)^{\frac{6}{5}}, \end{aligned} \tag{4.11}$$

where $T_r \simeq 0.8$ eV is the temperature of matter-radiation equality, $T_{ca} \simeq m_X/10$ is the X freeze-out temperature, g^*_{ca} is the number of relativistic field degrees of freedom at freeze-out, and M_{pl} is the reduced Planck mass. From this we see that in the regime in which consistent cosmological formation can be obtained for dark fermion masses up to and even exceeding 10^{10} GeV. The resulting number of dark matter particles contained per composite is well above the saturation threshold, Eq. (4.8), and leads to composite masses approximately ranging over 10^{10} - 10^{42} GeV, where even larger masses may be obtained for a smaller dilution parameter ζ. Thus, the binding field in the composite interior is $\langle\phi\rangle \propto m_X$, and potentially results in highly-energetic signatures, as initially explored in [108]. However, we will also show below that, even if the composites are comparatively less massive and $\langle\phi\rangle$ is correspondingly smaller (*i.e.* for $\zeta = 1$), a small coupling between ϕ and Standard Model nucleons can still result in detectable nuclear scattering and ionization processes at underground dark matter experiments [109].

4.1.3 Nuclear Acceleration Effect from Composite Potential

So far we have discussed the properties of saturated composite states without assuming any coupling of this dark sector to Standard Model particles. We now introduce a coupling between the binding field ϕ and SM nucleons by adding a Yukawa interaction,

$$\mathcal{L}_n = g_n \bar{n} \phi n \tag{4.12}$$

to Eq. (4.1), where g_n is the Yukawa coupling between ϕ and Standard Model nucleons. Note that g_n can be either positive or negative, resulting in either a repulsive or attractive Yukawa potential for nucleons sourced by the dark matter composite. As we saw above, the binding field $\phi(x) \simeq \langle\phi\rangle$ is classical and effectively uniform inside a large composite, and its value is well-approximated by

$$\langle\phi\rangle \simeq \frac{m_X}{g_X}, \quad r < R_X, \tag{4.13}$$

so long as $m_* \ll p_F$, *cf*. Eq. (4.3). On the other hand, because of boundary conditions, the field must rapidly decay outside the composite state according to,

$$\phi(r) = \langle\phi\rangle\; e^{-m_\phi(r-R_X)} \left(\frac{R_X}{r}\right), \quad r \geqslant R_X. \tag{4.14}$$

Nuclei coupled to this scalar ϕ will then have an effective mass smaller or larger than their vacuum mass in the composite interior, for an attractive and repulsive potential, respectively. Energy conservation imposes that their momenta must change as they enter the boundary of the composite state (and similarly as they exit) according to,

$$p^2 + m_N^2 = p'^2 + (m_N - \langle\varphi\rangle)^2\,, \tag{4.15}$$

where p and p' are the momenta of a nucleus before and after entering the composite respectively, $m_N = Am_n$ is the nuclear mass, and we have defined $\langle\varphi\rangle = Ag_n\langle\phi\rangle$. We note again that the above implies a decrease or increase in the mass of the nucleus, depending on the sign of g_n.

Before continuing, for completeness we summarize four interaction regimes for large dark matter composites with a Yukawa coupling to nuclei.

1. $\langle\varphi\rangle \lesssim m_N$ and $g_n > 0$. In this case there will be energetic interactions between nuclei accelerated into the composite interior. We have recently studied signatures of the resulting Bremsstrahlung and fusion processes in [108].

2. $\langle\varphi\rangle \ll m_N$ and either $g_n > 0$ or $g_n < 0$. Low energy attractive or repulsive interactions will result in a soft nuclear recoil at the boundary of the composite, yielding scintillation and Migdal ionization at underground experiments as we show for the first time in this work. Quite recently, repulsive dark matter composites were also studied in the context of mineralogical detection [296].

3. $\langle\varphi\rangle \gg m_N$ and either $g_n > 0$ or $g_n < 0$. For a large enough (and hence relativistic) attractive or repulsive composite potential, the dark matter composite boundary will form a repulsive barrier for incoming nuclei [303], as discussed in [108]. Most of the nuclear recoil work presented here will generalize easily to this case.

4. In addition to interactions between the dark matter composite's scalar potential

$\langle\varphi\rangle$ and nuclei, we also consider nucleus-X (that is nucleus-constituent) scattering interactions. These can occur as scattering interactions between nuclei and single dark matter constituents, or take the form of collective excitations of multiple composite constituents. As discussed in Sec. 4.1.4, these interactions are highly suppressed relative to interactions with the composite potential, since X constituent particles in saturated composites are highly degenerate.

Fig. 4.1 shows a schematic of the different recoil and high energy processes that arise from a Yukawa coupling between the binding field for composites (ϕ) and SM nucleons. In what follows we will focus on the case that g_n is positive and the potential is attractive. For the low-energy scattering processes we will study in Section 4.2.1, the generalization to g_n negative is straightforward, since the nuclear recoil spectrum implied for an attractive and repulsive potential are the same.

To quantify the kinetic energy change of nuclei at the boundary of the composite, we first note that the field $\langle\varphi\rangle$ couples directly to the nuclear mass since it is a Lorentz scalar. When $\langle\varphi\rangle \ll m_N$, we neglect the $\sim \mathcal{O}(\langle\varphi\rangle^2)$ term and obtain the kinetic energy change in the non-relativistic limit,

$$\Delta E \simeq \left(\frac{p'^2}{2m_N} - \frac{p^2}{2m_N}\right) \simeq A g_n \left(\frac{m_X}{g_X}\right). \tag{4.16}$$

In this limit, the kinetic energies of nuclei can lead to nuclear fusion and bremmstrahlung we investigated in [108]. Eq. (4.16) above illustrates the central result: the energy difference per SM nucleon is given by $g_n m_X/g_X$ for large composites, where the constituent mass m_X can span several orders of magnitude in straightforward cosmologies, ranging from sub-GeV up to EeV. Such heavy constituents are accommodated in a cosmology that includes a stage of relic abundance dilution [108], *cf.*

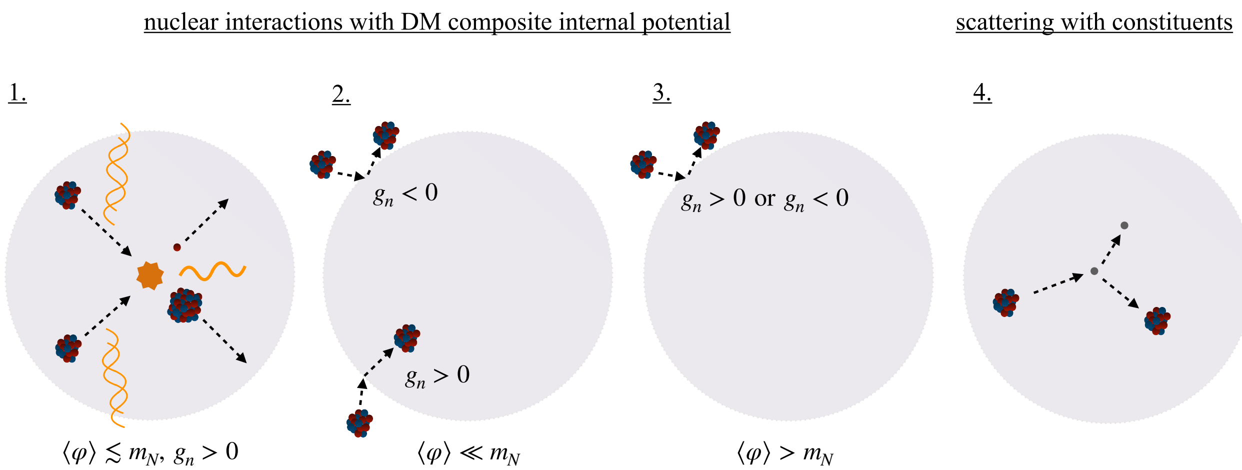

Figure 4.1: Different interactions are shown between a large dark matter composite and nuclei, for nucleons that have a Yukawa coupling g_n to the scalar field ϕ that binds the composite constituents X together. For the first three processes, the size of the Yukawa potential for nuclei inside the dark matter composite, $\langle\varphi\rangle = Ag_n\langle\phi\rangle$, as compared to the nuclear mass m_N, determines the characteristics of nuclear interactions with the composite's scalar potential. The sign of the Yukawa coupling g_n determines whether the potential is attractive or repulsive. *1.* The first panel shows that for a sizable, attractive, but non-relativistic Yukawa potential, nuclei emit Bremmstrahlung radiation and may fuse in the composite interior, as studied in [108]. *2.* The second panel shows that for a small composite potential $\langle\varphi\rangle \ll m_N$, nuclei will recoil at the boundary of the composite, either accelerating or decelerating, depending on whether the potential is attractive or repulsive. Note that in the case of a repulsive Yukawa potential, the extent to which the nucleus enters the composite will depend on its initial kinetic energy as compared to $\langle\varphi\rangle$. *3.* The third panel shows that for a relativistic internal potential, there will be a large potential barrier that reflects nuclei [108, 303]. *4.* The fourth panel depicts nuclear scattering with DM constituents X. As detailed in Section 4.1.4, this sort of scattering interaction will be very suppressed since the X particles in the composite are highly degenerate.

Eq. (4.11). Therefore, even for tiny coupling values, nuclei can gain or lose substantial kinetic energy as they cross the composite boundary. In addition, the composite states considered have large sizes compared to the atomic separation at densities $\rho_* \gtrsim 1$ g cm^{-3}, and so they collect a large number of nuclei in their interior. Thus, composites with this simple renormalizable coupling to SM nucleons act as microscopic nuclear accelerators as they traverse matter.

A number of processes can occur between nuclei and dark matter composites, depending on the Yukawa coupling g_n, as this quantity determines the dynamics of SM matter as it crosses the composite interior. For nuclear kinetic energy shifts $\Delta E \lesssim 100$ eV, a small fraction of the entering atoms will be ionized via collisional processes and the Migdal effect [304, 305], leading to the emission of electromagnetic radiation. In Section 4.2.1, we demonstrate that the Migdal effect alone permits liquid noble element experiments like XENON-1T to probe nucleon-scalar Yukawa couplings well below existing constraints based on stellar cooling arguments [109]. For $\Delta E \gtrsim 100$ eV, low-Z atomic nuclei will be fully ionized, leading to substantial thermal bremsstrahlung, and potentially thermonuclear reactions if the kinetic energy change of nuclei exceeds $\gtrsim 100$ keV [108]. However, as was previously indicated, these high energy signatures can only occur for heavy composites with masses beyond the reach of direct detection experiments. Nevertheless, these fusion-capable composite states could still be discovered at neutrino experiments through the massive energy released upon their transit, which is discussed in Sec. 4.2.2. Finally, in Section 4.3, we show how composites with this simple coupling to the Standard Model may trigger Type-Ia supernovae in white dwarfs [108, 109], as well as explore implications for planetary heating [109]. At much higher energies, the non-relativistic approximation made here for nuclei breaks down. This can be seen from Eq. (4.15): if $\langle\varphi\rangle \gtrsim m_N$, then necessarily $p' < p$, implying that this potential eventually becomes repulsive in this limit [303]. We have left a detailed treatment of this case to future work – however we would point out that there are bounds on such high values of $\langle\varphi\rangle$, because of stellar cooling limits considerations, which at present limit the coupling to values $g_n \lesssim 10^{-10}$ - 10^{-12} over the mediator mass range $m_\phi \sim$ eV - GeV.

To conclude this Section, we discuss the timescale over which nuclei are accelerated when entering the composite's Yukawa potential. As we show below, this timescale is short compared to the timescale over which the nucleus crosses the dark matter composite, since the composite radii considered here are much larger than the binding force range, and so nuclei are accelerated over a short distance to substantial energies. First, we consider the dynamical expression for the acceleration time

$$\tau_{\text{accel}} = \left(\frac{m_N}{2}\right)^{1/2} \int_{\infty}^{R_X} \left(\varepsilon + \varphi(r)\right)^{-1/2} \, dr, \tag{4.17}$$

where ε denotes the energy of the nucleus in the composite rest frame and $\varphi(r) = A g_n \phi(r)$, with $\phi(r)$ given by Eq. (4.14). The initial energy ε can be expressed in terms of the energy in the laboratory frame ε_0 via $\varepsilon = \varepsilon_0 + \mathbf{p}\cdot\mathbf{v}_X + m_N v_X^2/2$, with $\mathbf{v}_X$ being the velocity of the composite in such frame. For the phenomenology considered in this work, $\varepsilon_0 \ll m_N v_X^2/2$ and the initial (pre-composite crossing) energy of nuclei in the composite rest frame is well approximated by $\varepsilon \simeq m_N v_X^2/2$. Because the field gradient decays exponentially outside the composite volume, nuclei accelerate over a short distance near the composite surface. In terms of the dimensionless variable

$\chi = r/R_X$, this length scale is $\chi \simeq (m_\phi R_X)^{-1}$. The acceleration timescale is then

$$\tau_{\rm accel} = R_X \left(\frac{m_N}{2\varepsilon}\right)^{1/2} \int_{1+(m_\phi R_X)^{-1}}^{1} \left(1 + \left(\frac{\varphi}{\varepsilon}\right) \frac{e^{-m_\phi R_X(\chi-1)}}{\chi}\right)^{-1/2} d\chi, \qquad (4.18)$$

which can be solved numerically. However, for the large composite masses we consider, it is always the case that $(R_X m_\phi)^{-1} \ll 1$. Therefore, we can estimate the timescale above by approximating $\chi \simeq 1$ and $d\chi \simeq (m_\phi R_X)^{-1}$, yielding

$$\tau_{\rm accel} \simeq \frac{1}{m_\phi}\left(\frac{1}{v_X^2 + v_N^2}\right)^{1/2} \simeq 6.5 \times 10^{-19}\ \mathrm{s}\ \left(\frac{m_\phi}{\mathrm{MeV}}\right)^{-1} \left(\frac{v_X}{10^{-3}}\right)^{-1}, \qquad (4.19)$$

where $v_N = (2\langle\varphi\rangle/m_N)^{1/2}$ is the final nuclear velocity in the composite rest frame. In the rightmost expression, we show the scaling when $v_N \ll v_X$, which is the case for all phenomena considered in this work. Note that in the opposite limit $v_X \ll v_N$ a finite acceleration timescale is also recovered,

$$\tau_{\rm accel} \simeq m_\phi^{-1}\left(\frac{2\langle\varphi\rangle}{m_N}\right)^{-1/2} \simeq 10^{-18}\ \mathrm{s}\ \left(\frac{m_N}{10\ \mathrm{GeV}}\right)^{\frac{1}{2}} \left(\frac{m_\phi}{\mathrm{MeV}}\right)^{-1} \left(\frac{\langle\varphi\rangle}{\mathrm{MeV}}\right)^{-\frac{1}{2}}. \qquad (4.20)$$

Before turning to the associated signatures of this effect, next we discuss the potential scattering processes between nuclei and the dark matter.

4.1.4 Scattering Interactions between Nuclei and Composites

In this Section, we discuss a few different interactions between nuclei and dark matter constituents, *i.e.* processes that fall under the fourth category depicted in Fig. 4.1. These processes are of some interest, since if nuclei lose kinetic energy while scattering in the composite, this will cause a kinetic drag on the composite state, resulting in a stopping force as the composite moves through matter, for further details see App. B. A full treatment of every scattering interaction is out of scope: it would require the computation of a dynamic structure factor $S_X(\mathbf{q}, \omega)$, which has encoded all the collective excitations of the constituents, for a given momentum exchange $\mathbf{q}$ and energy exchange ω between the nucleus and the composite state. This is still an active area of investigation. Instead, following [109], we briefly review the three lowest-lying scattering modes: coherent scattering of the nucleus against the full composite state, excitation of low-lying surface modes, and up-scattering individual constituents above the Fermi level in an ideal Fermi gas approximation. Below, we briefly comment on each process, while the full details can be found in [109],

- *Coherent composite-nucleus scattering:* We first consider the scattering process whereby a composite with N_X constituents and radius R_X coherently scatters against a nucleus and transfers a fraction of its total momentum and kinetic energy. As computed in [109], in terms of the momentum exchange q, the differential cross section for this process is given by,

$$\left(\frac{d\sigma}{dq}\right)_{XN\to XN} = A^2 N_X^2 f^2(\Lambda)\bar{\sigma}_0 \left(\frac{q}{2m_N^2 v_X^2}\right) \, |F_X(qR_X)|^2 \, |F_a(qr_N)|^2, \quad (4.21)$$

  where A is the mass number of the nucleus, v_X is the velocity of the nucleus in the composite rest frame, and $\bar{\sigma}_0 = g_n^2 g_X^2 m_N^2/4\pi\tilde{m}_\phi^4$ is a reference cross section for point-like dark matter scattering against a free nucleus in the limit $m_N \ll M_X$. This reference cross-section includes the mediator mass correction due to screening effects, $\tilde{m}_\phi^2 = m_\phi^2 + \delta m_\phi^2$ with $\delta m_\phi^2 \simeq (4\pi\alpha_X \bar{m}_X^4)^{1/2}$. The function

$f(\Lambda)$,

$$f(\Lambda) = \min\left[1, \left(\frac{\Lambda}{R_X}\right)^3\right], \tag{4.22}$$

accounts for the partial overlap of the nucleus wave function with the composite state [276], Λ being the initial spatial spread of the scatterer wavefunction. This scale depends on the material in question, but relevant choices for this study are the thermal de Broglie wavelength in the case of terrestrial detectors, $\Lambda_{\rm th} = (2\pi/m_N T)^{1/2} \lesssim 10^{-9}$ cm, and the spatial dispersion of nuclei in the case of crystalline white dwarfs (*cf.* Sec. 4.3.1), $\Lambda_{\rm wd} = (2m_N\Omega_p)^{-1/2} \lesssim 10^{-12}$ cm with Ω_p being the plasma frequency. Eq. (4.22) effectively reduces the number of targets available for coherent scattering when the composite size is large compared to the initial spatial spread of the scattered nucleus. The two form factors in Eq. (4.21) are

$$F_a(qr_N) = \frac{3j_1(qr_N)}{qr_N} e^{-q^2 r_N^2}, \tag{4.23}$$

$$F_X(qR_X) = \frac{3j_1(qR_X)}{qR_X}, \tag{4.24}$$

and account, respectively, for the nuclear and composite substructure effects at inverse momentum exchanges that are small compared to the nucleus and composite radius. Overall, this cross section is highly suppressed for large composite states from the combined effect of the form factors above, existing limits on the coupling g_n, and Eq. (4.22).

- *Surface mode excitation:* Surface vibrations are potentially the lowest-lying collective modes in the composite state, with excitation energies of order $\sim$ eV in most of the parameter space [109]. The differential cross section for exciting a single surface vibration quantum (phonon) of angular momentum l can similarly be written as

$$\left(\frac{d\sigma}{dq}\right)_{0\to 1_l} \simeq A^2 N_X^2 f^2(\Lambda)\bar{\sigma}_0 \left(\frac{q}{2m_N^2 v_X^2}\right) |F_{\rm surf}^{(l)}(qR_X)|^2, \tag{4.25}$$

where most of the definitions are the same as in the previous item, see [109] for further details. The new form factor associated with single phonon excitation is

$$F_{\rm surf}^{(l)}(qR_X) = \epsilon_l \ (2l+1)^{1/2} j_l(qR_X). \tag{4.26}$$

The quantity ϵ_l above is the amplitude of the mode, which scales as,

$$\epsilon_l \propto m_X^{-1/4} \bar{m}_X^{-3/2} R_X^{-7/4} \simeq 10^{-14} \ \left(\frac{m_X}{\rm TeV}\right)^{-\frac{1}{4}} \left(\frac{\bar{m}_X}{5 \ \rm GeV}\right)^{-\frac{3}{2}} \left(\frac{R_X}{\rm nm}\right)^{-\frac{7}{4}}. \tag{4.27}$$

This form factor significantly reduces the cross section for exciting surface modes in the composite state. Moreover, the creation of multiple vibration quanta in a given mode l result in additional powers of ϵ_l, and therefore further suppression of the cross section. In a similar manner, we expect other collective modes to be suppressed from the same considerations above, as well as potentially having higher excitation gaps.

- *Constituent up-scattering:* In addition to quasi-coherent composite-nucleus scattering, accelerated nuclei in the interior of the composite may lose energy by exciting individual dark matter constituents above their Fermi level. We consider the dark matter constituents to form a non-interacting Fermi gas of particles with effective mass m_*, with $m_* \ll p_F$, when the composite state is sufficiently massive, *cf*. Eqs. (4.3) and (4.4). Since the dark matter constituents are ultra-relativistic, this scattering interaction requires a fully relativistic treatment, and the phase space available for scattering, given the degeneracy of the targets, must be carefully analyzed as well. In [170, 306], a Lorentz-invariant formalism was developed to compute the dark matter capture efficiency of relativistic degenerate electrons in neutron stars. Such formalism accounts for both relativistic kinematics and Pauli blocking of the targets. In [109], we have adapted those results to estimate the scattering rate and the subsequent energy loss of nuclei inside the composite from exciting constituents above the Fermi level. The scattering rate of a nucleus against dark matter constituents in the composite rest frame [306],

$$\Gamma_{NX\to NX^*} = n_X \int_{p_{\min}}^{p_F} \frac{dp\, p^2}{V_F} \int d\varphi\, d(\cos\theta) \times \int d\alpha\, d(\cos\psi)\, \Theta\left(\Delta E + p - p_F\right)\, \tilde{v} \left(\frac{d\sigma}{d\Omega}\right)_{(CM)}, \tag{4.28}$$

where $V_F = 4\pi p_F^3/3$ is the occupied phase space volume of the target dark matter particles, $n_X = p_F^3/3\pi^2$ is the dark matter number density, $(d\sigma/d\Omega)_{(CM)}$ is the tree-level constituent-nucleus differential cross section for a Yukawa interaction in the centre-of-momentum frame, and

$$\tilde{v} = \left(\frac{(p_\mu k^\mu)^2 - m_*^2 m_N^2}{(p^2 + m_*^2)(m_N^2 + k^2)}\right)^{1/2} \tag{4.29}$$

is the Moller velocity [307, 308], with p^μ and k^μ respectively being the four-momentum of the dark matter particle and the nucleus in the composite rest frame, prior to the collision. The latter is determined from Eq. (4.16). The Moller velocity relates differential cross sections in different frames for non-collinear scattering processes. In this case, the frames considered are the composite rest frame, where the Fermi surface is spherical, and the centre-of-momentum frame, where the collision kinematics are more easily analyzed. The scattering rate given by Eq. (4.28) integrates over the target Fermi sphere, and accounts for the potentially large boost between both frames for relativistic targets. The first two integrals correspond to integrating the differential cross section over the azimuthal and polar scattering angles (α, ψ) in the center-of-momentum frame. The integrals that follow correspond to integrating over the azimuthal and polar angles (φ, θ) on the Fermi sphere (the integral over φ yields a 2π factor). These angles determine the momentum direction of the dark matter targets in the composite rest frame. The final integral to the left corresponds to integrating over the momentum magnitude p of the dark matter constituents, also in the composite rest frame. Note that it runs from some $p = p_{\mathrm{min}}$ set by the Pauli blocking condition, *i.e.* only those dark matter particles occupying states sufficiently close to the Fermi surface will be excited. This condition is enforced by the Heaviside step function, where ΔE is the energy deposited by the nucleus in the composite frame. This energy transfer is fully determined by the relativistic kinematics, and in turn depends on the above angles, see [109] for details.

Integration of Eq. (4.28), in the limit that nuclei are non-relativistic, yields a scattering rate of order

$$\Gamma_{NX\to NX^*} \simeq \frac{3A^2 g_n^2 g_X^2 m_N^4 (m_N + 2p_F) v_N^6}{40\pi p_F^4}. \tag{4.30}$$

This scattering rate scales as $\mathcal{O}(v_N^6)$ at the lowest order in the nuclear velocity, with $v_N \lesssim 10^{-2}$ for the most energetic signatures of this model. Combined with existing limits on g_n and the large Fermi momentum of the constituents, the up-scattering rate of constituents by incoming nuclei is extremely small in all the parameter space considered.

Overall, we have found all of these processes to be extremely suppressed, and therefore, do not constitute a significant energy loss for nuclei as they accelerate due to the composite's internal field. Here, we have limited ourselves to review the basic features of each interaction, however, further details on the computation of the associated stopping power can be found in Ref. [109].

4.2 Signatures at Underground Experiments

Having reviewed the composite state properties in saturation, how these dark matter bound states may have been synthesized in the early universe, and their interactions with Standard Model nuclei, we now turn to discuss some of the signatures of this model at underground experiments.

4.2.1 Ionization via Migdal Effect at Liquid Noble Element Experiments

Composite dark matter crossing the volume of direct detection experiments can accelerate atomic nuclei over a short timescale, thereby ionizing and exciting atoms with the sudden nuclear recoil induced by the dark matter composite's potential. We first turn to the ionization of atoms at the dark matter composite boundary. The non-adiabatic response of electrons to an impulsive nuclear motion is called the Migdal effect [304, 305]. In essence, the Migdal formalism relies on a sufficiently rapid change in nuclear momentum, so that the perturbed electron wavefunctions can be modeled by applying a straightforward momentum boost. Therefore, to apply the Migdal formalism to large dark matter composites we will require that the nuclear recoil interaction time is short compared to both the electron orbital period $\tau_{e^-} \sim (10 \text{ eV})^{-1} \simeq 6.5 \times 10^{-17}$ s and the ratio R_a/v_N, where R_a is the atomic radius and v_N is the final nuclear velocity. Before the interaction the atomic nucleus can be assumed stationary, and the electron cloud is characterized by its ground state wavefunction $|\psi\rangle$. After the interaction has occurred, the nucleus moves with speed v_N. In the rest frame of the recoiling nucleus, if the interaction occurred fast enough, the electrons initially have the same coordinates as when the nucleus was stationary, but their momenta are boosted by $q = m_e v_N$. The perturbed electron cloud wavefunction is subsequently expressed as $|\psi'\rangle \simeq \exp\left(-i \sum_a \mathbf{q} \cdot \mathbf{r}_a\right) |\psi\rangle$, where r_a are the position operators of the electrons in this new rest frame, with $a = 1, ..., Z$. This yields a finite transition amplitude to excited and free states, even for the electrons occupying inner orbitals.

In practice, noble elements used in direct dark matter searches have large atomic radii of order $R_a \simeq 10^{-8}$ cm, so $R_a/v_N \gg \tau_{e^-}$. Comparing then the electron orbital period to Eq. (4.19), we see that the acceleration occurs fast enough for this approximation to be valid, so long as the composite is moving sufficiently fast or the potential is sufficiently short-ranged. In this Section, we will demonstrate that Migdal electrons produced by the composite transit yield excellent detection prospects for liquid noble element (LNE) experiments like XENON-1T.

There have been several proposals for dark matter searches using the Migdal effect [309, 310, 311, 312, 313, 314, 315, 316, 317, 318, 319, 320, 321, 322], especially in the sub-GeV mass range. As a proof-of-concept for dark matter composite detection, we will focus here on XENON-1T and its first dark matter search [23]. As we show below, the extremely low electron background of this experiment, combined with the high mass number of xenon, allows for a sensitivity to dark matter composite-nucleon couplings well below existing constraints. In particular, we follow here the analysis of [314]. However, because of the nature of the Migdal effect as applied to dark matter composites, the recoil energy spectrum will be different compared to [314], since all atomic nuclei are accelerated to approximately the same kinetic energy along the composite's path.

For a large dark matter composite, the Migdal ionization differential event rate per unit of exposure is set by

$$\frac{dR}{dE_R} = \frac{\rho_X}{m_N M_X} \int_{v > v_X^{(\min)}} \frac{d\sigma}{dE_R}\ v\ g(v)\ dv \tag{4.31}$$

where $m_N \simeq 130$ GeV is the mass of a xenon atom, and $g(v)$ is the dark matter velocity distribution in the laboratory frame. In our analysis we assume a local dark matter density $\rho_X \simeq 0.4$ GeV cm^{-3} [323] and use a flux-normalized velocity distribution outlined in [69],

$$f(\mathbf{v}) = \mathcal{N}^{-1}(v^2 - v_e^2)^{3/2} \exp\left(\frac{\tilde{v}^2}{v_0^2}\right) \Theta(v - v_e)\Theta(v_{eg} - \tilde{v}), \tag{4.32}$$

where $v = |\mathbf{v}|$, $v_e \simeq 11.2$ km s^{-1} is the Earth's escape velocity, $v_{eg} \simeq 528$ km s^{-1} is the galactic escape velocity, and $v_0 \simeq 220$ km s^{-1} is the velocity dispersion [324, 207]. The variable $\tilde{v}^2 = v^2 - v_e^2 + v_{rf}^2 + 2v_{rf}\sqrt{v^2 - v_e^2}\cos\varphi$ accounts for the relative velocity between the solar system with respect to the galactic frame, with $v_{rf} \simeq 230$ km s^{-1} and φ being the angle between such relative velocity and the dark matter vector. The constant $\mathcal{N}^{-1}$ is a normalization factor that enforces $\int_0^\infty \int_0^\pi f(\mathbf{v})\, dv\, d(\cos\varphi) = 1$. The distribution $g(v)$ in Eq. (4.31) is then given by the integration over φ of Eq. (4.32), *i.e.* $g(v) = \int_0^\pi f(\mathbf{v}) d(\cos\varphi)$.

We express the differential cross section per unit of nuclear recoil energy as the geometric cross section of the composite, multiplied by a delta function enforcing the fact that all nuclei along the composite path will be accelerated to the same energy

$$\frac{d\sigma}{dE_R} \simeq 2\pi R_X^2\ \delta\big(E_R - E_R^0\big)\,, \tag{4.33}$$

where $E_R^0 = A g_n m_X / g_X$ ($A \simeq 130$) denotes the kinetic energy to which nuclei are accelerated as they cross the composite boundary, *cf.* Eq. (4.16). Note that there is a factor of two in this expression that accounts for nuclei accelerating both as they approach and exit the composite boundary.

The minimum integration speed in Eq. (4.31), unlike other analyses, is now set by the minimum kinetic energy that the composite must have to penetrate the experiment's overburden, and still reach the detection volume with a sufficient speed for the Migdal approximation to remain valid. Depending on the coupling and mediator mass, radiation or conduction losses will dominate the stopping power. For couplings sufficiently high so that temperatures $T \gtrsim 100$ eV are reached in the composite interior, matter will be completely ionized but optically thin to photons, resulting in an energy loss in the form of thermal bremsstrahlung, see below. At smaller couplings, however, heat conduction losses will dominate, which we estimate by taking a crust thermal conductivity ~ 1 W m^{-1} K^{-1} $\simeq 10^7$ GeV s^{-1} [325] and applying Fourier's law with a thermal gradient $\nabla T \simeq T m_\phi$. Both of these energy loss channels imply that composites must have a minimum velocity of order $v_X^{(\text{heat})} \gtrsim 10^{-4}$ - 10^{-3}, and so an $\sim \mathcal{O}(1)$ fraction of the flux will have enough kinetic energy to penetrate the overburden. On the other hand, for the Migdal approach to be valid, we require the acceleration timescale τ_{accel}, given by Eq. (4.17), to be short enough compared to the electron orbital period, of order $\tau_{e^-} \sim 10^{-17}$ s. Thus, setting $\tau_{\text{accel}} = \tau_{e^-}$ in Eq. (4.17), we obtain the minimum speed

$$v_X^{(\text{mig})} \simeq \frac{1}{m_\phi \tau_{e^-}} \simeq 10^{-5} \left(\frac{\text{MeV}}{m_\phi} \right), \tag{4.34}$$

where we have neglected v_N in Eq. (4.17) compared to $(m_\phi \tau_{e^-})^{-1}$, which is the case for the entire parameter space considered here.

The differential ionization rate will be given by Eq. (4.31), multiplied by the probability of electron emission from a given energy level [314],

$$\frac{dR_{\text{ion}}}{dE_R dE_e} = \frac{dR}{dE_R} \times \left(\frac{1}{2\pi} \sum_{n,l} \frac{dp_{n,l\to E_e}}{dE_e} \bigg|_q \right). \tag{4.35}$$

in the above equation, E_e is the final kinetic energy of the ionized electron and $\frac{dp_{n,l\to E_e}}{dE_e}|_q$ is the differential probability, for a given momentum change $q = m_e v_N = (2m_e^2 E_R^0/m_N)^{1/2}$, for an electron initially at a level (n,l) to be ionized with a final kinetic energy E_e. This set of probabilities was numerically computed for xenon atoms in [313]; we use the results of that study to evaluate the integral in Eq. 4.35 (Table

II of [313]). The total energy deposition is given by $E_{em} = E_{nl} + E_e$, where E_{nl} is the initial binding energy of the electron. We remark that while E_e is typically $\sim \mathcal{O}(\text{eV})$, the ionization energies E_{nl} are $\sim \mathcal{O}(\text{keV})$, and therefore dominant.

Due to the very narrow nuclear recoil spectrum, *cf.* Eq. (4.33), integration over the nuclear recoil energy can be performed analytically. We can also integrate over the electronic energies and obtain

$$R_{\text{ion}} = \frac{4\pi R_X^2 n_X}{m_N} \times \left(\int_{v > v_X^{(\text{min})}} v \; g(v) \; dv \right) \times \left(\frac{1}{2\pi} \sum_{n,l} \int dE_e \; \varepsilon(E_{em}) \; \frac{dp_{n,l\to E_e}}{dE_e} \bigg|_q \right). \tag{4.36}$$

We have explicitly included here XENON-1T's detection efficiency for a given electromagnetic energy deposition $\varepsilon(E_{em})$ [314]. For XENON-1T's first run, a total exposure of 98 kg yr was achieved [23]. Furthermore, the integral in the above equation yields a factor of q^2, allowing us to express the total number of Migdal electron events at XENON-1T in terms of composite parameters, *cf.* Eqs. (4.6) and (4.16),

$$N_{\text{ion}} \simeq 10^8 \left(\frac{m_X}{10^3 \text{ GeV}} \right)^{-\frac{2}{5}} \left(\frac{m_\phi}{10^{-3} \text{ GeV}} \right)^{-\frac{4}{5}} \left(\frac{g_n}{10^{-10}} \right) \left(\frac{\alpha_X}{0.3} \right)^{-\frac{1}{10}} . \tag{4.37}$$

It is also relevant to compute the average number of electronic recoils produced by a single composite transiting the detection volume. This is given by the ionization probabilities, the detection efficiency, and the flux of xenon atoms through the composite,

$$\begin{aligned} N_{\text{transit}} &\simeq \left(2\pi R_X^2 n_{\text{Xe}} L_{\text{det}} \right) \times \left(\frac{1}{2\pi} \sum_{n,l} \int dE_e \; \varepsilon(E_{em}) \; \frac{dp_{n,l\to E_e}}{dE_e} \bigg|_q \right) \\ &\simeq 5 \times 10^{16} \left(\frac{R_X}{\text{nm}} \right)^2 \left(\frac{m_X}{\text{TeV}} \right) \left(\frac{g_n}{10^{-10}} \right) \left(\frac{\alpha_X}{0.3} \right)^{-\frac{1}{2}} . \end{aligned} \tag{4.38}$$

In the above expression, $L_{\rm det} \simeq 100$ cm is the length scale of XENON-1T's detection volume, $n_{\rm Xe} \simeq 10^{22}$ cm^{-3} is the number density of targets, and we assume the composite is moving fast enough for the Migdal approximation to be valid. Eq. (4.38) demonstrates that even for tiny couplings, a composite crossing XENON-1T's volume could be observed from the large ionization track it creates.

Finally, we must consider the maximum composite mass that can be probed by XENON-1T given the total dark matter flux passing through the experiment. An accurate modelling of the experiment's geometry is out of the scope of this work (see, *e.g.*, [326, 327, 328, 329, 295]), however as a first estimate we use the flux through a spherical detector with a radius of order $R_{\rm det} \sim 50$ cm, yielding $\Phi_X \simeq 2\pi R_{\rm det}^2 \langle v_X \rangle (\rho_X / M_X) \simeq 10^{-4}\ {\rm s}^{-1} \left(M_X / 10^{15}\ {\rm GeV}\right)^{-1}$. The maximum mass to which the experiment is sensitive is then estimated by requiring $\Phi_X t \simeq 1$, where t is the running time. XENON-1T's first dark matter search had a total of 34.2 live days [23], resulting in a mass limit of $M_X^{(\rm max)} \simeq 2 \times 10^{17}$ GeV.

Figure 4.2 shows the constraints on the dark matter-nucleon coupling g_n based on XENON-1T's first dark matter search results, for composites with different mediator masses that were synthesized in the early universe without a dilution stage, *cf.* Eq. (4.11) with $\zeta = 1$. A composite synthesis including a dilution stage $\zeta \ll 1$ results in much heavier composites, limiting their detection prospects at traditional dark matter experiments due to the flux limit set by their running time and size (however, large neutrino observatories can still play a role in their detection, see [108]). The bounds in Fig. 4.2 are derived from the observation of $\mathcal{O}(1)$ electron recoil events during XENON-1T's first run. The composite mass range is limited either by the strong binding condition, $\bar{m}_X \ll m_X$, or the minimum composite radius considered here.

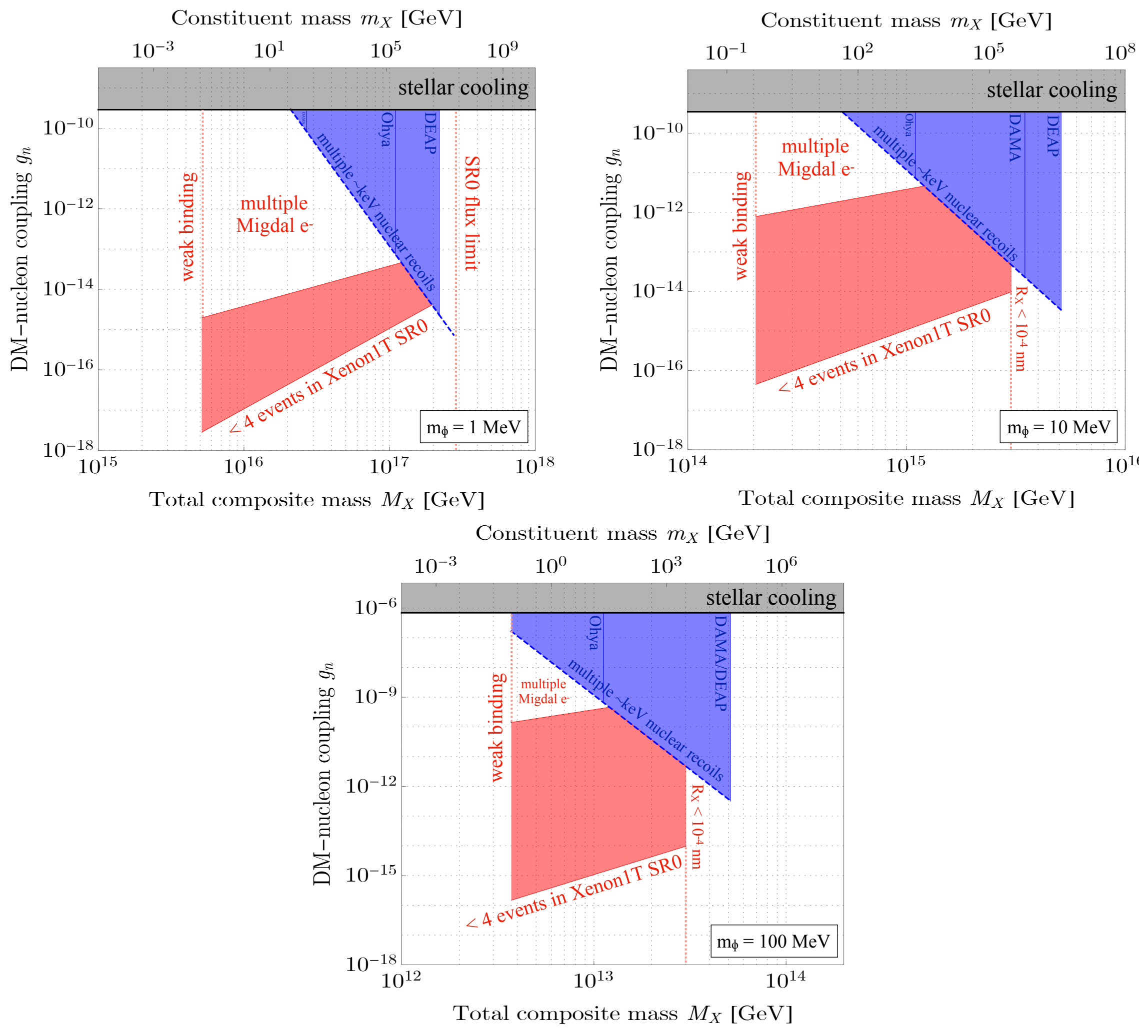

Figure 4.2: Bounds on the dark matter-nucleon coupling from XENON-1T's first dark matter search (SR0) [23] as a function of composite mass (**red**), for a fixed dark coupling $\alpha_X = 0.3$, and different binding mediator masses. The upper horizontal scale indicates the corresponding constituent mass. These results assume no dilution during cosmological synthesis, *cf*. Eq. (4.11). Constraints are drawn from the expected number of Migdal electrons from composites in 98 kg yr of exposure, compared to the electronic recoils observed. We require $R_X > 10^{-4}$ nm so that each composite intercepts a few xenon nuclei. At small M_X, the strong binding condition is not met. The line 'SR0 flux limit' indicates the maximum mass reach of XENON-1T's SR0. Above the upper line, a single composite will produce multiple Migdal electrons, requiring a new analysis of XENON-1T data. The dashed blue line shows where each composite produces multiple $\sim$ keV nuclear recoils, constrained by DAMA [330], DEAP-3600 [27] and Ohya quarry/Skylab [329] (**blue**). We also show stellar cooling bounds on light scalar fields coupled to nucleons [331, 332] (**gray**).

The upper bound of the constraints is set by Eq. (4.38). For larger couplings, a single composite would create an ionization track while transiting the detection volume. While clearly detectable, such a signal requires a dedicated analysis of XENON-1T's data, which is out of the scope of this work.

For comparison, we have also indicated the parameter space region where observable $\sim$ keV nuclear recoils proceed. Within this region, we display existing constraints from DAMA [330], a recent analysis of multiscatter signatures of superheavy dark matter at the DEAP-3600 experiment [27], and the Ohya quarry [333, 329], which are obtained by identifying the geometric cross section of the composite with a cross section for scattering with nuclei. Specifically, we use Eq. (4.6) with Eq. (4.11) and the definition of $\bar{m}_X$ in the saturated regime to obtain the geometric cross-section for the composites, which is directly constrained by geometric composite nuclear scattering as detailed in [329]. We note that there is a nontrivial relationship between the radius of the assembled composite and m_X; the scaling follows $R_X \propto m_X^{-3/5}$, meaning more massive composites with more massive constituents will be smaller in size. For this work, we have terminated the bounds at a cutoff radius $R_X \simeq 10^{-4}$ nm, to ensure that each composite encounters at least one xenon nucleus during its transit through XENON-1T's detection volume. Smaller composite geometric cross-sections can in principle be considered, but we have left a detailed treatment of this regime for future investigation. Additional bounds using nuclear scattering should be obtainable with new multiscatter analyses at experiments like XENON-1T [326, 327, 334, 328], as were recently obtained by DEAP-3600 [27]. We also show existing stellar cooling constraints on the coupling [331, 332]. Overall, these plots demonstrate that couplings well below existing experimental or stellar cooling constraints can be probed for large composite states by accounting for the Migdal effect. We also remark that for the regions we have constrained, the bounds are equally valid for a repulsive interaction between nuclei and the composite state, since the Migdal effect is independent of the direction of the momentum change.

Finally, we comment on other existing constraints on nucleon couplings to light scalars from cosmological and experimental origin. As discussed extensively in [332], the light scalar ϕ may contribute to the number of relativistic degrees of freedom at Big Bang Nucleosynthesis. However, for couplings $g_n \lesssim 10^{-9}$, its resulting contribution is not in tension with limits on $\Delta N_{\rm eff}^{\rm BBN}$ measured from primordial H and D abundances, as well as similar limits from CMB data and large-scale structure. In addition, one might consider whether the composite states themselves alter cosmological predictions like BBN; however cosmological observables appear to be unaltered by these composites, primarily because of their low number density [108]. There are also constraints on g_n from accelerators. At present, rare B and K meson decays place limits of order $g_n \lesssim 10^{-8}$ [332], which are less restrictive than the stellar cooling constraints we account for.

4.2.2 Bremsstrahlung and Nuclear Fusion at Neutrino Observatories

In the previous Section, we have shown that for tiny couplings these composite states could be detected from the order ∼few ionization events they produce at dark matter direct detection experiments over time. At larger dark matter-nucleon coupling g_n, more energetic signatures occur during the transit of composite dark matter through a given medium. As shown in [108], for potential values $\langle \varphi \rangle \gtrsim 100$ eV, the composite transit produces copious amounts of thermal radiation and potentially nuclear processes that vastly exceed the detection threshold of any terrestrial dark matter search. This is schematically shown in Fig. 4.3. However, since $\langle\varphi\rangle \propto g_n m_X$, and g_n is severely constrained from stellar cooling arguments, the constituents must be rather heavy to get such high energy signatures with such small couplings. This, in turn, requires large dilution factors ($\zeta \ll 1$) in the early universe, and the synthesized composites are so heavy that they are challenging to observe with direct detection experiments given their overall flux limit. Indeed, thermal radiation can only occur for transplanckian composite states, whereas experiments like XENON-1T or DEAP-3600 have lower mass limits, *cf.* Fig. 4.2. Instead, as pointed out in [108], one could consider neutrino observatories, such as IceCube and SNO+, with much larger geometric sizes and therefore much larger flux limits. Moreover, their high trigger thresholds compared to typical dark matter experiments are not an impediment for detection, as they are also significantly exceeded during the transit of composite states. In this Section, we analyze these higher energy signatures, and discuss composite detection prospects at neutrino experiments.

First, we discuss the ionization state of matter as it crosses the composite boundary. As shown previously, the sharp gradient of the composite potential accelerates atomic nuclei to high energies in a rather short timescale. For lighter elements like carbon or oxygen, the most abundant elements in *e.g.* IceCube and SNO+, numerical results from [313] indicate that the probability of outer-shell electron ionization for these atoms is of order $f_e \simeq (10^{-2}$ - $10^{-1})$, for the nuclear kinetic energies considered here, with the probability peak located at ionized electron energies $\sim$ 1 - 10 eV. Hence after this impulsive motion, a sizeable fraction of atoms are already partially ionized. However, further considerations indicate the atoms will be fully

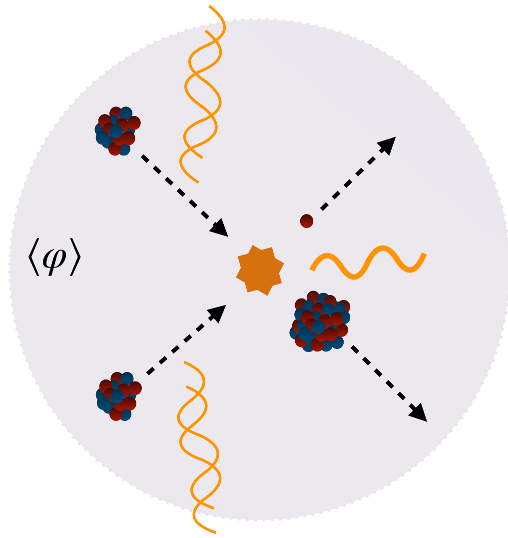

Figure 4.3: Schematic of nuclei accelerated by the potential $\langle\phi\rangle$ inside a dark matter composite. Depending on the coupling strength g_n, this effect results in ionization, bremsstrahlung radiation, and thermonuclear fusion. In the above graphic, a typical fusion reaction is displayed where two oxygen combine to make phosphorous, a proton, and ~ 7.7 MeV excess energy.

ionized. The atoms accelerated to relative energies 100 eV - 1 MeV, will scatter with the free electrons, resulting in further ionization. The cross-section for ionizing atomic oxygen or carbon is $\sigma_i \sim (10^{-17}$ - $10^{-16})$ cm^2 in the energy range of interest [335]. Ionization by electron-atom collisions will occur on a timescale given by $(f_e n_e v_N \sigma_i)^{-1} \lesssim 10^{-15}$ s, where v_N is the atom velocity and $n_e \simeq 10^{23}$ cm^{-3} is the typical electron number density. This timescale is shorter than the composite crossing time $(2R_X/v_X) \gtrsim 10^{-15}$ s $(R_X/\text{nm})(v_X/10^{-3})^{-1}$, so long as composites are larger than $\sim$nanometer, and becomes even shorter as more electrons are ionized and f_e tends to unity. Hence, we expect atoms to be fully ionized when composites are sufficiently large. This occurs in the detection regions shown in Fig. 4.4. Furthermore, our estimates are in agreement with Ref. [336], which finds order one ionization fractions for carbon and oxygen plasmas at $T \gtrsim 100$ eV and density ~ 1 g cm^{-3}.

The resulting ion-electron plasma that forms in the composite interior will have a photon opacity dominated by free-electron scattering, with a photon mean free path $(n_e \sigma_T)^{-1} \simeq 5$ cm $\gg R_X$, where $\sigma_T \sim 10^{-24}$ cm^2 is the non-relativistic Thompson cross-section for electrons. Therefore, radiation never equilibrates with the plasma and we do not expect blackbody radiation. Instead, we expect thermal electron-ion bremsstrahlung, which has specific emissivity at frequency ω (see *e.g.* [337])

$$j_\omega = \left(\frac{16\pi e^6 n_e^2}{3\sqrt{3} m_e^2}\right)\left(\frac{2m_e}{\pi T}\right)^{1/2} \exp\left(-\frac{\omega}{T}\right), \tag{4.39}$$

for electron mass m_e and fine structure constant $e^2/4\pi$. Since in Fig. 4.4 we require $T \gtrsim 100$ eV, there is emission of ionizing radiation. The integrated emissivity over volume and frequency yields a radiated energy rate

$$\begin{aligned} \dot{E}_{\text{brem}} &= \frac{64\pi^2 e^6}{9\sqrt{3} m_e^2}\left(\frac{2m_e T}{\pi}\right)^{\frac{1}{2}} n_e^2 R_X^3 \\ &\simeq 10^{10} \text{ GeV s}^{-1} \left(\frac{g_X}{1}\right)^{-\frac{1}{2}} \left(\frac{g_n}{10^{-10}}\right)^{\frac{1}{2}} \left(\frac{m_X}{\text{TeV}}\right)^{\frac{1}{2}} \left(\frac{R_X}{\text{nm}}\right)^3 . \end{aligned} \tag{4.40}$$

At temperatures $T \sim 100$ keV - 1 MeV, we also expect a fraction of the ions to undergo thermonuclear fusion. In particular, we consider ^{16}O burning reactions, with their rate tabulated in [338], for two reasons: first, it is the most abundant isotope in the terrestrial crust and mantle, which is relevant for planetary heating considerations discussed in Sec. 4.3.2. Second, as we detail below, they are the reactions that could potentially proceed within IceCube's volume.

Inspecting Eq. (4.40), it is clear that the radiation alone produced by large and heavy composite states makes them observable at large neutrino experiments like IceCube, Super-K, as well as large volume scintillators (LVS) like SNO+, Borexino, and JUNO; their enormity extends the M_X mass reach to 3×10^{25} GeV in the case of IceCube (assuming 5 yrs and a km^2 detection area). Before establishing the sensitivity prospects of these underground experiments though, we briefly comment on the possibility of composites being halted in the experiment's overburden. The same radiative losses described above could in principle halt the composite state before it reaches the detectors, see App. B for a general discussion on composite stopping. Other energy losses, such as heat conduction or ionization play a lesser role in this higher energy regime. Using Eq. (4.40), we find a composite with an initial velocity v_X will travel through the Earth's mantle a distance

$$L_{\rm cap} \simeq 2~{\rm km}~\left(\frac{m_X}{\rm TeV}\right)^{3/2}\left(\frac{g_n}{10^{-10}}\right)^{-1/2}\left(\frac{g_X}{1}\right)^{-3/2}\left(\frac{v_X}{200~{\rm km~s^{-1}}}\right)^{3}\left(\frac{m_\phi}{10~{\rm keV}}\right)^{2}, \quad (4.41)$$

before being slowed below Earth's escape velocity, where we have computed this distance considering the most abundant isotope ^{16}O and using elemental/density profiles from [339, 69]. Eq. (4.41) indicates that the underground experiment's overburden does not prevent the composites from reaching the detection volume for overhead trajectories. Furthermore, it demonstrates that astrophysical objects like the Earth are highly efficient at capturing these composite states in their interior, a subject that is further analyzed in Sec. 4.3.2. We remark that the scalings of the above equation agree with a more simple capture estimate $L_{\rm cap} \sim \Delta E_{\rm cap} v_\chi / \dot{E}_{\rm brem}$, where $\Delta E_{\rm cap}$ is the dark matter's initial kinetic energy. The Earth's composite capture rate can be subsequently found using, for instance, the method described in [69].

To conservatively establish the sensitivity of IceCube and LVS to a flood of $\gtrsim$ eV photons emitted from transiting composites, we require trigger threshold energy depositions of ~ 10 TeV and 1 MeV per 100 ns respectively, which are an order of magnitude above the TeV [340] and 100 keV [341, 342] per 100 ns design thresholds of these experiments (this still underestimates IceCube's sensitivity, since our requirement implies $\gtrsim$ 100 PeV radiated in a transit through IceCube). Comparing this to Eq. (4.40), we find that nucleon couplings as small as $g_n \sim 10^{-14}$ at IceCube and $g_n \sim 10^{-12}$ at LVS can be detected in the upper left portions of IceCube and LVS detection regions marked in Fig. 4.4. Smaller coupling values will result in too little radiation rate for composite detection. We also show where highly exothermic ^{16}O fusion reactions occur at IceCube as a single composite crosses its volume, using the ^{16}O burning rate tabulated in [338] as a function of temperature, and requiring at least one reaction to occur during the composite's transit through IceCube's volume. In this case, there will be additional gamma rays and byproducts with $\sim$MeV energies, *e.g.* ^{32,31}S, ^{32}P, ^{28}Si, ^{24}Mg as well as p, n and α's [338]. Unlike IceCube, LVS experiments are not typically large enough to satisfy the above condition for any reaction set. Overall, the results summarized in Fig. 4.4 indicate that the most massive composites accessible to terrestrial searches could be probed by current and future neutrino observatories, even for very weak couplings to the Standard Model.

4.3 Signatures at Astrophysical Objects

To conclude this Chapter, we also review some of the astrophysical signatures of composite states having weak couplings between their binding field and the Standard Model nucleon. Some potential signatures have been reviewed in [109] (see also [298] for a more general discussion with no coupling to the visible sector specified), however we emphasize that by no means all the possible implications of this model have been exhausted.

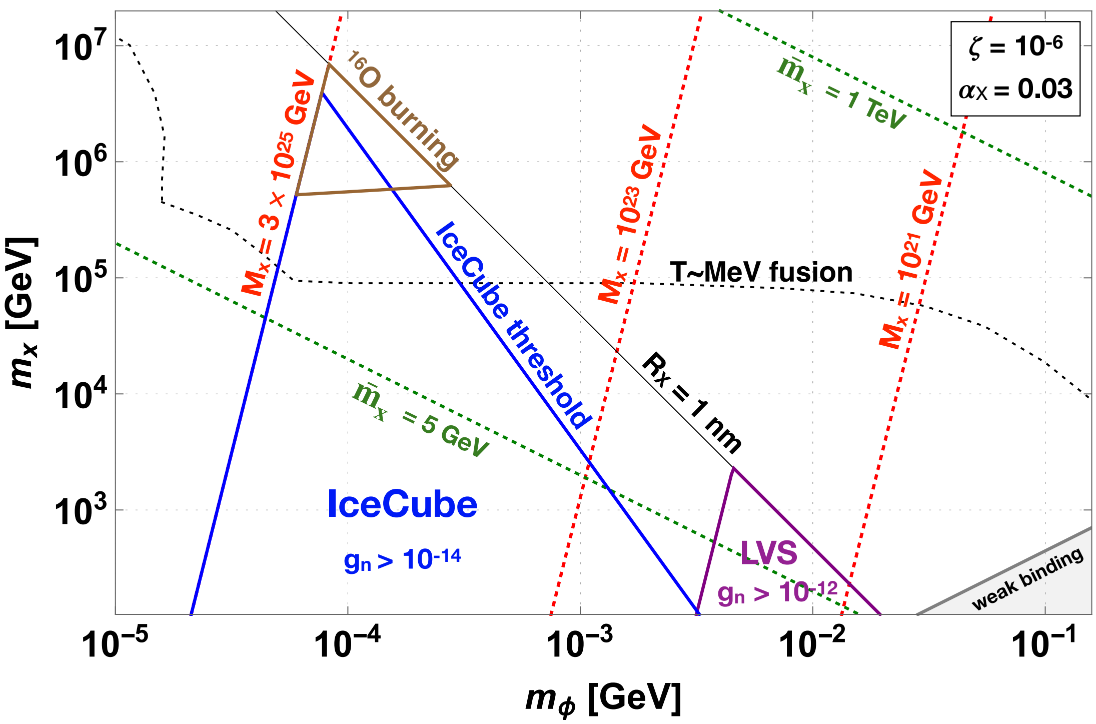

Figure 4.4: Heavy asymmetric composites that cause nuclei to radiate and fuse in their interiors, for fermion mass m_X, scalar mass m_ϕ, and ϕ - X coupling $\alpha_X = 0.03$. The total mass of the composites $M_X = N_c \bar{m}_X$ is shown with red dashed lines, determined by composite assembly after dark matter freeze-out, followed by a process that dilutes relic abundances by $\zeta = 10^{-6}$, *cf*. Eq. (4.11). The baryon and dark matter densities could arise from a common asymmetry for $\bar{m}_X \approx 5$ - 1000 GeV. Blue and purple regions show what composites can be discovered via bremsstrahlung radiation from ionized matter at IceCube and large volume scintillator (LVS) experiments, for ϕ-nucleon couplings $g_n \geq 10^{-14}$ and $g_n \geq 10^{-12}$ as indicated. For detection we require $R_X \gtrsim$ nm, so composites contain $\gtrsim 10$ atoms at solid Earth densities. Above the dotted line marked "T∼MeV fusion", the maximum g_n allowed by stellar bounds [331, 332], permits nuclei to be accelerated to MeV temperatures. In the tan wedges, composites can cause nuclei to fuse at IceCube. A strong binding condition $\alpha_X^2 m_X \gtrsim m_\phi$ [273] limits the lower gray area. See [108] for a more comprehensive version of this figure.

4.3.1 Ignition of Type-Ia Supernovae in White Dwarfs

For sufficiently large composite sizes and strong enough couplings to the Standard Model, the transit of a single composite state through the white dwarf can ignite Type-Ia supernovae. Indeed, in this Section, we examine how saturated composites produce enough localized heating via exothermic fusion reactions occurring in the dark matter composite interior, to initiate a thermonuclear runaway at the center of a carbon-oxygen (C/O) white dwarf [109]. In what follows, we shall refer to the ignition requirements already discussed in Sec. 2.1.4 which, roughly summarized, are: 1) a small sample of white dwarf material must be heated to a temperature $T_c \simeq 1$ MeV, and 2) the heating rate must exceed the dissipation rate of the sample. As we show below, these requirements translate into parameter space where composites could explode white dwarfs, and this parameter space region is subsequently constrained by the existence of massive white dwarfs that have not exploded so far, *cf.* the general discussion in Sec. 2.2.

To begin, we first comment on the velocity of nuclei in the white dwarf, relative to the transiting composites. Neglecting the initial halo velocity, dark matter composites will cross the white dwarf at approximately escape velocity, $v_{\rm esc} = (2GM_*/R_*)^{1/2} \simeq 3.5 \times 10^{-2}\ (M_*/1.3M_\odot)^{1/2}\ (R_*/3000\ \text{km})^{-1/2}$, where $M_\odot$ is a solar mass. We can directly compare this speed to the motion of the stellar constituents. For cold ~Gyr old white dwarfs, nuclei are arranged in a crystalline lattice, and we assume they vibrate in their zero point state $|0\rangle$ with a natural frequency given by the plasma frequency of the medium,

$$\Omega_p = \left(\frac{4\pi Z^2 e^2 n_N}{m_N}\right)^{\frac{1}{2}} \simeq 37\ \text{keV} \left(\frac{\rho_*}{10^9\ \text{g cm}^{-3}}\right)^{\frac{1}{2}} \left(\frac{Z}{6}\right) \left(\frac{A}{12}\right)^{-1}. \tag{4.42}$$

In such a state, their average velocity is $\langle 0|v|0\rangle = 0$, whereas the velocity dispersion is $\left(\langle 0|v^2|0\rangle\right)^{1/2} = \left(\Omega_p/m_N\right)^{1/2} \simeq 10^{-3} \ll v_{\rm esc}$, for $m_N \simeq 12$ - 16 GeV. Therefore, we safely assume nuclei to be at rest compared to the dark matter composite velocity in the stellar rest frame.

As discussed in App. B, dissipation processes occurring in the white dwarf material progressively slow the composite down, potentially preventing ignition at the center. The nuclei accelerated inside the composite scatter against the degenerate electrons of the white dwarf medium, which efficiently conduct heat. In addition, transiting nuclei can also radiate photons and neutrinos. Below, we discuss each of these energy loss channels in detail,

- *Electron conduction:* In Sec. 2.1.4, we have already discussed the electron conduction rate of the white dwarf material. In this case, a large temperature gradient is occurs near the composite boundary, and the energy loss due to heat conduction can be estimated by considering Eq. (2.33) and using the radius of the composite,

$$\begin{aligned}\dot{Q}_{\rm cond} =& \frac{4\pi^2 R_X T_c^3 (T_c - T_*)}{15\kappa_c \rho_*} \simeq \frac{4\pi^2 T_c^4 R_X}{15\kappa_c\rho_*} \\ &\simeq 10^{27}\ \text{GeV s}^{-1}\ \left(\frac{\rho_*}{10^9\ \text{g cm}^{-3}}\right)^{\frac{4}{15}} \left(\frac{R_X}{\mu\text{m}}\right). \end{aligned} \tag{4.43}$$

  In the second equality, as before, we have neglected the stellar background temperature compared to the critical ignition temperature.

- *Photon emission*: The heated stellar material inside the composite will also cool down by radiating photons. Due to the high opacity of the stellar material, photons will scatter many times inside the composite, thermalizing with the heated plasma. Therefore, we assume this cooling process can be modeled using a blackbody radiation spectrum at temperature T_c. The rate at which energy is radiated out of a composite of radius R_X is [122],

$$\begin{aligned} \dot{Q}_{\rm rad} =& \frac{4\pi R_X^2 \sigma_{\rm SB} \nabla T^4}{\kappa_r \rho_*} \simeq \frac{16\pi R_X^2 \sigma_{\rm SB} m_\phi T_c^4}{\kappa_r \rho_*} \\ &\simeq 10^{24}\ {\rm GeV\ s^{-1}} \left(\frac{m_\phi}{\rm keV}\right) \left(\frac{R_X}{\mu{\rm m}}\right)^2, \end{aligned} \tag{4.44}$$

where $\sigma_{\rm SB} = \pi^2/60$ is the Stefan-Boltzmann constant in natural units, and $\kappa_r \simeq 10^7\ {\rm cm^2\ g^{-1}}\ (T_*/10^7\ {\rm K})^{-7/2}\ (\rho_*/10^9\ {\rm g\ cm^{-3}})$ is the white dwarf radiative opacity for free-free electron transitions [343, 105]. In the second equality, we have approximated the temperature gradient $\nabla T^4 = 4T^3 \nabla T \simeq 4T_c^3 \left((T_c - T_*)/m_\phi^{-1}\right) \simeq 4 m_\phi T_c^4$. This approximation is accurate for saturated composites because $m_\phi^{-1} \ll R_X$, so the potential is short-ranged compared to the composite size.

- *Neutrino emission*: At the critical temperature T_c, neutrino emission is dominated by electron-positron annihilation, with an emission rate of (10^{29} - 10^{30}) GeV cm^{-3} s^{-1} in the stellar density range (10^8 - 10^{10}) g cm^{-3} [344, 345, 346]. The white dwarf material is transparent to neutrinos of $\sim$ MeV energies, and so they escape the star carrying all of their energy away. This yields a neutrino energy loss rate of order $\dot{Q}_\nu \simeq 10^{18}\ {\rm GeV\ s^{-1}}\ (R_X/\mu{\rm m})^3$.

Comparing these energy loss mechanisms, we see that photon and neutrino losses will be sub-dominant compared to electron conduction unless composites have radii $R_X \gtrsim 0.1$ cm and $R_X \gtrsim 100$ cm respectively. However as we detail below, composites in excess of $R_X \gtrsim 1$ cm will be too scarce in dark matter halos and therefore unable to explode white dwarfs on ∼Gyr timescales. Thus, we are only concerned with the energy loss from conduction and, at the highest composite masses and radii, radiation emission.

We now turn to the question of whether composites will be stopped through dissipative processes as they cross the white dwarf. Let us compare the above energy loss rates to the composite kinetic energy at the surface of the white dwarf, and the white dwarf crossing time. The initial composite kinetic energy at the star surface is

$$\frac{1}{2}M_X v_{\rm esc}^2 \simeq 10^{27}\ \text{GeV}\left(\frac{M_X}{10^{30}\ \text{GeV}}\right)\left(\frac{v_{\rm esc}}{3\times 10^{-2}}\right)^2. \tag{4.45}$$

For sub-Chandrasekhar white dwarfs, with radii ranging (2500 - 3000) km, composites will cross the star in ~ 1 s, given their escape velocity at the surface. Thus, comparing Eq. (4.45) to the conduction and radiation losses above, we see that composites of masses $M_X \gtrsim 10^{30}$ GeV will not be significantly stopped by these dissipation processes, and are able to reach the ignition point at center of the star.

Next, to determine whether the composite can cause a thermonuclear runaway, we must compare the above cooling rates to a number of timescales relevant for thermonuclear reactions inside the composite as it crosses the white dwarf. First, we look at the timescale for stellar material to be heated as it crosses the dark matter composite's boundary. The heat capacity of the white dwarf ions is $C_v \simeq 2\pi\rho_* R_X^3/m_N$. Utilizing the nuclear acceleration timescale, *cf.* Eq. (4.17), we estimate the heating rate of the stellar material from accelerating across the composite boundary to be

$$\dot{Q}_{\rm nuc} \simeq C_v\ T_c\ \tau_{\rm accel}^{-1} \simeq 10^{34}\ \text{GeV s}^{-1}\left(\frac{v_X}{10^{-2}}\right)\left(\frac{m_\phi}{\text{keV}}\right)\left(\frac{\rho_*}{10^9\ \text{g cm}^{-3}}\right)\left(\frac{R_X}{\mu\text{m}}\right)^2. \tag{4.46}$$

This is much larger than the above cooling rates for the parameters indicated. Hence, for composites with radii $R_X \gtrsim 10^{-2}$ μm, $\dot{Q}_{\rm nuc} \gg \dot{Q}_{\rm cond}, \dot{Q}_{\rm rad}$, and so neither conductive nor radiative losses prevent stellar material from being rapidly heated to the critical ignition temperature during the composite transit.

The same cooling mechanisms discussed above must also be compared to the timescale required for the thermonuclear runaway itself. Specifically, to ignite the white dwarf star we must require the heat diffusion rate to fall below the rate at which energy is released from the thermonuclear reactions. At the critical temperature T_c, the ions can be treated as an ideal gas, and nuclear reactions proceed in the classical thermonuclear regime, *i.e.* screening effects are negligible. For a C/O white dwarf, there will be three primary fusion processes we will consider: $^{12}\text{C} +^{12}\text{C}$, $^{12}\text{C} +^{16}\text{O}$ and $^{16}\text{O} +^{16}\text{O}$. These reactions respectively produce the compound nuclei ^{24}Mg, ^{28}Si and ^{32}S, each decaying via n-, p- and α- channels. The nuclear burning rate is set by the astrophysical S-factor which determines the fusion cross section at low energies, as well as the Coulomb barrier penetration factor, which are extensively discussed in [347, 348]. Using the formalism outlined in these References, we find the specific rates for each reaction per unit volume,

$$\left.\frac{d\dot{R}_{\rm C+C}}{dV}\right|_{T_c} \simeq 10^{43}\ \text{cm}^{-3}\ \text{s}^{-1} \left(\frac{\text{X}_\text{C}}{0.5}\right)^2 \left(\frac{\rho_*}{10^9\ \text{g cm}^{-3}}\right)^2, \tag{4.47}$$

$$\left.\frac{d\dot{R}_{\rm C+O}}{dV}\right|_{T_c} \simeq 10^{42}\ \text{cm}^{-3}\ \text{s}^{-1} \left(\frac{\text{X}_\text{C}}{0.5}\right) \left(\frac{\text{X}_\text{O}}{0.5}\right) \left(\frac{\rho_*}{10^9\ \text{g cm}^{-3}}\right)^2, \tag{4.48}$$

$$\left.\frac{d\dot{R}_{\rm O+O}}{dV}\right|_{T_c} \simeq 10^{40}\ \text{cm}^{-3}\ \text{s}^{-1} \left(\frac{\text{X}_\text{O}}{0.5}\right)^2 \left(\frac{\rho_*}{10^9\ \text{g cm}^{-3}}\right)^2, \tag{4.49}$$

where $X_C + X_O = 1$ are the mass fractions of carbon and oxygen. Each fusion process releases $Q_{\rm C+C} \simeq 3.16$ MeV, $Q_{\rm C+O} \simeq 6.51$ MeV and $Q_{\rm O+O} \simeq 13.09$ MeV of average heat per reaction [338]. The subsequent nuclear energy release rate is,

$$\dot{Q}_{\rm fus} \simeq \frac{4\pi}{3}\left(\sum_{j={\rm CC,CO,OO}} Q_j \frac{d\dot{R}_j}{dV}\bigg|_{T_c} \right) R_X^3 \tag{4.50}$$

The nuclear energy release rate Eq. (4.50) scales as R_X^3, whereas the heat conduction rate, Eq. (4.43), and the photon emission rate, Eq. (4.44), only scale as R_X and R_X^2 respectively. This implies that there is a minimum composite radius for which the nuclear energy released exceeds the dissipation rate and the runaway commences. For concreteness, we consider two benchmark cases: a pure $X_{\rm C} = 1$ composition, and an $X_{\rm C} = X_{\rm O} = 0.5$ C/O mixture. Using the reaction rates above, we obtain a nuclear energy release rate of $\dot{Q}_{\rm fus} \simeq 10^{33}$ GeV s^{-1} $(\rho_*/10^9 \text{ g cm}^{-3})^2(R_X/\mu\text{m})^3$ for pure carbon, and $\dot{Q}_{\rm fus} \simeq 4 \times 10^{32}$ GeV s^{-1} $(\rho_*/10^9 \text{ g cm}^{-3})^2(R_X/\mu\text{m})^3$ for a C/O mixture. For both benchmark compositions, composites with radii above $R_X \gtrsim 10^{-2}$ μm will satisfy $\dot{Q}_{\rm nuc} \gg \dot{Q}_{\rm cond}, \dot{Q}_{\rm rad}$. Using Eq. (4.6), this implies a minimum composite mass $M_X \gtrsim 10^{23}$ GeV, which is smaller than the required mass for the composites to reach the stellar core, *cf*. Eq. (4.45) and surrounding discussion. Thus, we conclude that composites with masses and radii

$$M_X \gtrsim 10^{30} \text{ GeV} \quad , \quad R_X \gtrsim 10^{-2}\ \mu\text{m} \tag{4.51}$$

are capable of reaching the core of a massive C/O white dwarf and ignite a nuclear runaway, so long as their coupling to SM nucleons is sufficiently strong. Such minimum coupling is determined from the critical temperature by setting Eq. (4.16) equal to T_c. Following this procedure, the minimum coupling for igniting a thermonuclear runaway in the white dwarf is

$$g_n \gtrsim 10^{-12} \left(\frac{m_X}{10^8 \text{ GeV}} \right)^{-1}. \tag{4.52}$$

We remark that given stellar cooling constraints, which already bound the coupling $g_n \lesssim 10^{-12}$ for mediators with masses $\lesssim$ keV, typically it will be composite states made of heavy $m_X \gg$ PeV constituents, which have a sufficiently strong potential, that will cause a white dwarf star to explode, as we explored in [108]. Thus, a cosmological synthesis with a dilution stage is necessary to synthesize composites with an adequate size and coupling to produce Type-Ia supernovae, *cf.* $\zeta \ll 1$ in Eq. (4.11).

As discussed in Sec. 2.2, the existence of old white dwarfs in the mass range (1.1 - 1.4) $M_\odot$, corresponding to approximate central densities $\rho_* \simeq (10^8$ - $10^{10})$ g cm^{-3}, implies constraints on the nucleon-dark matter coupling g_n, assuming at least one encounter with a composite occurred in their $\sim$ Gyr lifespan. First, we comment on the robustness of our results in relation to the thermonuclear reaction set considered, *cf.* Eqs. (4.47)-(4.49). Although a fraction of massive white dwarfs will possess O/Ne cores, which have not been accounted for here, we remark that multiple studies [349, 350, 351] indicate that an $\mathcal{O}(1)$ fraction of massive C/O white dwarfs are formed as the result of binary mergers [352, 353]. Furthermore, there exist single-evolution channels by which massive C/O white dwarfs may form, such as reduced mass loss rates in the asymptotic giant branch phase [354, 355] or enhanced rotation [356, 355]. Searching the Montreal White Dwarf Database [111], we find an $\sim \mathcal{O}(10^3)$ sample of single white dwarfs in the mass range of interest, with cooling ages ranging 1 - 5 Gyr at distances $\lesssim 10^3$ pc. Based on the above considerations, a fraction of this sample must be C/O white dwarfs that have not exploded, implying that either ignition conditions were not satisfied, or else they have not encountered a composite in their lifetime. The former condition constrains g_n according to Eq. (4.52), whereas the latter condition implies that such constraints are valid for composites with masses $M_X \lesssim 10^{42}$ GeV, assuming a dark matter halo density $\rho_X \simeq 0.4$ GeV cm^{-3}. We emphasize that any C/O white dwarf within this mass range will impose a similar condition on the minimum mass and radius of ignition-capable composites, since the central density spans ~ 2 orders of magnitude, resulting in an $\sim \mathcal{O}(1)$ correction factor to the minimum composite radius for ignition.

4.3.2 Planetary Heating

The implications of this model for planetary heating have also been discussed in [109], and we review them here as well. Although a number of works have studied the impact of dark matter on planets and their satellites [357, 358, 359, 360, 361, 339, 362, 363, 364, 69, 365], the specifics of the model considered here requires further investigation. In particular, constraints have been placed on different dark matter models based on the heat that captured dark matter would produce in the Earth's core from annihilation [359, 361, 339] or gravitational collapse into evaporating black holes [69], which would exceed the $\dot{Q}_\oplus \lesssim 44$ TW $\simeq 10^{23}$ GeV s^{-1} of heat flow from the surface of the Earth [366, 367]. In this Section, we discuss the potential heat signature produced by large composites in the Earth's mantle and core and argue that, although a significant fraction of the composite dark matter flux can be gravitationally captured by the Earth, these composites do not necessarily produce a heat flow comparable to the observed value.

Composite dark matter can be captured by the Earth's crust and mantle from the various energy dissipation mechanisms which, as detailed in Appendix B, translates into kinetic energy loss as it travels through matter. The composite dark matter number flux through the Earth is

$$\Phi_X = 2\pi R_\oplus^2 \langle v_X \rangle \frac{\rho_X}{M_X} \simeq 10^5 \text{ s}^{-1} \left(\frac{M_X}{10^{20} \text{ GeV}} \right)^{-1}, \tag{4.53}$$

where $R_\oplus = 6371$ km is the radius of the Earth, $\langle v_X \rangle \simeq 300$ km s^{-1} is the average dark matter velocity entering the Earth, and $\rho_X \simeq 0.4$ GeV/cm^3 is the local dark matter mass density [359, 323, 368, 339]. By itself, the kinetic energy of this dark matter flux falls well short of the observed heat flow of the Earth. Each composite has a kinetic energy of order $\sim 10^{13}$ GeV $(M_X/10^{20}$ GeV$)(v_X/300$ km s$^{-1})^2$, in contrast with the $\sim \dot{Q}_\oplus/\Phi_X \simeq 10^{18}$ GeV $(M_X/10^{20}$ GeV$)$ required per composite to produce an observable deviation in the Earth's heat flow. However, we must consider if the composites that are captured release further energy into the core and mantle through nuclear collisions and reactions in their interiors. At temperatures $\gtrsim 100$ keV, thermal bremsstrahlung will significantly stop composites in the mantle, *cf.* Eq. (4.41), which will then slowly drift and settle at the core, on a timescale that can be computed using the methods described in [339, 69]. Given that the mantle composition is predominantly ^{16}O, we expect sizeable oxygen burning reactions to occur at such temperatures. Once the composites have settled at the core, they could later release heat as matter is accumulated in their interior, since matter they accumulate will have fallen into the composite's potential, and would radiate a corresponding amount of potential energy. Finally, we should also consider whether these dark matter states might congregate at the center of the Earth and gravitationally collapse into a black hole light enough to evaporate via Hawking radiation, provided enough dark matter is captured [69]. Below we detail each of these processes,

- *Fusion reactions:* The captured composites could release heat via fusion reactions occurring in their interiors. The Earth's mantle is mostly composed of ^{16}O and silicon [369, 370, 371], while the core is mostly composed of ^{56}Fe [372], which can no longer fuse and therefore is not considered in this analysis. Oxygen burning is the only plausible reaction that can occur at temperatures $T \sim 100$ keV - 1 MeV, with a highly temperature-dependent rate we extract from [338]. To achieve such temperatures, given that stellar cooling constraints limit the dark matter-nucleon coupling to $g_n \lesssim 10^{-12}$ - 10^{-10} in the eV - GeV mediator range, constituent masses must be in excess of $m_X \gtrsim 10^6$ GeV. In $t_\oplus \simeq 4.5$ Gyr $\simeq 10^{17}$ s, about 10^{22} $(M_X/10^{20}$ GeV$)^{-1}$ composites are captured. Each of them must then release at least 10 GeV s^{-1} $(M_X/10^{20}$ GeV) to produce $\dot{Q}_\oplus$. However, the energy released from oxygen burning reactions per composite is $\sim 10^{-1}$ GeV s^{-1} $(M_X/10^{20}$ GeV$)(\bar{m}_X/5$ GeV$)^{-4}$. Thus, oxygen fusion reactions in the mantle triggered by these composites cannot substantially alter the observed Earth heat flow.

- *Gravitational collapse*: The composites accumulated in the Earth's core will eventually fuse into a single larger composite state. We do not discuss the timescale for such process here. Instead, we point out that if the critical mass is exceeded, the dark matter will collapse into a black hole which can either overheat or destroy the Earth depending on its initial mass, as discussed extensively in [69]. However, the critical mass for collapse is $M_{\rm coll} \simeq M_{pl}^3/\bar{m}_X^2 \simeq 10^{55}$ GeV $(\bar{m}_X/5$ GeV$)^{-2}$ [129] (for reference, a solar mass is $\sim 10^{57}$ GeV). The total dark matter mass flux, on the other hand, is $2\pi R_\oplus^2 \langle v_X \rangle \rho_X \simeq 10^{25}$ GeV s^{-1}, *cf.* Eq. (4.53), and therefore insufficient for the critical mass to be accumulated in $t_\oplus \simeq 4.5$ Gyr $\simeq 10^{17}$ s.

- *Matter compression:* A detailed study of the phase of matter after a captured composite has settled is out of the scope of this work. A simple estimate, however, indicates that the heat released as nuclei settle in the composite interior is insufficient to produce $\dot{Q}_\oplus$. As specified above, each captured composite would need to deposit $\sim \dot{Q}_\oplus/\Phi_X \simeq 10^{18}$ GeV $(M_X/10^{20}$ GeV$)$ in the form of compressional heating once they reach the core and thermalize. By contrast, nuclei would ultimately release an energy of order $\langle\varphi\rangle$ in the form of heat, resulting in a total energy deposition of $n_N \langle\varphi\rangle R_X^3 \sim$ MeV $(n_N/10^{23}$ cm$^{-3})(\langle\varphi\rangle/\text{MeV})(M_X/10^{20}$ GeV$)(\bar{m}_X/5$ GeV$)^{-4}$, where the number density has been normalized to the Earth's inner core value. However, it is probably the case that Standard Model nuclear material collected into the composite will continue to accumulate, potentially reaching a density well beyond 10^{23} cm^{-3}, until it is stabilized against further accumulation by electron or nucleon degeneracy pressure. Put differently, we should consider whether nuclei continue to collect until the interior of dark matter composites resembles "white dwarf" or "neutron star" material. In this case, the above estimates indicate that composites with an extremely small in-medium mass (*e.g.* $\bar{m}_X \ll 5$ MeV, assuming a 10^{32} cm^{-3} "WD" nuclear density) may appreciably heat the Earth. We leave a proper study of this phenomenon to future work.

From these estimates we conclude that, while dark matter composites captured by the Earth may be responsible for a fraction of its observed heat output, they cannot account for the total flow observed, either via fusion reactions or gravitational collapse. On the other hand, in the case of "matter compression", a bound might be attained for larger composites than those we consider. In such a case, that the accumulated nuclear material inside the composite comes to exceed terrestrial densities by many orders of magnitude. This possibility is still open to future inquiry, since this will depend on the eventual equilibrium state of nuclei inside very large dark matter composites that settled at the Earth's core.

Chapter 5

Summary and Conclusions

5.1 Summary

In this thesis, we have reviewed a plethora of results on (mostly) heavy dark matter signatures in compact stars and underground experiments. Before finishing with some general conclusions, it is prudent to summarize all the main findings we have covered, and convey their implications.

In the first Chapter, we have shown how asymmetric heavy dark matter might be responsible for triggering Type-Ia supernovae in white dwarf stars. We assumed that the dark matter does not possess any sizeable self-interactions, it scatters with Standard Model nuclei via the exchange of some heavy mediator, and its mass is $\gtrsim 10^6$ GeV. As detailed before, cosmologies for the synthesis of such heavy dark matter can be successfully constructed. The accumulation and eventual collapse of this dark matter inside white dwarfs is a potential explanation for recent findings indicating that some of these objects are exploding without the presence of a binary companion. Depending on their cross section, a fraction dark matter particles crossing the star will lose energy and become gravitationally bound to it. These dark matter particles then repeatedly cross the star, losing more energy and eventually become contained in it. The dark matter core that forms at the center grows over time, eventually becoming gravitationally unstable. As this dark matter core collapses, one of two alternatives may occur,

- If the cross section is large enough, the frequent scatters between the dark matter particles and the white dwarf nuclei will substantially heat a small region of the core, leading to a thermonuclear runaway in the star.

- Otherwise, if the cross section is too small, the dark matter core will collapse to a black hole, provided no additional source of pressure can stabilize collapse. For the parameter space considered, this is always the case provided self-interactions are not exceedingly strong. If the dark matter is lighter than $\sim 10^{12}$ GeV, the nascent black hole is heavy enough that it grows by accretion of stellar material and dark matter, imploding the star. Alternatively, if the dark matter is heavier than this value, then the black hole is so light that it rapidly evaporates into mostly hadronic particles, which in turn deposit sizeable energy in a small region of the core, igniting it.

Overall, we have seen that for a wide region of dark matter parameters, and very general assumptions on its self-interactions, ignition via one of the two channels above can proceed. We have computed the overall timescale for this ignition process and, by comparing it to the cooling age of an old white dwarf that has not exploded, we have set bounds on the dark matter-nucleon cross section. The evaluation of such a timescale required novel considerations on the white dwarf microscopic structure, and how the different scattering regimes change in each stage of the process. To illustrate the reach of the derived bounds, we have mapped them into two specific models whereby the dark matter interacts through a vector (dark photon) mediator or a scalar (Higgs portal) mediator with the Standard Model. The vector portal model, in particular, allows for much faster explosion times since dark matter can scatter against electrons, leading to stronger constraints based on white dwarf survival.

Some comments are in order about the uncertainty on the constraints derived based on the $\sim$ Gyr existence of white dwarfs. The thermonuclear runaway process in white dwarfs lighter than $\sim 1.1 M_{\odot}$ is not robustly understood. Therefore, only heavier white dwarfs must be considered when setting bounds using this method. For white dwarfs above this mass threshold, various simulation works reasonably agree on the conditions for a successful ignition. Although the white dwarf star that we selected from the Montreal White Dwarf Database places the most competitive constraint, other white dwarfs in the higher mass end yield very similar bounds. In [102], a more comprehensive discussion of the variation of these results with the choice of white dwarfs can be found.

In the second Chapter, we have discussed how the thermal evolution of neutron stars can place leading bounds on dark matter interactions with nucleons, utilizing next-generation infrared telescopes. We considered dark matter in the mass range $\sim$ MeV up to $\sim 10^6$ GeV, whereby a single scatter against the neutron star constituents is sufficient for the dark matter particles to become gravitationally bound to the star, and subsequently thermalize with it on a short timescale. Furthermore, we assumed that the dark matter can either be symmetric or asymmetric, and as before it scatters against nucleons through the exchange of some heavy mediator. Constraints on dark matter-nucleon interactions are placed by comparing the effective temperature of an old isolated neutron star to the value we expect from dark matter constantly falling into the star and depositing its kinetic energy through scatterings. The caveat to this proposal is the potential existence of exotic phases of matter in the core, which may prevent dark matter from scattering and depositing energy altogether. Our knowledge of the neutron star crust, by contrast, is substantially more robust than the core. In fact, the majority of recent works agree to a good level of precision on all its basic properties, including the composition of each layer, and the densities at which each relevant transition occurs. Building on prior works, we have demonstrated how this knowledge of the crust alone would permit us to robustly constrain dark matter interactions without having to consider the uncertain physics of the neutron star core. This implies that forthcoming infrared telescopes are guaranteed to observe or constrain dark matter heating of neutron stars via crust-only scattering.

Computing the effects of dark kinetic heating of the crust requires evaluating how each crust layer responds to different momentum transfers, which in turn depends on the mass of the infalling dark matter. The optical depth of each crustal layer, and the resulting senstivity projection, was thoroughly analyzed,

- The outer crust is a crystalline lattice of heavy nuclei, where coherent nuclear scattering is suppressed due to structural effects at large momentum transfers. Instead, we considered dark matter scattering against loosely bound nucleons within the nuclei. We found that kinetic heating of this layer alone is sensitive electroweak-scale dark matter with cross sections of $\sim 10^{-40}$ cm^2.

- The inner crust is structurally similar to the outer crust, however it has two key differences: nuclei are far heavier and neutron-richer, and there is a large population of unbound neutrons forming a superfluid phase at sufficiently low temperatures. The same considerations for dark matter scattering in the outer crust apply here, although the inner crust substantially contributes to the total optical depth of the crust. Dark kinetic heating of this layer provides sensitivity to smaller cross sections of order $\sim 10^{-41}$ cm^2.

In addition, one can consider dark matter scattering against phonons in the unbound neutron phase. This provides cross section sensitivities of 10^{-39} - 10^{-34} cm^2, for dark matter as light as 10 eV up to 10 MeV mass. This is a secondary result that requires further investigation.

- Although technically part of the inner crust as well, the nuclear pasta phases deserve a separate discussion. These are nuclear structures of complicated shape that dark matter can scatter against. Using structure factors numerically computed in molecular dynamics simulations of these phases, we have computed their corresponding optical depth and found there is a substantial coherent enhancement in the scattering for dark matter in the mass range 100 MeV - 1 GeV. This layer, although shallower compared to the rest of the layers, contains most of the crustal mass, and is the dominant contribution to the optical depth. For the maximum enhancement, the nuclear pasta sensitivity reaches cross sections down to 10^{-43} cm^2.

The above sensitivity projections are valid for dark matter in the mass range 100 MeV - 10^6 GeV, outside of which Pauli-blocking and multi-scatter capture would need to be accounted for. Although the inferred constraints are weaker compared to dark matter fully scattering in the core, they are considerably more robust and certainly still competitive with underground experiments. This result alone sets a compelling case for further investigating neutron star heating as a dark matter detection method.

The results presented here also have important implications for dark matter thermalization in neutron stars. If dark matter-core interactions do not exist or are highly suppressed, once dark matter particles have settled in orbits contained below the crust, no further energy would be lost, limiting the total amount of energy imparted by dark matter particles. However, if the dark matter particles, which remain oscillating inside the star, annihilate to Standard Model particles, these annihilation products transfer the remaining energy to the star. We have found that, with crust-only interactions, the time required to reach capture-annihilation equilibrium is much shorter than the ages of old neutron stars for thermal annihilation cross sections. We have therefore shown that dark matter can thermalize in neutron stars, without having to consider the largely uncertain physics of the core. Additionally, we have also verified that substantial sensitivity is achievable using the crust for inelastic dark matter models. As an explicit example, we evaluated sensitivity projections for a thermal Higgsino dark matter model.

In the third Chapter, we have reviewed new signatures of composite dark matter. In particular, we considered a simple model of dark matter fermions bound by some light scalar, and showed that when this light scalar is coupled to Standard Model particles, new and rich phenomenology is uncovered. These composites can form in the early universe through successive dark fusion reactions and, if their cosmological synthesis includes additional dilution stages, can have masses ranging from $\sim 10^{10}$ GeV up to $\sim 10^{45}$ GeV. After synthesis, these composite states have a large number of constituents that effectively source a scalar potential under which nuclei can accelerate to significant energies. This effect is prominent even in the limit of weak couplings between the dark matter and the Standard Model. We first discussed the relevant signatures at underground experiments,

- Liquid noble element experiments: The passage of composite states through matter simultaneously recoils so many atoms, that a fraction of them undergo ionization from the jolt, *i.e.* the so-called Migdal effect. Noble element-based detectors like XENON-1T, given their high ionization probabilities and low electron backgrounds, are highly sensitive to the composite passage. This is the case even for extremely weak couplings between the dark matter and the Standard Model.

- Neutrino observatories: Composites heavier than about $\sim 10^{18}$ GeV are mostly out of the reach of direct detection experiments, given the dark matter flux passing through them. However, these heavier composites could still be detected at large neutrino observatories like IceCube, or scintillator-based experiments like SNO+, due to their large sizes and long operation times. At the same time, large composite states typically source so strong fields that matter passing through the composite is fully ionized, producing sizable amounts of thermal radiation and even nuclear reactions. This massive energy deposition easily exceeds the detection thresholds of these experiments.

We have indicated regions of parameter space where both direct detection experiments like XENON-1T, and neutrino observatories like IceCube or SNO+, could observe the transit of these composite states. In particular, using existing XENON-1T data, we have set bounds on the composite-nucleus coupling by comparing the expected number of events to the few recorded electron recoil events. Couplings as low as $\sim 10^{-17}$ can be constrained with this method, which lie several orders of magnitude below the most stringent constraints based on stellar cooling considerations.

Finally, we have also shown how the transit of large composite states through white dwarfs could spark supernovae. We found that composites heavier than $\sim 10^{30}$ GeV and larger than $\sim 10^{-2}$ μm can reach the core of a white dwarf star and ignite it, provided their coupling to Standard Model nuclei is strong enough. Similar to the case of point-like asymmetric dark matter, the survival of these objects also implies constraints on the coupling, assuming at least one encounter with a composite state during their lifetime. We have also discussed how composites can accumulate in planets and alter their heat flow. Although initial considerations indicate that this effect is not prominent, further investigation is required on the overall effect of composite state capture and accumulation in stellar objects.

5.2 Conclusions

The nature of dark matter remains elusive, yet its discovery prospects are increasingly optimistic. Extensive direct, indirect and collider searches for dark matter are either underway or planned, and are rapidly closing many existing gaps in the parameter space. In this thesis, we have only covered a tiny fraction of all the existing phenomenology, both in astrophysical objects and underground experiments, with the hope of further constraining –or perhaps discovering– dark matter.

As closing remarks, we point out that several aspects of the research discussed here deserve further investigation in the future. The results on dark matter scattering in compact stars illustrate the need for appropriately modelling the response of the material to dark matter, as this can have a major impact on the constraints or sensitivity projections that are ultimately derived. Although some recent works on dark matter signatures in stellar objects are starting to account for structural effects in dark matter scattering, in most of the literature these considerations are missing. A suitable modelling of structure functions will be paramount as new instruments searching for dark matter in astrophysical probes come online. On the other hand, the novel phenomenology of composite dark matter discussed here requires much further exploration. Alternative composite dark matter theories, with more complicated field content, could present a similar nuclear acceleration effect. For instance, this could mean direct detection experiments are highly sensitive to other types of weakly-coupled composite states by considering the Migdal effect. This remains unexplored so far, and as shown here with the simplest composite dark matter model, has the potential to push the detection frontier by several orders of magnitude.

Bibliography

[1] G. Bertone and D. Hooper, *History of dark matter*, *Rev. Mod. Phys.* **90** (2018) 045002, [1605.04909].

[2] G. Bertone, D. Hooper and J. Silk, *Particle dark matter: Evidence, candidates and constraints*, *Phys. Rept.* **405** (2005) 279–390, [hep-ph/0404175].

[3] Y. b. Zeldovich, *Survey of Modern Cosmology*, *Adv. Astron. Astrophys.* **3** (1965) 241–379.

[4] B. W. Lee and S. Weinberg, *Cosmological Lower Bound on Heavy Neutrino Masses*, *Phys. Rev. Lett.* **39** (1977) 165–168.

[5] P. Gondolo and G. Gelmini, *Cosmic abundances of stable particles: Improved analysis*, *Nucl. Phys. B* **360** (1991) 145–179.

[6] G. Jungman, M. Kamionkowski and K. Griest, *Supersymmetric dark matter*, *Phys. Rept.* **267** (1996) 195–373, [hep-ph/9506380].

[7] T. Moroi, H. Murayama and M. Yamaguchi, *Cosmological constraints on the light stable gravitino*, *Phys. Lett. B* **303** (1993) 289–294.

[8] T. Asaka, K. Ishiwata and T. Moroi, *Right-handed sneutrino as cold dark matter*, *Phys. Rev. D* **73** (2006) 051301, [hep-ph/0512118].

[9] M. Shaposhnikov and I. Tkachev, *The nuMSM, inflation, and dark matter*, *Phys. Lett. B* **639** (2006) 414–417, [hep-ph/0604236].

[10] A. Kusenko, *Sterile neutrinos, dark matter, and the pulsar velocities in models with a Higgs singlet*, *Phys. Rev. Lett.* **97** (2006) 241301, [hep-ph/0609081].

[11] L. J. Hall, K. Jedamzik, J. March-Russell and S. M. West, *Freeze-In Production of FIMP Dark Matter*, *JHEP* **03** (2010) 080, [0911.1120].

[12] K. M. Zurek, *Asymmetric Dark Matter: Theories, Signatures, and Constraints*, *Phys. Rept.* **537** (2014) 91–121, [1308.0338].

[13] K. Petraki and R. R. Volkas, *Review of asymmetric dark matter*, *Int. J. Mod. Phys.* **A28** (2013) 1330028, [1305.4939].

[14] M. J. Baker, M. Breitbach, J. Kopp and L. Mittnacht, *Primordial Black Holes from First-Order Cosmological Phase Transitions*, 2105.07481.

[15] M. J. Baker, M. Breitbach, J. Kopp and L. Mittnacht, *Detailed Calculation of Primordial Black Hole Formation During First-Order Cosmological Phase Transitions*, 2110.00005.

[16] P. Asadi, E. D. Kramer, E. Kuflik, G. W. Ridgway, T. R. Slatyer and J. Smirnov, *Accidentally Asymmetric Dark Matter*, *Phys. Rev. Lett.* **127** (2021) 211101, [2103.09822].

[17] P. Asadi, E. D. Kramer, E. Kuflik, T. R. Slatyer and J. Smirnov, *Glueballs in a Thermal Squeezeout Model*, 2203.15813.

[18] Y. Tang and Y.-L. Wu, *On Thermal Gravitational Contribution to Particle Production and Dark Matter*, *Phys. Lett. B* **774** (2017) 676–681, [1708.05138].

[19] Y. Mambrini and K. A. Olive, *Gravitational Production of Dark Matter during Reheating*, *Phys. Rev. D* **103** (2021) 115009, [2102.06214].

[20] D. Carney et al., *Snowmass2021 Cosmic Frontier White Paper: Ultraheavy particle dark matter*, 2203.06508.

[21] J. Alexander et al., *Dark Sectors 2016 Workshop: Community Report*, 8, 2016. 1608.08632.

[22] M. Schumann, *Direct Detection of WIMP Dark Matter: Concepts and Status*, *J. Phys. G* **46** (2019) 103003, [1903.03026].

[23] XENON collaboration, E. Aprile et al., *First Dark Matter Search Results from the XENON1T Experiment*, *Phys. Rev. Lett.* **119** (2017) 181301, [1705.06655].

[24] XENON collaboration, E. Aprile et al., *Constraining the spin-dependent WIMP-nucleon cross sections with XENON1T*, *Phys. Rev. Lett.* **122** (2019) 141301, [1902.03234].

[25] XENON collaboration, E. Aprile et al., *Excess electronic recoil events in XENON1T*, *Phys. Rev. D* **102** (2020) 072004, [2006.09721].

[26] DEAP collaboration, R. Ajaj et al., *Search for dark matter with a 231-day exposure of liquid argon using DEAP-3600 at SNOLAB*, *Phys. Rev. D* **100** (2019) 022004, [1902.04048].

[27] (DEAP Collaboration)‡, DEAP collaboration, P. Adhikari et al., *First Direct Detection Constraints on Planck-Scale Mass Dark Matter with Multiple-Scatter Signatures Using the DEAP-3600 Detector*, *Phys. Rev. Lett.* **128** (2022) 011801, [2108.09405].

[28] LUX collaboration, D. S. Akerib et al., *Results from a search for dark matter in the complete LUX exposure*, *Phys. Rev. Lett.* **118** (2017) 021303, [1608.07648].

[29] LUX collaboration, D. S. Akerib et al., *Limits on spin-dependent WIMP-nucleon cross section obtained from the complete LUX exposure*, *Phys. Rev. Lett.* **118** (2017) 251302, [1705.03380].

[30] LUX collaboration, D. S. Akerib et al., *Results of a Search for Sub-GeV Dark Matter Using 2013 LUX Data*, *Phys. Rev. Lett.* **122** (2019) 131301, [1811.11241].

[31] PandaX-II collaboration, Q. Wang et al., *Results of dark matter search using the full PandaX-II exposure*, *Chin. Phys. C* **44** (2020) 125001, [2007.15469].

[32] PandaX-4T collaboration, Y. Meng et al., *Dark Matter Search Results from the PandaX-4T Commissioning Run*, *Phys. Rev. Lett.* **127** (2021) 261802, [2107.13438].

[33] DarkSide collaboration, P. Agnes et al., *Low-Mass Dark Matter Search with the DarkSide-50 Experiment*, *Phys. Rev. Lett.* **121** (2018) 081307, [1802.06994].

[34] J. Billard, L. Strigari and E. Figueroa-Feliciano, *Implication of neutrino backgrounds on the reach of next generation dark matter direct detection experiments*, *Phys. Rev.* **D89** (2014) 023524, [1307.5458].

[35] F. Ruppin, J. Billard, E. Figueroa-Feliciano and L. Strigari, *Complementarity of dark matter detectors in light of the neutrino background*, *Phys. Rev.* **D90** (2014) 083510, [1408.3581].

[36] SuperCDMS collaboration, R. Agnese et al., *New Results from the Search for Low-Mass Weakly Interacting Massive Particles with the CDMS Low Ionization Threshold Experiment*, *Phys. Rev. Lett.* **116** (2016) 071301, [1509.02448].

[37] SuperCDMS collaboration, R. Agnese et al., *First Dark Matter Constraints from a SuperCDMS Single-Charge Sensitive Detector*, *Phys. Rev. Lett.* **121** (2018) 051301, [1804.10697].

[38] SuperCDMS collaboration, D. W. Amaral et al., *Constraints on low-mass, relic dark matter candidates from a surface-operated SuperCDMS single-charge sensitive detector*, *Phys. Rev. D* **102** (2020) 091101, [2005.14067].

[39] G. Angloher et al., *Results from 730 kg days of the CRESST-II Dark Matter Search*, *Eur. Phys. J. C* **72** (2012) 1971, [1109.0702].

[40] CRESST collaboration, G. Angloher et al., *Results on light dark matter particles with a low-threshold CRESST-II detector*, *Eur. Phys. J. C* **76** (2016) 25, [1509.01515].

[41] R. Strauss et al., *A prototype detector for the CRESST-III low-mass dark matter search*, *Nucl. Instrum. Meth. A* **845** (2017) 414–417, [1802.08639].

[42] D. Carney, S. Ghosh, G. Krnjaic and J. M. Taylor, *Proposal for gravitational direct detection of dark matter*, *Phys. Rev. D* **102** (2020) 072003, [1903.00492].

[43] O. Buchmueller, C. Doglioni and L. T. Wang, *Search for dark matter at colliders*, *Nature Phys.* **13** (2017) 217–223, [1912.12739].

[44] LDMX collaboration, T. Åkesson et al., *Light Dark Matter eXperiment (LDMX)*, 1808.05219.

[45] B. Echenard, *Light Dark Matter Searches at Accelerators and the LDMX Experiment*, *Astrophys. Space Sci. Proc.* **56** (2019) 49–57.

[46] L. Carpenter, A. DiFranzo, M. Mulhearn, C. Shimmin, S. Tulin and D. Whiteson, *Mono-Higgs-boson: A new collider probe of dark matter*, *Phys. Rev. D* **89** (2014) 075017, [1312.2592].

[47] ATLAS collaboration, M. Aaboud et al., *Dark matter interpretations of ATLAS searches for the electroweak production of supersymmetric particles in $\sqrt{s} = 8$ TeV proton-proton collisions*, *JHEP* **09** (2016) 175, [1608.00872].

[48] CMS collaboration, A. M. Sirunyan et al., *Search for dark matter and unparticles in events with a Z boson and missing transverse momentum in proton-proton collisions at $\sqrt{s} = 13$ TeV*, *JHEP* **03** (2017) 061, [1701.02042].

[49] ATLAS collaboration, M. Aaboud et al., *Search for new phenomena in final states with an energetic jet and large missing transverse momentum in pp*

collisions at $\sqrt{s} = 13$ TeV using the ATLAS detector, *Phys. Rev. D* **94** (2016) 032005, [1604.07773].

[50] M. Fairbairn, J. Heal, F. Kahlhoefer and P. Tunney, *Constraints on Z' models from LHC dijet searches and implications for dark matter*, *JHEP* **09** (2016) 018, [1605.07940].

[51] K. K. Boddy et al., *Astrophysical and Cosmological Probes of Dark Matter*, in *2022 Snowmass Summer Study*, 3, 2022. 2203.06380.

[52] S. Ando et al., *Snowmass2021 Cosmic Frontier: Synergies between dark matter searches and multiwavelength/multimessenger astrophysics*, in *2022 Snowmass Summer Study*, 3, 2022. 2203.06781.

[53] A. Boyarsky, J. Franse, D. Iakubovskyi and O. Ruchayskiy, *Checking the Dark Matter Origin of a 3.53 keV Line with the Milky Way Center*, *Phys. Rev. Lett.* **115** (2015) 161301, [1408.2503].

[54] E. Bulbul, M. Markevitch, A. Foster, R. K. Smith, M. Loewenstein and S. W. Randall, *Detection of An Unidentified Emission Line in the Stacked X-ray spectrum of Galaxy Clusters*, *Astrophys. J.* **789** (2014) 13, [1402.2301].

[55] J. M. Cline and A. R. Frey, *Consistency of dark matter interpretations of the 3.5 keV x-ray line*, *Phys. Rev. D* **90** (2014) 123537, [1410.7766].

[56] P. Jean et al., *Early SPI / INTEGRAL measurements of 511 keV line emission from the 4th quadrant of the Galaxy*, *Astron. Astrophys.* **407** (2003) L55, [astro-ph/0309484].

[57] C. Boehm, D. Hooper, J. Silk, M. Casse and J. Paul, *MeV dark matter: Has it been detected?*, *Phys. Rev. Lett.* **92** (2004) 101301, [astro-ph/0309686].

[58] J.-H. Huh, J. E. Kim, J.-C. Park and S. C. Park, *Galactic 511 keV line from MeV milli-charged dark matter*, *Phys. Rev. D* **77** (2008) 123503, [0711.3528].

[59] R. Essig, E. Kuflik, S. D. McDermott, T. Volansky and K. M. Zurek, *Constraining Light Dark Matter with Diffuse X-Ray and Gamma-Ray Observations*, *JHEP* **11** (2013) 193, [1309.4091].

[60] K. K. Boddy and J. Kumar, *Indirect Detection of Dark Matter Using MeV-Range Gamma-Ray Telescopes*, *Phys. Rev. D* **92** (2015) 023533, [1504.04024].

[61] L. Goodenough and D. Hooper, *Possible Evidence For Dark Matter Annihilation In The Inner Milky Way From The Fermi Gamma Ray Space Telescope*, 0910.2998.

[62] T. Daylan, D. P. Finkbeiner, D. Hooper, T. Linden, S. K. N. Portillo, N. L. Rodd et al., *The characterization of the gamma-ray signal from the central Milky Way: A case for annihilating dark matter*, *Phys. Dark Univ.* **12** (2016) 1–23, [1402.6703].

[63] R. K. Leane and T. R. Slatyer, *Revival of the Dark Matter Hypothesis for the Galactic Center Gamma-Ray Excess*, *Phys. Rev. Lett.* **123** (2019) 241101, [1904.08430].

[64] Super-Kamiokande collaboration, T. Tanaka et al., *An Indirect Search for WIMPs in the Sun using 3109.6 days of upward-going muons in Super-Kamiokande*, *Astrophys. J.* **742** (2011) 78, [1108.3384].

[65] Super-Kamiokande collaboration, K. Choi et al., *Search for neutrinos from annihilation of captured low-mass dark matter particles in the Sun by Super-Kamiokande*, *Phys. Rev. Lett.* **114** (2015) 141301, [1503.04858].

[66] IceCube collaboration, M. G. Aartsen et al., *Search for dark matter annihilations in the Sun with the 79-string IceCube detector*, *Phys. Rev. Lett.* **110** (2013) 131302, [1212.4097].

[67] IceCube collaboration, M. G. Aartsen et al., *Search for annihilating dark matter in the Sun with 3 years of IceCube data*, *Eur. Phys. J. C* **77** (2017) 146, [1612.05949].

[68] M. Ardid, I. Felis, A. Herrero and J. A. Martínez-Mora, *Constraining Secluded Dark Matter models with the public data from the 79-string IceCube search for dark matter in the Sun*, *JCAP* **04** (2017) 010, [1701.08863].

[69] J. F. Acevedo, J. Bramante, A. Goodman, J. Kopp and T. Opferkuch, *Dark Matter, Destroyer of Worlds: Neutrino, Thermal, and Existential Signatures from Black Holes in the Sun and Earth*, *JCAP* **04** (2021) 026, [2012.09176].

[70] ANTARES collaboration, S. Adrian-Martinez et al., *First results on dark matter annihilation in the Sun using the ANTARES neutrino telescope*, *JCAP* **11** (2013) 032, [1302.6516].

[71] ANTARES collaboration, S. Adrián-Martínez et al., *A search for Secluded Dark Matter in the Sun with the ANTARES neutrino telescope*, *JCAP* **05** (2016) 016, [1602.07000].

[72] ANTARES collaboration, S. Adrian-Martinez et al., *Limits on Dark Matter Annihilation in the Sun using the ANTARES Neutrino Telescope*, *Phys. Lett. B* **759** (2016) 69–74, [1603.02228].

[73] S. Mohanty, S. Rao and D. P. Roy, *Relic density and PAMELA events in a heavy wino dark matter model with Sommerfeld effect*, *Int. J. Mod. Phys. A* **27** (2012) 1250025, [1009.5058].

[74] D. Hooper, T. Linden and P. Mertsch, *What Does The PAMELA Antiproton Spectrum Tell Us About Dark Matter?*, *JCAP* **03** (2015) 021, [1410.1527].

[75] B.-Q. Lu and H.-S. Zong, *Limits on dark matter from AMS-02 antiproton and positron fraction data*, *Phys. Rev. D* **93** (2016) 103517, [1510.04032].

[76] A. Reinert and M. W. Winkler, *A Precision Search for WIMPs with Charged Cosmic Rays*, *JCAP* **01** (2018) 055, [1712.00002].

[77] R. K. Leane et al., *Snowmass2021 Cosmic Frontier White Paper: Puzzling Excesses in Dark Matter Searches and How to Resolve Them*, 2203.06859.

[78] LIGO Scientific, Virgo collaboration, R. Abbott et al., *Population Properties of Compact Objects from the Second LIGO-Virgo Gravitational-Wave Transient Catalog*, *Astrophys. J. Lett.* **913** (2021) L7, [2010.14533].

[79] LIGO Scientific, VIRGO, KAGRA collaboration, R. Abbott et al., *The population of merging compact binaries inferred using gravitational waves through GWTC-3*, 2111.03634.

[80] A. K. Mehta, A. Buonanno, J. Gair, M. C. Miller, E. Farag, R. J. deBoer et al., *Observing Intermediate-mass Black Holes and the Upper Stellar-mass gap with LIGO and Virgo*, *Astrophys. J.* **924** (2022) 39, [2105.06366].

[81] Planck collaboration, P. A. R. Ade et al., *Planck 2015 results. XIII. Cosmological parameters*, *Astron. Astrophys.* **594** (2016) A13, [1502.01589].

[82] T. R. Slatyer, *Indirect dark matter signatures in the cosmic dark ages. I. Generalizing the bound on s-wave dark matter annihilation from Planck results*, *Phys. Rev. D* **93** (2016) 023527, [1506.03811].

[83] J. Stadler and C. Bœhm, *Constraints on γ-CDM interactions matching the Planck data precision*, *JCAP* **10** (2018) 009, [1802.06589].

[84] A. Kogut et al., *The Primordial Inflation Explorer (PIXIE): A Nulling Polarimeter for Cosmic Microwave Background Observations*, *JCAP* **07** (2011) 025, [1105.2044].

[85] DES collaboration, T. M. C. Abbott et al., *Dark Energy Survey Year 1 Results: Constraints on Extended Cosmological Models from Galaxy Clustering and Weak Lensing*, *Phys. Rev. D* **99** (2019) 123505, [1810.02499].

[86] HERA collaboration, Z. Abdurashidova et al., *HERA Phase I Limits on the Cosmic 21 cm Signal: Constraints on Astrophysics and Cosmology during the Epoch of Reionization*, *Astrophys. J.* **924** (2022) 51, [2108.07282].

[87] J. D. Bowman et al., *Science with the Murchison Widefield Array*, *Publ. Astron. Soc. Austral.* **30** (2013) e031, [1212.5151].

[88] A. Weltman et al., *Fundamental physics with the Square Kilometre Array*, *Publ. Astron. Soc. Austral.* **37** (2020) e002, [1810.02680].

[89] SKA collaboration, D. J. Bacon et al., *Cosmology with Phase 1 of the Square Kilometre Array: Red Book 2018: Technical specifications and performance forecasts*, *Publ. Astron. Soc. Austral.* **37** (2020) e007, [1811.02743].

[90] P. Tinyakov, M. Pshirkov and S. Popov, *Astroparticle Physics with Compact Objects*, *Universe* **7** (2021) 401, [2110.12298].

[91] R. A. Scalzo, A. J. Ruiter and S. A. Sim, *The ejected mass distribution of type Ia supernovae: A significant rate of non-Chandrasekhar-mass progenitors*, *Mon. Not. Roy. Astron. Soc.* **445** (2014) 2535–2544, [1408.6601].

[92] R. A. Scalzo et al., *Probing type Ia supernova properties using bolometric light curves from the Carnegie Supernova Project and the CfA Supernova Group*, *Mon. Not. Roy. Astron. Soc.* **483** (2019) 628, [1811.08969].

[93] K. Nomoto, *Accreting white dwarf models for type I supernovae. I - Presupernova evolution and triggering mechanisms*, *The Astrophysical Journal Letters* **253** (Feb., 1982) 798–810.

[94] Z.-W. Han and P. Podsiadlowski, *The single degenerate channel for the progenitors of type Ia supernovae*, *Mon. Not. Roy. Astron. Soc.* **350** (2004) 1301, [astro-ph/0309618].

[95] B. Wang, *Mass-accreting white dwarfs and type Ia supernovae*, *Res. Astron. Astrophys.* **18** (2018) 049, [1801.04031].

[96] A. Kashi and N. Soker, *A circumbinary disc in the final stages of common envelope and the core-degenerate scenario for type ia supernovae*, *Monthly Notices of the Royal Astronomical Society* **417** (2011) 1466–1479.

[97] D.-D. Liu, B. Wang, P. Podsiadlowski and Z. Han, *The violent white dwarf merger scenario for the progenitors of type ia supernovae*, *Monthly Notices of the Royal Astronomical Society* **461** (2016) 3653–3662.

[98] R. Pakmor, M. Kromer, S. Taubenberger and V. Springel, *Helium-ignited violent mergers as a unified model for normal and rapidly declining type ia supernovae*, *The Astrophysical Journal Letters* **770** (2013) L8.

[99] R. P. Olling, R. Mushotzky, E. J. Shaya, A. Rest, P. M. Garnavich, B. E. Tucker et al., *No signature of ejecta interaction with a stellar companion in three type Ia supernovae*, *Nature* **521** (May, 2015) 332–335.

[100] D. Maoz, F. Mannucci and G. Nelemans, *Observational clues to the progenitors of Type-Ia supernovae*, *Ann. Rev. Astron. Astrophys.* **52** (2014) 107–170, [1312.0628].

[101] J. Bramante, *Dark matter ignition of type Ia supernovae*, *Phys. Rev. Lett.* **115** (2015) 141301, [1505.07464].

[102] J. F. Acevedo and J. Bramante, *Supernovae Sparked By Dark Matter in White Dwarfs*, *Phys. Rev. D* **100** (2019) 043020, [1904.11993].

[103] R. Janish, V. Narayan and P. Riggins, *Type Ia supernovae from dark matter core collapse*, *Phys. Rev.* **D100** (2019) 035008, [1905.00395].

[104] P. W. Graham, R. Janish, V. Narayan, S. Rajendran and P. Riggins, *White Dwarfs as Dark Matter Detectors*, *Phys. Rev.* **D98** (2018) 115027, [1805.07381].

[105] M. A. Fedderke, P. W. Graham and S. Rajendran, *White dwarf bounds on charged massive particles*, *Phys. Rev. D* **101** (2020) 115021, [1911.08883].

[106] P. W. Graham, S. Rajendran and J. Varela, *Dark Matter Triggers of Supernovae*, *Phys. Rev.* **D92** (2015) 063007, [1505.04444].

[107] P. Montero-Camacho, X. Fang, G. Vasquez, M. Silva and C. M. Hirata, *Revisiting constraints on asteroid-mass primordial black holes as dark matter candidates*, *JCAP* **08** (2019) 031, [1906.05950].

[108] J. F. Acevedo, J. Bramante and A. Goodman, *Nuclear fusion inside dark matter*, *Phys. Rev. D* **103** (2021) 123022, [2012.10998].

[109] J. F. Acevedo, J. Bramante and A. Goodman, *Accelerating composite dark matter discovery with nuclear recoils and the Migdal effect*, *Phys. Rev. D* **105** (2022) 023012, [2108.10889].

[110] Y. C. Pan et al., *The Host Galaxies of Type Ia Supernovae Discovered by the Palomar Transient Factory*, *Mon. Not. Roy. Astron. Soc.* **438** (2014) 1391–1416, [1311.6344].

[111] P. Dufour, S. Blouin, S. Coutu, M. Fortin-Archambault, C. Thibeault, P. Bergeron et al., *The Montreal White Dwarf Database: A Tool for the*

Community, in *20th European White Dwarf Workshop* (P.-E. Tremblay, B. Gaensicke and T. Marsh, eds.), vol. 509 of *Astronomical Society of the Pacific Conference Series*, p. 3, Mar., 2017. `1610.00986`.

[112] C. Kouvaris and P. Tinyakov, *Constraining Asymmetric Dark Matter through observations of compact stars*, *Phys. Rev.* **D83** (2011) 083512, [`1012.2039`].

[113] J. Bramante and J. Unwin, *Superheavy Thermal Dark Matter and Primordial Asymmetries*, *JHEP* **02** (2017) 119, [`1701.05859`].

[114] M. Benito, A. Cuoco and F. Iocco, *Handling the Uncertainties in the Galactic Dark Matter Distribution for Particle Dark Matter Searches*, *JCAP* **1903** (2019) 033, [`1901.02460`].

[115] R. H. Helm, *Inelastic and Elastic Scattering of 187-Mev Electrons from Selected Even-Even Nuclei*, *Phys. Rev.* **104** (1956) 1466–1475.

[116] J. Lewin and P. Smith, *Review of mathematics, numerical factors, and corrections for dark matter experiments based on elastic nuclear recoil*, *Astroparticle Physics* **6** (1996) 87 – 112.

[117] G. Chabrier, *Quantum Effects in Dense Coulombic Matter: Application to the Cooling of White Dwarfs*, *Astrophysical Journal* **414** (Sep, 1993) 695.

[118] M. D. Jones and D. M. Ceperley, *Crystallization of the one-component plasma at finite temperature*, *Phys. Rev. Lett.* **76** (Jun, 1996) 4572–4575.

[119] C. Kittel, *Quantum Theory of Solids, Wiley.* 1987.

[120] D. A. Baiko, A. D. Kaminker, A. Y. Potekhin and D. G. Yakovlev, *Ion structure factors and electron transport in dense Coulomb plasmas*, *Phys. Rev. Lett.* **81** (1998) 5556–5559, [physics/9811052].

[121] D. A. Baiko, D. G. Yakovlev, H. E. De Witt and W. L. Slattery, *Coulomb crystals in the harmonic lattice approximation*, *Phys. Rev. E* **61** (2000) 1912–1919.

[122] S. Shapiro and S. Teukolsky, *Black holes, white dwarfs, and neutron stars: The physics of compact objects, New York, Wiley-Interscience*. 1983.

[123] J. Bramante, K. Fukushima and J. Kumar, *Constraints on bosonic dark matter from observation of old neutron stars*, *Phys. Rev.* **D87** (2013) 055012, [1301.0036].

[124] F. X. Timmes and S. E. Woosley, *The conductive propagation of nuclear flames. I - Degenerate C + O and O + NE + MG white dwarfs*, *Astrophys. J.* **396** (Sept., 1992) 649–667.

[125] A. Potekhin, D. Baiko, P. Haensel and D. Yakovlev, *Transport properties of degenerate electrons in neutron star envelopes and white dwarf cores*, *Astron.Astrophys.* **346** (1999) 345, [astro-ph/9903127].

[126] J. C. Niemeyer and S. E. Woosley, *The Thermonuclear explosion of Chandrasekhar-mass white dwarfs*, *Astrophys. J.* **475** (1997) 740, [astro-ph/9607032].

[127] M. Colpi, S. L. Shapiro and I. Wasserman, *Boson Stars: Gravitational Equilibria of Selfinteracting Scalar Fields*, *Phys. Rev. Lett.* **57** (1986) 2485–2488.

[128] C. Kouvaris and N. G. Nielsen, *Asymmetric Dark Matter Stars*, *Phys. Rev.* **D92** (2015) 063526, [1507.00959].

[129] M. I. Gresham and K. M. Zurek, *Asymmetric Dark Stars and Neutron Star Stability*, 1809.08254.

[130] C. Doran, A. Lasenby, S. Dolan and I. Hinder, *Fermion absorption cross section of a Schwarzschild black hole*, *Phys. Rev.* **D71** (2005) 124020, [gr-qc/0503019].

[131] J. H. MacGibbon and B. R. Webber, *Quark and gluon jet emission from primordial black holes: The instantaneous spectra*, *Phys. Rev.* **D41** (1990) 3052–3079.

[132] J. H. MacGibbon, *Quark and gluon jet emission from primordial black holes. 2. The Lifetime emission*, *Phys. Rev.* **D44** (1991) 376–392.

[133] D. N. Page, *Particle Emission Rates from a Black Hole. 3. Charged Leptons from a Nonrotating Hole*, *Phys. Rev.* **D16** (1977) 2402–2411.

[134] M. Autzen and C. Kouvaris, *Blocking the Hawking Radiation*, *Phys. Rev.* **D89** (2014) 123519, [1403.1072].

[135] P. K. Grieder, *Extensive Air Showers: High Energy Phenomena and Astrophysical Aspects - A Tutorial, Reference Manual and Data Book.* Springer, Berlin, Heidelberg, 2010.

[136] J. Bramante, T. Linden and Y.-D. Tsai, *Searching for dark matter with neutron star mergers and quiet kilonovae*, *Phys. Rev.* **D97** (2018) 055016, [1706.00001].

[137] M. McCullough and M. Fairbairn, *Capture of Inelastic Dark Matter in White Dwarves*, *Phys. Rev.* **D81** (2010) 083520, [1001.2737].

[138] S. Tulin, H.-B. Yu and K. M. Zurek, *Beyond Collisionless Dark Matter: Particle Physics Dynamics for Dark Matter Halo Structure*, *Phys. Rev.* **D87** (2013) 115007, [1302.3898].

[139] M. Kaplinghat, S. Tulin and H.-B. Yu, *Direct Detection Portals for Self-interacting Dark Matter*, *Phys. Rev.* **D89** (2014) 035009, [1310.7945].

[140] B. Holdom, *Two U(1)'s and Epsilon Charge Shifts*, *Phys. Lett.* **166B** (1986) 196–198.

[141] M. Pospelov, A. Ritz and M. B. Voloshin, *Secluded WIMP Dark Matter*, *Phys. Lett.* **B662** (2008) 53–61, [0711.4866].

[142] A. Bhoonah, J. Bramante, F. Elahi and S. Schon, *Galactic Center gas clouds and novel bounds on ultralight dark photon, vector portal, strongly interacting, composite, and super-heavy dark matter*, *Phys. Rev. D* **100** (2019) 023001, [1812.10919].

[143] J. Bramante, P. J. Fox, G. D. Kribs and A. Martin, *Inelastic frontier: Discovering dark matter at high recoil energy*, *Phys. Rev.* **D94** (2016) 115026, [1608.02662].

[144] APEX collaboration, S. Abrahamyan et al., *Search for a New Gauge Boson in Electron-Nucleus Fixed-Target Scattering by the APEX Experiment*, *Phys. Rev. Lett.* **107** (2011) 191804, [1108.2750].

[145] R. Essig et al., *Working Group Report: New Light Weakly Coupled Particles*, in *Proceedings, 2013 Community Summer Study on the Future of U.S. Particle Physics: Snowmass on the Mississippi (CSS2013): Minneapolis, MN, USA, July 29-August 6, 2013*, 2013. 1311.0029.

[146] NA48/2 collaboration, E. Goudzovski, *Search for the dark photon in π^0 decays by the NA48/2 experiment at CERN*, *EPJ Web Conf.* **96** (2015) 01017, [1412.8053].

[147] H. Merkel et al., *Search at the Mainz Microtron for Light Massive Gauge Bosons Relevant for the Muon g-2 Anomaly*, *Phys. Rev. Lett.* **112** (2014) 221802, [1404.5502].

[148] B. Batell, R. Essig and Z. Surujon, *Strong Constraints on Sub-GeV Dark Sectors from SLAC Beam Dump E137*, *Phys. Rev. Lett.* **113** (2014) 171802, [1406.2698].

[149] D. Curtin, R. Essig, S. Gori and J. Shelton, *Illuminating Dark Photons with High-Energy Colliders*, *JHEP* **02** (2015) 157, [1412.0018].

[150] A. Fradette, M. Pospelov, J. Pradler and A. Ritz, *Cosmological Constraints on Very Dark Photons*, *Phys. Rev.* **D90** (2014) 035022, [1407.0993].

[151] C. P. Burgess, M. Pospelov and T. ter Veldhuis, *The Minimal model of nonbaryonic dark matter: A Singlet scalar*, *Nucl. Phys.* **B619** (2001) 709–728, [hep-ph/0011335].

[152] M. J. Dolan, F. Kahlhoefer, C. McCabe and K. Schmidt-Hoberg, *A taste of dark matter: Flavour constraints on pseudoscalar mediators*, *JHEP* **03** (2015) 171, [1412.5174].

[153] A. Fradette, M. Pospelov, J. Pradler and A. Ritz, *Cosmological beam dump: constraints on dark scalars mixed with the Higgs boson*, *Phys. Rev.* **D99** (2019) 075004, [1812.07585].

[154] I. Goldman and S. Nussinov, *Weakly Interacting Massive Particles and Neutron Stars*, *Phys. Rev.* **D40** (1989) 3221–3230.

[155] A. Gould, B. T. Draine, R. W. Romani and S. Nussinov, *Neutron Stars: Graveyard of Charged Dark Matter*, *Phys. Lett.* **B238** (1990) 337–343.

[156] C. Kouvaris, *WIMP Annihilation and Cooling of Neutron Stars*, *Phys. Rev.* **D77** (2008) 023006, [0708.2362].

[157] G. Bertone and M. Fairbairn, *Compact Stars as Dark Matter Probes*, *Phys. Rev.* **D77** (2008) 043515, [0709.1485].

[158] A. de Lavallaz and M. Fairbairn, *Neutron Stars as Dark Matter Probes*, *Phys. Rev.* **D81** (2010) 123521, [1004.0629].

[159] C. Kouvaris and P. Tinyakov, *Can Neutron stars constrain Dark Matter?*, *Phys. Rev.* **D82** (2010) 063531, [1004.0586].

[160] S. D. McDermott, H.-B. Yu and K. M. Zurek, *Constraints on Scalar Asymmetric Dark Matter from Black Hole Formation in Neutron Stars*, *Phys. Rev.* **D85** (2012) 023519, [1103.5472].

[161] C. Kouvaris and P. Tinyakov, *Excluding Light Asymmetric Bosonic Dark Matter*, *Phys. Rev. Lett.* **107** (2011) 091301, [1104.0382].

[162] T. Guver, A. E. Erkoca, M. Hall Reno and I. Sarcevic, *On the capture of dark matter by neutron stars*, *JCAP* **1405** (2014) 013, [1201.2400].

[163] N. F. Bell, A. Melatos and K. Petraki, *Realistic neutron star constraints on bosonic asymmetric dark matter*, *Phys. Rev.* **D87** (2013) 123507, [1301.6811].

[164] J. Bramante, K. Fukushima, J. Kumar and E. Stopnitzky, *Bounds on self-interacting fermion dark matter from observations of old neutron stars*, *Phys. Rev. D* **89** (2014) 015010, [1310.3509].

[165] B. Bertoni, A. E. Nelson and S. Reddy, *Dark Matter Thermalization in Neutron Stars*, *Phys. Rev.* **D88** (2013) 123505, [1309.1721].

[166] M. Ángeles Pérez-García and J. Silk, *Constraining decaying dark matter with neutron stars*, *Phys. Lett. B* **744** (2015) 13–17, [1403.6111].

[167] M. Cermeno, M. Perez-Garcia and J. Silk, *Light dark matter scattering in outer neutron star crusts*, *Phys. Rev.* **D94** (2016) 063001, [1607.06815].

[168] R. Krall and M. Reece, *Last Electroweak WIMP Standing: Pseudo-Dirac Higgsino Status and Compact Stars as Future Probes*, *Chin. Phys. C* **42** (2018) 043105, [1705.04843].

[169] D. McKeen, A. E. Nelson, S. Reddy and D. Zhou, *Neutron stars exclude light dark baryons*, *Phys. Rev. Lett.* **121** (2018) 061802, [1802.08244].

[170] A. Joglekar, N. Raj, P. Tanedo and H.-B. Yu, *Relativistic capture of dark matter by electrons in neutron stars*, *Phys. Lett.* **B** (2020) 135767, [1911.13293].

[171] J. Bramante, B. J. Kavanagh and N. Raj, *Scattering searches for dark matter in subhalos: neutron stars, cosmic rays, and old rocks*, 2109.04582.

[172] M. Baryakhtar, J. Bramante, S. W. Li, T. Linden and N. Raj, *Dark Kinetic Heating of Neutron Stars and An Infrared Window On WIMPs, SIMPs, and Pure Higgsinos*, *Phys. Rev. Lett.* **119** (2017) 131801, [1704.01577].

[173] R. Nan, D. Li, C. Jin, Q. Wang, L. Zhu, W. Zhu et al., *The Five-Hundred Aperture Spherical Radio Telescope (fast) Project*, *International Journal of Modern Physics D* **20** (Jan., 2011) 989–1024, [1105.3794].

[174] J. F. Acevedo, J. Bramante, R. K. Leane and N. Raj, *Warming Nuclear Pasta with Dark Matter: Kinetic and Annihilation Heating of Neutron Star Crusts*, *JCAP* **03** (2020) 038, [1911.06334].

[175] S. B. Ruester, M. Hempel and J. Schaffner-Bielich, *The outer crust of non-accreting cold neutron stars*, *Phys. Rev.* **C73** (2006) 035804, [astro-ph/0509325].

[176] B. K. Sharma, M. Centelles, X. Vinas, M. Baldo and G. F. Burgio, *Unified equation of state for neutron stars on a microscopic basis*, *Astron. Astrophys.* **584** (2015) A103, [1506.00375].

[177] A. Y. Potekhin, A. F. Fantina, N. Chamel, J. M. Pearson and S. Goriely, *Analytical representations of unified equations of state for neutron-star matter*, *Astron. Astrophys.* **560** (2013) A48, [1310.0049].

[178] C. J. Pethick and D. G. Ravenhall, *Matter at large neutron excess and the physics of neutron-star crusts*, *Ann. Rev. Nucl. Part. Sci.* **45** (1995) 429–484.

[179] F. Douchin and P. Haensel, *Inner edge of neutron star crust with SLY effective nucleon-nucleon interactions*, *Phys. Lett.* **B485** (2000) 107–114, [astro-ph/0006135].

[180] C. J. Pethick, N. Chamel and S. Reddy, *Superfluid dynamics in neutron star crusts*, *Prog. Theor. Phys. Suppl.* **186** (2010) 9–16, [1009.2303].

[181] D. G. Ravenhall, C. J. Pethick and J. R. Wilson, *Structure of Matter Below Nuclear Saturation Density*, *Phys. Rev. Lett.* **50** (1983) 2066–2069.

[182] R. D. Williams and S. E. Koonin, *Sub-saturation phases of nuclear matter*, *Nucl. Phys.* **A435** (1985) 844–858.

[183] C. P. Lorenz, D. G. Ravenhall and C. J. Pethick, *Neutron star crusts*, *Phys. Rev. Lett.* **70** (1993) 379–382.

[184] K. Oyamatsu, *Nuclear shapes in the inner crust of a neutron star*, *Nucl. Phys.* **A561** (1993) 431–452.

[185] S. Goriely, N. Chamel and J. M. Pearson, *Further explorations of Skyrme-Hartree-Fock-Bogoliubov mass formulas. XII: Stiffness and stability of neutron-star matter*, *Phys. Rev. C* **82** (2010) 035804, [1009.3840].

[186] N. Chamel, *Effective contact pairing forces from realistic calculations in infinite homogeneous nuclear matter*, *Phys. Rev. C* **82** (2010) 014313, [1007.0873].

[187] D. Page and S. Reddy, *Dense Matter in Compact Stars: Theoretical Developments and Observational Constraints*, *Ann. Rev. Nucl. Part. Sci.* **56** (2006) 327–374, [astro-ph/0608360].

[188] J. B. Hartle, R. F. Sawyer and D. J. Scalapino, *Pion condensed matter at high densities: equation of state and stellar models.*, *Astrophysical Journal* **199** (Jul, 1975) 471–481.

[189] P. Haensel and M. Proszynski, *Pion condensation in cold dense matter and neutron stars*, *Astrophysical Journal* **258** (Jul, 1982) 306–320.

[190] G. Brown and W. Weise, *Pion condensates*, *Physics Reports* **27** (1976) 1 – 34.

[191] B. Holdom, J. Ren and C. Zhang, *Quark matter may not be strange*, *Phys. Rev. Lett.* **120** (2018) 222001, [1707.06610].

[192] D. D. Ivanenko and D. F. Kurdgelaidze, *Hypothesis concerning quark stars*, *Astrophysics* **1** (Oct, 1965) 251–252.

[193] D. Ivanenko and D. F. Kurdgelaidze, *Remarks on quark stars*, *Lettere al Nuovo Cimento (1969-1970)* **2** (Jul, 1969) 13–16.

[194] J. C. Collins and M. J. Perry, *Superdense Matter: Neutrons Or Asymptotically Free Quarks?*, *Phys. Rev. Lett.* **34** (1975) 1353.

[195] F. Weber, *Quark matter in neutron stars*, *J. Phys.* **G25** (1999) R195–R229.

[196] R. Lastowiecki, D. Blaschke, T. Fischer and T. Klähn, *Quark matter in high-mass neutron stars?*, *Physics of Particles and Nuclei* **46** (Sep, 2015) 843–845.

[197] D. Chatterjee and I. Vidaña, *Do hyperons exist in the interior of neutron stars?*, *Eur. Phys. J.* **A52** (2016) 29, [1510.06306].

[198] M. G. Alford, K. Rajagopal and F. Wilczek, *Color flavor locking and chiral symmetry breaking in high density QCD*, *Nucl. Phys.* **B537** (1999) 443–458, [hep-ph/9804403].

[199] M. G. Alford, A. Schmitt, K. Rajagopal and T. Schafer, *Color superconductivity in dense quark matter*, *Rev. Mod. Phys.* **80** (2008) 1455–1515, [0709.4635].

[200] N. K. Glendenning and S. Pei, *Crystalline structure of the mixed confined - deconfined phase in neutron stars*, *Phys. Rev.* **C52** (1995) 2250–2253.

[201] P. F. Bedaque and T. Schafer, *High density quark matter under stress*, *Nucl. Phys.* **A697** (2002) 802–822, [hep-ph/0105150].

[202] D. B. Kaplan and S. Reddy, *Novel phases and transitions in color flavor locked matter*, *Phys. Rev.* **D65** (2002) 054042, [hep-ph/0107265].

[203] H. T. Cromartie et al., *Relativistic Shapiro delay measurements of an extremely massive millisecond pulsar*, 1904.06759.

[204] J. Rikovska-Stone, P. A. M. Guichon, H. H. Matevosyan and A. W. Thomas, *Cold uniform matter and neutron stars in the quark-mesons-coupling model*, *Nucl. Phys.* **A792** (2007) 341–369, [nucl-th/0611030].

[205] P. Haensel, M. Bejger, M. Fortin and L. Zdunik, *Rotating neutron stars with exotic cores: masses, radii, stability*, *Eur. Phys. J.* **A52** (2016) 59, [1601.05368].

[206] T. F. Motta, A. W. Thomas and P. A. Guichon, *Do Delta Baryons Play a Role in Neutron Stars?*, 1906.05459.

[207] M. Pato, F. Iocco and G. Bertone, *Dynamical constraints on the dark matter distribution in the Milky Way*, *JCAP* **12** (2015) 001, [1504.06324].

[208] D. Page, J. M. Lattimer, M. Prakash and A. W. Steiner, *Minimal cooling of neutron stars: A New paradigm*, *Astrophys. J. Suppl.* **155** (2004) 623–650, [astro-ph/0403657].

[209] D. G. Yakovlev and C. J. Pethick, *Neutron star cooling*, *Ann. Rev. Astron. Astrophys.* **42** (2004) 169–210, [astro-ph/0402143].

[210] D. Gonzalez and A. Reisenegger, *Internal heating of old neutron stars: contrasting different mechanisms*, *Astronomy & Astrophysics* **522** (Oct, 2010) A16.

[211] K. Hamaguchi, N. Nagata and K. Yanagi, *Dark Matter Heating vs. Rotochemical Heating in Old Neutron Stars*, *Phys. Lett.* **B795** (2019) 484–489, [1905.02991].

[212] N. Chamel and P. Haensel, *Physics of neutron star crusts*, *Living Reviews in Relativity* **11** (Dec, 2008) 10.

[213] P. Haensel, A. Y. Potekhin and D. G. Yakovlev, *Neutron stars 1: Equation of state and structure*, *Astrophys. Space Sci. Libr.* **326** (2007) pp.1–619.

[214] C. Misner, K. Thorne and J. Wheeler, *Gravitation.* W. H. Freeman, 1973.

[215] X. Roca-Maza and J. Piekarewicz, *Impact of the symmetry energy on the outer crust of non-accreting neutron stars*, *Phys. Rev.* **C78** (2008) 025807, [0805.2553].

[216] D. A. Baiko, D. G. Yakovlev, H. E. de Witt and W. L. Slattery, *Coulomb crystals in the harmonic lattice approximation*, *Phys. Rev. E* **61** (Feb, 2000) 1912–1919, [physics/9912048].

[217] L. G. Cao, U. Lombardo and P. Schuck, *Screening effects in superfluid nuclear and neutron matter within Brueckner theory*, *Phys. Rev.* **C74** (2006) 064301, [nucl-th/0608005].

[218] J. Bardeen, L. N. Cooper and J. R. Schrieffer, *Theory of superconductivity*, *Phys. Rev.* **108** (1957) 1175–1204.

[219] J. Kundu and S. Reddy, *Neutrino scattering off pair-breaking and collective excitations in superfluid neutron matter and in color-flavor locked quark matter*, *Phys. Rev.* **C70** (2004) 055803, [nucl-th/0405055].

[220] B. Bertoni, S. Reddy and E. Rrapaj, *Electron-neutron scattering and transport properties of neutron stars*, *Phys. Rev.* **C91** (2015) 025806, [1409.7750].

[221] A. Schwenk and B. Friman, *Polarization contributions to the spin dependence of the effective interaction in neutron matter*, *Phys. Rev. Lett.* **92** (2004) 082501, [nucl-th/0307089].

[222] A. Gezerlis, C. J. Pethick and A. Schwenk, *Pairing and superfluidity of nucleons in neutron stars*, 1406.6109.

[223] N. Chamel, D. Page and S. Reddy, *Low-energy collective excitations in the neutron star inner crust*, *Phys. Rev.* **C87** (2013) 035803, [1210.5169].

[224] L. S. Brown and G. Gabrielse, *Geonium Theory: Physics of a Single Electron or Ion in a Penning Trap*, *Rev. Mod. Phys.* **58** (1986) 233.

[225] P. Magierski and P.-H. Heenen, *Structure of the inner crust of neutron stars: Crystal lattice or disordered phase?*, *Phys. Rev.* **C65** (2002) 045804, [nucl-th/0112018].

[226] P. Gogelein and H. Muther, *Nuclear matter in the crust of neutron stars*, *Phys. Rev.* **C76** (2007) 024312, [0704.1984].

[227] H. Sonoda, G. Watanabe, K. Sato, K. Yasuoka and T. Ebisuzaki, *Phase diagram of nuclear "pasta" and its uncertainties in supernova cores*, *Phys. Rev.* **C77** (2008) 035806, [0712.0052].

[228] K. Iida, G. Watanabe and K. Sato, *Formation of nuclear 'pasta' in cold neutron star matter*, *Prog. Theor. Phys.* **106** (2001) 551–559, [nucl-th/0108034].

[229] G. Watanabe, *Understanding nuclear 'pasta': Current status and future prospects*, *AIP Conf. Proc.* **891** (2007) 373–381, [nucl-th/0610116].

[230] A. S. Schneider, C. J. Horowitz, J. Hughto and D. K. Berry, *Nuclear ?pasta? formation*, *Phys. Rev.* **C88** (2013) 065807, [1307.1678].

[231] A. da Silva Schneider, M. E. Caplan, D. K. Berry and C. J. Horowitz, *Domains and defects in nuclear pasta*, *Phys. Rev.* **C98** (2018) 055801, [1807.00102].

[232] M. E. Caplan, A. S. Schneider and C. J. Horowitz, *Elasticity of Nuclear Pasta*, *Phys. Rev. Lett.* **121** (2018) 132701, [1807.02557].

[233] R. Nandi and S. Schramm, *Transport Properties of the Nuclear Pasta Phase with Quantum Molecular Dynamics*, *Astrophys. J.* **852** (2018) 135, [1709.09793].

[234] R. Garani, Y. Genolini and T. Hambye, *New Analysis of Neutron Star Constraints on Asymmetric Dark Matter*, 1812.08773.

[235] J. M. Pearson, N. Chamel, A. Y. Potekhin, A. F. Fantina, C. Ducoin, A. K. Dutta et al., *Unified equations of state for cold non-accreting neutron stars with Brussels-Montreal functionals - I. Role of symmetry energy*, *Mon. Not. Roy. Astron. Soc.* **481** (2018) 2994–3026, [1903.04981].

[236] CRESST collaboration, G. Angloher et al., *Results on light dark matter particles with a low-threshold CRESST-II detector*, *Eur. Phys. J.* **C76** (2016) 25, [1509.01515].

[237] DEAP collaboration, R. Ajaj et al., *Search for dark matter with a 231-day exposure of liquid argon using DEAP-3600 at SNOLAB*, *Phys. Rev.* **D100** (2019) 022004, [1902.04048].

[238] DarkSide collaboration, P. Agnes et al., *Low-Mass Dark Matter Search with the DarkSide-50 Experiment*, *Phys. Rev. Lett.* **121** (2018) 081307, [1802.06994].

[239] PICO collaboration, C. Amole et al., *Dark Matter Search Results from the Complete Exposure of the PICO-60 C_3F_8 Bubble Chamber*, *Phys. Rev.* **D100** (2019) 022001, [1902.04031].

[240] A. L. Erickcek, P. J. Steinhardt, D. McCammon and P. C. McGuire, *Constraints on the Interactions between Dark Matter and Baryons from the X-ray Quantum Calorimetry Experiment*, *Phys. Rev.* **D76** (2007) 042007, [0704.0794].

[241] V. Gluscevic and K. K. Boddy, *Constraints on Scattering of keV?TeV Dark Matter with Protons in the Early Universe*, *Phys. Rev. Lett.* **121** (2018) 081301, [1712.07133].

[242] W. L. Xu, C. Dvorkin and A. Chael, *Probing sub-GeV Dark Matter-Baryon Scattering with Cosmological Observables*, *Phys. Rev.* **D97** (2018) 103530, [1802.06788].

[243] C. V. Cappiello, K. C. Y. Ng and J. F. Beacom, *Reverse Direct Detection: Cosmic Ray Scattering With Light Dark Matter*, *Phys. Rev.* **D99** (2019) 063004, [1810.07705].

[244] T. Bringmann and M. Pospelov, *Novel direct detection constraints on light dark matter*, *Phys. Rev. Lett.* **122** (2019) 171801, [1810.10543].

[245] R. V. Reid, Jr., *Local phenomenological nucleon-nucleon potentials*, *Annals Phys.* **50** (1968) 411–448.

[246] E. Witten, *Cosmic Separation of Phases*, *Phys. Rev.* **D30** (1984) 272–285.

[247] A. Zacchi, R. Stiele and J. Schaffner-Bielich, *Compact stars in a SU(3) Quark-Meson Model*, *Phys. Rev.* **D92** (2015) 045022, [1506.01868].

[248] G. G. Raffelt, *Stars as laboratories for fundamental physics, Chicago, Univ. Pr.* 1996.

[249] B. Batell, M. Pospelov, A. Ritz and Y. Shang, *Solar Gamma Rays Powered by Secluded Dark Matter*, *Phys. Rev.* **D81** (2010) 075004, [0910.1567].

[250] P. Schuster, N. Toro and I. Yavin, *Terrestrial and Solar Limits on Long-Lived Particles in a Dark Sector*, *Phys. Rev.* **D81** (2010) 016002, [0910.1602].

[251] P. Schuster, N. Toro, N. Weiner and I. Yavin, *High Energy Electron Signals from Dark Matter Annihilation in the Sun*, *Phys. Rev.* **D82** (2010) 115012, [0910.1839].

[252] P. Meade, S. Nussinov, M. Papucci and T. Volansky, *Searches for Long Lived Neutral Particles*, *JHEP* **06** (2010) 029, [0910.4160].

[253] N. F. Bell and K. Petraki, *Enhanced neutrino signals from dark matter annihilation in the Sun via metastable mediators*, *JCAP* **1104** (2011) 003, [1102.2958].

[254] J. L. Feng, J. Smolinsky and P. Tanedo, *Dark Photons from the Center of the Earth: Smoking-Gun Signals of Dark Matter*, *Phys. Rev.* **D93** (2016) 015014, [1509.07525].

[255] J. L. Feng, J. Smolinsky and P. Tanedo, *Detecting dark matter through dark photons from the Sun: Charged particle signatures*, *Phys. Rev.* **D93** (2016) 115036, [1602.01465].

[256] R. K. Leane, K. C. Y. Ng and J. F. Beacom, *Powerful Solar Signatures of Long-Lived Dark Mediators*, *Phys. Rev.* **D95** (2017) 123016, [1703.04629].

[257] HAWC collaboration, A. Albert et al., *Constraints on Spin-Dependent Dark Matter Scattering with Long-Lived Mediators from TeV Observations of the Sun with HAWC*, *Phys. Rev.* **D98** (2018) 123012, [1808.05624].

[258] N. F. Bell, Y. Cai, J. B. Dent, R. K. Leane and T. J. Weiler, *Enhancing Dark Matter Annihilation Rates with Dark Bremsstrahlung*, *Phys. Rev.* **D96** (2017) 023011, [1705.01105].

[259] M. Cermeno and M. A. Perez-Garcia, *Gamma rays from dark mediators in white dwarfs*, *Phys. Rev.* **D98** (2018) 063002, [1807.03318].

[260] M. U. Nisa, J. F. Beacom, S. Y. BenZvi, R. K. Leane, T. Linden, K. C. Y. Ng et al., *The Sun at GeV–TeV Energies: A New Laboratory for Astroparticle Physics*, 1903.06349.

[261] C. Niblaeus, A. Beniwal and J. Edsjo, *Neutrinos and gamma rays from long-lived mediator decays in the Sun*, *JCAP* **1911** (2019) 011, [1903.11363].

[262] R. K. Leane, T. Linden, P. Mukhopadhyay and N. Toro, *Celestial-Body Focused Dark Matter Annihilation Throughout the Galaxy*, *Phys. Rev. D* **103** (2021) 075030, [2101.12213].

[263] Y. Cui, M. Pospelov and J. Pradler, *Signatures of Dark Radiation in Neutrino and Dark Matter Detectors*, *Phys. Rev.* **D97** (2018) 103004, [1711.04531].

[264] J. F. Cherry, M. T. Frandsen and I. M. Shoemaker, *Direct Detection Phenomenology in Models Where the Products of Dark Matter Annihilation Interact with Nuclei*, *Phys. Rev. Lett.* **114** (2015) 231303, [1501.03166].

[265] D. McKeen and N. Raj, *Monochromatic dark neutrinos and boosted dark matter in noble liquid direct detection*, *Phys. Rev.* **D99** (2019) 103003, [1812.05102].

[266] D. Tucker-Smith and N. Weiner, *Inelastic dark matter*, *Phys. Rev.* **D64** (2001) 043502, [hep-ph/0101138].

[267] K. R. Dienes, J. Kumar, B. Thomas and D. Yaylali, *Overcoming Velocity Suppression in Dark-Matter Direct-Detection Experiments*, *Phys. Rev.* **D90** (2014) 015012, [1312.7772].

[268] N. F. Bell, G. Busoni and S. Robles, *Heating up Neutron Stars with Inelastic Dark Matter*, *JCAP* **1809** (2018) 018, [1807.02840].

[269] N. Arkani-Hamed, A. Delgado and G. F. Giudice, *The Well-tempered neutralino*, *Nucl. Phys.* **B741** (2006) 108–130, [hep-ph/0601041].

[270] R. J. Hill and M. P. Solon, *Standard Model anatomy of WIMP dark matter direct detection I: weak-scale matching*, *Phys. Rev.* **D91** (2015) 043504, [1401.3339].

[271] J. Hisano, K. Ishiwata, N. Nagata and T. Takesako, *Direct Detection of Electroweak-Interacting Dark Matter*, *JHEP* **07** (2011) 005, [1104.0228].

[272] G. Krnjaic and K. Sigurdson, *Big Bang Darkleosynthesis*, *Phys. Lett. B* **751** (2015) 464–468, [1406.1171].

[273] M. B. Wise and Y. Zhang, *Yukawa Bound States of a Large Number of Fermions*, *JHEP* **02** (2015) 023, [1411.1772].

[274] M. I. Gresham, H. K. Lou and K. M. Zurek, *Nuclear Structure of Bound States of Asymmetric Dark Matter*, *Phys. Rev. D* **96** (2017) 096012, [1707.02313].

[275] M. I. Gresham, H. K. Lou and K. M. Zurek, *Early Universe synthesis of asymmetric dark matter nuggets*, *Phys. Rev. D* **97** (2018) 036003, [1707.02316].

[276] D. M. Grabowska, T. Melia and S. Rajendran, *Detecting Dark Blobs*, *Phys. Rev. D* **98** (2018) 115020, [1807.03788].

[277] K. K. Boddy, J. L. Feng, M. Kaplinghat and T. M. P. Tait, *Self-Interacting Dark Matter from a Non-Abelian Hidden Sector*, *Phys. Rev. D* **89** (2014) 115017, [1402.3629].

[278] A. Soni and Y. Zhang, *Hidden SU(N) Glueball Dark Matter*, *Phys. Rev. D* **93** (2016) 115025, [1602.00714].

[279] A. R. Zhitnitsky, *'Nonbaryonic' dark matter as baryonic color superconductor*, *JCAP* **10** (2003) 010, [hep-ph/0202161].

[280] Y. Bai, A. J. Long and S. Lu, *Dark Quark Nuggets*, *Phys. Rev. D* **99** (2019) 055047, [1810.04360].

[281] M. Ricotti and A. Gould, *A New Probe of Dark Matter and High-Energy Universe Using Microlensing*, *Astrophys. J.* **707** (2009) 979–987, [0908.0735].

[282] J. Barranco and A. Bernal, *Self-gravitating system made of axions*, *Phys. Rev. D* **83** (2011) 043525, [1001.1769].

[283] A. H. Guth, M. P. Hertzberg and C. Prescod-Weinstein, *Do Dark Matter Axions Form a Condensate with Long-Range Correlation?*, *Phys. Rev. D* **92** (2015) 103513, [1412.5930].

[284] J. Eby, P. Suranyi, C. Vaz and L. C. R. Wijewardhana, *Axion Stars in the Infrared Limit*, *JHEP* **03** (2015) 080, [1412.3430].

[285] E. Braaten, A. Mohapatra and H. Zhang, *Dense Axion Stars*, *Phys. Rev. Lett.* **117** (2016) 121801, [1512.00108].

[286] Y. Bai, V. Barger and J. Berger, *Hydrogen Axion Star: Metallic Hydrogen Bound to a QCD Axion BEC*, *JHEP* **12** (2016) 127, [1612.00438].

[287] E. Braaten, A. Mohapatra and H. Zhang, *Emission of Photons and Relativistic Axions from Axion Stars*, *Phys. Rev. D* **96** (2017) 031901, [1609.05182].

[288] L. Visinelli, S. Baum, J. Redondo, K. Freese and F. Wilczek, *Dilute and dense axion stars*, *Phys. Lett. B* **777** (2018) 64–72, [1710.08910].

[289] D. A. Feinblum and W. A. McKinley, *Stable States of a Scalar Particle in Its Own Gravational Field*, *Phys. Rev.* **168** (1968) 1445.

[290] P.-H. Chavanis, *Mass-radius relation of Newtonian self-gravitating Bose-Einstein condensates with short-range interactions: I. Analytical results*, *Phys. Rev. D* **84** (2011) 043531, [1103.2050].

[291] J. Eby, C. Kouvaris, N. G. Nielsen and L. C. R. Wijewardhana, *Boson Stars from Self-Interacting Dark Matter*, *JHEP* **02** (2016) 028, [1511.04474].

[292] F. Kling and A. Rajaraman, *Towards an Analytic Construction of the Wavefunction of Boson Stars*, *Phys. Rev. D* **96** (2017) 044039, [1706.04272].

[293] S. R. Coleman, *Q-balls*, *Nucl. Phys. B* **262** (1985) 263.

[294] C. V. Cappiello, J. I. Collar and J. F. Beacom, *New experimental constraints in a new landscape for composite dark matter*, *Phys. Rev. D* **103** (2021) 023019, [2008.10646].

[295] J. F. Acevedo, J. Bramante and A. Goodman, *Old Rocks, New Limits: Excavated Ancient Mica Searches ForDark Matter*, 2105.06473.

[296] R. Ebadi et al., *Ultraheavy dark matter search with electron microscopy of geological quartz*, *Phys. Rev. D* **104** (2021) 015041, [2105.03998].

[297] M. B. Wise and Y. Zhang, *Stable Bound States of Asymmetric Dark Matter*, *Phys. Rev. D* **90** (2014) 055030, [1407.4121].

[298] M. I. Gresham, H. K. Lou and K. M. Zurek, *Astrophysical Signatures of Asymmetric Dark Matter Bound States*, *Phys. Rev. D* **98** (2018) 096001, [1805.04512].

[299] J. Walecka, *Theoretical nuclear and subnuclear physics*, vol. 16. 1995.

[300] E. Hardy, R. Lasenby, J. March-Russell and S. M. West, *Big Bang Synthesis of Nuclear Dark Matter*, *JHEP* **06** (2015) 011, [1411.3739].

[301] I. Affleck and M. Dine, *A New Mechanism for Baryogenesis*, *Nucl. Phys.* **B249** (1985) 361–380.

[302] M. Dine, L. Randall and S. D. Thomas, *Baryogenesis from flat directions of the supersymmetric standard model*, *Nucl. Phys.* **B458** (1996) 291–326, [hep-ph/9507453].

[303] W. Greiner, *Relativistic quantum mechanics: Wave equations*. 1990.

[304] A. B. Migdal, *Qualitative Methods in Quantum Theory*, vol. 48. 1977.

[305] L. D. Landau and E. Lifshits, *Quantum Mechanics: Non-Relativistic Theory*, vol. v.3 of *Course of Theoretical Physics*. Butterworth-Heinemann, Oxford, 1991.

[306] A. Joglekar, N. Raj, P. Tanedo and H.-B. Yu, *Dark kinetic heating of neutron stars from contact interactions with relativistic targets*, *Phys. Rev. D* **102** (2020) 123002, [2004.09539].

[307] L. Landau, *The Classical Theory of Fields*. Course of theoretical physics. Elsevier Science, 2013.

[308] M. Cannoni, *Lorentz invariant relative velocity and relativistic binary collisions*, *Int. J. Mod. Phys. A* **32** (2017) 1730002, [1605.00569].

[309] J. D. Vergados and H. Ejiri, *The role of ionization electrons in direct neutralino detection*, *Phys. Lett. B* **606** (2005) 313–322, [hep-ph/0401151].

[310] C. Moustakidis, J. Vergados and H. Ejiri, *Direct dark matter detection by observing electrons produced in neutralino-nucleus collisions*, *Nucl. Phys. B* **727** (2005) 406–420, [hep-ph/0507123].

[311] H. Ejiri, C. Moustakidis and J. Vergados, *Dark matter search by exclusive studies of X-rays following WIMPs nuclear interactions*, *Phys. Lett. B* **639** (2006) 218–222, [hep-ph/0510042].

[312] R. Bernabei et al., *On electromagnetic contributions in WIMP quests*, *Int. J. Mod. Phys. A* **22** (2007) 3155–3168, [0706.1421].

[313] M. Ibe, W. Nakano, Y. Shoji and K. Suzuki, *Migdal Effect in Dark Matter Direct Detection Experiments*, *JHEP* **03** (2018) 194, [1707.07258].

[314] M. J. Dolan, F. Kahlhoefer and C. McCabe, *Directly detecting sub-GeV dark matter with electrons from nuclear scattering*, *Phys. Rev. Lett.* **121** (2018) 101801, [1711.09906].

[315] R. Essig, J. Pradler, M. Sholapurkar and T.-T. Yu, *Relation between the Migdal Effect and Dark Matter-Electron Scattering in Isolated Atoms and Semiconductors*, *Phys. Rev. Lett.* **124** (2020) 021801, [1908.10881].

[316] D. Baxter, Y. Kahn and G. Krnjaic, *Electron Ionization via Dark Matter-Electron Scattering and the Migdal Effect*, *Phys. Rev. D* **101** (2020) 076014, [1908.00012].

[317] G. Grilli di Cortona, A. Messina and S. Piacentini, *Migdal effect and photon Bremsstrahlung: improving the sensitivity to light dark matter of liquid argon experiments*, *JHEP* **11** (2020) 034, [2006.02453].

[318] C. P. Liu, C.-P. Wu, H.-C. Chi and J.-W. Chen, *Model-independent determination of the Migdal effect via photoabsorption*, *Phys. Rev. D* **102** (2020) 121303, [2007.10965].

[319] V. V. Flambaum, L. Su, L. Wu and B. Zhu, *Constraining sub-GeV dark matter from Migdal and Boosted effects*, 2012.09751.

[320] S. Knapen, J. Kozaczuk and T. Lin, "The Migdal effect in semiconductors." 11, 2020.

[321] N. F. Bell, J. B. Dent, B. Dutta, S. Ghosh, J. Kumar and J. L. Newstead, *Low-mass inelastic dark matter direct detection via the Migdal effect*, *Phys. Rev. D* **104** (2021) 076013, [2103.05890].

[322] N. F. Bell, J. B. Dent, R. F. Lang, J. L. Newstead and A. C. Ritter, *Observing the Migdal effect from nuclear recoils of neutral particles with liquid xenon and argon detectors*, 2112.08514.

[323] F. Iocco, M. Pato, G. Bertone and P. Jetzer, *Dark Matter distribution in the Milky Way: microlensing and dynamical constraints*, *JCAP* **11** (2011) 029, [1107.5810].

[324] J. I. Read, *The Local Dark Matter Density*, *J. Phys. G* **41** (2014) 063101, [1404.1938].

[325] G. R. Beardsmore and J. P. Cull, *Crustal heat flow: a guide to measurement and modelling*. Cambridge University Press, 2001.

[326] J. Bramante, B. Broerman, R. F. Lang and N. Raj, *Saturated Overburden Scattering and the Multiscatter Frontier: Discovering Dark Matter at the Planck Mass and Beyond*, *Phys. Rev. D* **98** (2018) 083516, [1803.08044].

[327] J. Bramante, B. Broerman, J. Kumar, R. F. Lang, M. Pospelov and N. Raj, *Foraging for dark matter in large volume liquid scintillator neutrino detectors with multiscatter events*, *Phys. Rev. D* **99** (2019) 083010, [1812.09325].

[328] M. Clark, A. Depoian, B. Elshimy, A. Kopec, R. F. Lang and J. Qin, *Direct Detection Limits on Heavy Dark Matter*, *Phys. Rev. D* **102** (2020) 123026, [2009.07909].

[329] A. Bhoonah, J. Bramante, B. Courtman and N. Song, *Etched plastic searches for dark matter*, *Phys. Rev. D* **103** (2021) 103001, [2012.13406].

[330] R. Bernabei et al., *Extended limits on neutral strongly interacting massive particles and nuclearites from NaI(Tl) scintillators*, *Phys. Rev. Lett.* **83** (1999) 4918–4921.

[331] E. Hardy and R. Lasenby, *Stellar cooling bounds on new light particles: plasma mixing effects*, *JHEP* **02** (2017) 033, [1611.05852].

[332] S. Knapen, T. Lin and K. M. Zurek, *Light Dark Matter: Models and Constraints*, *Phys. Rev. D* **96** (2017) 115021, [1709.07882].

[333] S. Orito et al., *Search for supermassive relics with 2000-m**2 array of plastic track detector*, *Phys. Rev. Lett.* **66** (1991) 1951–1954.

[334] J. Bramante, J. Kumar and N. Raj, *Dark matter astrometry at underground detectors with multiscatter events*, *Phys. Rev. D* **100** (2019) 123016, [1910.05380].

[335] W. Lotz, *Electron-Impact Ionization Cross-Sections and Ionization Rate Coefficients for Atoms and Ions*, *Zeitschrift für Physik* **14** (May, 1967) 207.

[336] G. Massacrier, A. Potekhin and G. Chabrier, *Equation of state for partially ionized carbon and oxygen mixtures at high temperatures*, *Phys. Rev. E* **84** (2011) 056406, [1111.0532].

[337] T. Padmanabhan, *Theoretical Astrophysics*, vol. 1. Cambridge University Press, 2000.

[338] G. R. Caughlan and W. A. Fowler, *Thermonuclear reaction rates. 5.*, *Atom. Data Nucl. Data Tabl.* **40** (1988) 283–334.

[339] J. Bramante, A. Buchanan, A. Goodman and E. Lodhi, *Terrestrial and Martian Heat Flow Limits on Dark Matter*, *Phys. Rev. D* **101** (2020) 043001, [1909.11683].

[340] IceCube collaboration, M. Aartsen et al., *The IceCube Neutrino Observatory: Instrumentation and Online Systems*, *JINST* **12** (2017) P03012, [1612.05093].

[341] Borexino collaboration, G. Bellini et al., *Final results of Borexino Phase-I on low energy solar neutrino spectroscopy*, *Phys. Rev. D* **89** (2014) 112007, [1308.0443].

[342] SNO+ collaboration, S. Andringa et al., *Current Status and Future Prospects of the SNO+ Experiment*, *Adv. High Energy Phys.* **2016** (2016) 6194250, [1508.05759].

[343] R. Kippenhahn, A. Weigert and A. Weiss, *Stellar structure and evolution*, vol. 9783642303043. Springer, 8, 2012, 10.1007/978-3-642-30304-3.

[344] P. J. Schinder, D. N. Schramm, P. J. Wiita, S. H. Margolis and D. L. Tubbs, *Neutrino Emission by the Pair, Plasma, and Photo Processes in the Weinberg-Salam Model*, *Astrophysical Journal* **313** (Feb., 1987) 531.

[345] N. Itoh, T. Adachi, M. Nakagawa, Y. Kohyama and H. Munakata, *Neutrino Energy Loss in Stellar Interiors. III. Pair, Photo-, Plasma, and Bremsstrahlung Processes*, *Astrophysical Journal* **339** (Apr., 1989) 354.

[346] N. Itoh, H. Hayashi, A. Nishikawa and Y. Kohyama, *Neutrino Energy Loss in Stellar Interiors. VII. Pair, Photo-, Plasma, Bremsstrahlung, and Recombination Neutrino Processes*, *Astrophysical Journal Supplement* **102** (Feb., 1996) 411.

[347] L. Gasques, A. Afanasjev, E. Aguilera, M. Beard, L. Chamon, P. Ring et al., *Nuclear fusion in dense matter: Reaction rate and carbon burning*, *Phys. Rev. C* **72** (2005) 025806, [astro-ph/0506386].

[348] D. g. Yakovlev, L. R. Gasques, M. Beard, M. Wiescher and A. V. Afanasjev, *Fusion reactions in multicomponent dense matter*, *Phys. Rev. C* **74** (2006) 035803, [astro-ph/0608488].

[349] S. Toonen, M. Hollands, B. T. Gänsicke and T. Boekholt, *The binarity of the local white dwarf population*, *Astronomy & Astrophysics* **602** (June, 2017) A16, [1703.06893].

[350] D. Maoz, N. Hallakoun and C. Badenes, *The separation distribution and merger rate of double white dwarfs: improved constraints*, *Mon. Not. Roy. Astron. Soc.* **476** (2018) 2584–2590, [1801.04275].

[351] K. D. Temmink, S. Toonen, E. Zapartas, S. Justham and B. T. Gänsicke, *Looks can be deceiving. Underestimating the age of single white dwarfs due to binary mergers*, *Astronomy & Astrophysics* **636** (Apr., 2020) A31, [1910.05335].

[352] S.-C. Yoon, P. Podsiadlowski and S. Rosswog, *Remnant evolution after a carbon-oxygen white dwarf merger*, *Mon. Not. Roy. Astron. Soc.* **380** (2007) 933, [0704.0297].

[353] P. Loren-Aguilar, J. Isern and E. Garcia-Berro, *High-resolution Smoothed Particle Hydrodynamics simulations of the merger of binary white dwarfs*, *AIP Conf. Proc.* **1122** (2009) 320–323, [0903.4599].

[354] L. Decin, W. Homan, T. Danilovich, A. de Koter, D. Engels, L. B. F. M. Waters et al., *Reduction of the maximum mass-loss rate of OH/IR stars due to unnoticed binary interaction*, *Nature Astronomy* **3** (Feb., 2019) 408–415, [1902.09259].

[355] L. G. Althaus, P. Gil-Pons, A. H. Córsico, M. Miller Bertolami, F. De Gerónimo, M. E. Camisassa et al., *The formation of ultra-massive*

carbon-oxygen core white dwarfs and their evolutionary and pulsational properties, *Astronomy & Astrophysics* **646** (Feb., 2021) A30, [2011.10439].

[356] I. Dominguez, O. Straniero, A. Tornambe and J. Isern, *On the Formation of Massive C-O White Dwarfs: The Lifting Effect of Rotation*, *Astrophysical Journal* **472** (Dec., 1996) 783.

[357] M. Kawasaki, H. Murayama and T. Yanagida, *Can the strongly interacting dark matter be a heating source of Jupiter?*, *Prog. Theor. Phys.* **87** (1992) 685–692.

[358] S. Mitra, *Uranus' anomalously low excess heat constrains strongly interacting dark matter*, *Phys. Rev. D* **70** (2004) 103517, [astro-ph/0408341].

[359] G. D. Mack, J. F. Beacom and G. Bertone, *Towards Closing the Window on Strongly Interacting Dark Matter: Far-Reaching Constraints from Earth's Heat Flow*, *Phys. Rev. D* **76** (2007) 043523, [0705.4298].

[360] S. L. Adler, *Planet-bound dark matter and the internal heat of Uranus, Neptune, and hot-Jupiter exoplanets*, *Phys. Lett. B* **671** (2009) 203–206, [0808.2823].

[361] B. Chauhan and S. Mohanty, *Constraints on leptophilic light dark matter from internal heat flux of Earth*, *Phys. Rev. D* **94** (2016) 035024, [1603.06350].

[362] R. Garani and P. Tinyakov, *Constraints on Dark Matter from the Moon*, *Phys. Lett. B* **804** (2020) 135403, [1912.00443].

[363] M. H. Chan and C. M. Lee, *Constraining the spin-independent elastic scattering cross section of dark matter using the Moon as a detection target*

and the background neutrino data, *Phys. Rev. D* **102** (2020) 023024, [2007.01589].

[364] R. K. Leane and J. Smirnov, *Exoplanets as Sub-GeV Dark Matter Detectors*, *Phys. Rev. Lett.* **126** (2021) 161101, [2010.00015].

[365] R. K. Leane and T. Linden, *First Analysis of Jupiter in Gamma Rays and a New Search for Dark Matter*, 2104.02068.

[366] D. L. Williams, R. P. Von Herzen, J. G. Sclater and R. N. Anderson, *The Galapagos Spreading Centre: Lithospheric Cooling and Hydrothermal Circulation**, *Geophysical Journal International* **38** (09, 1974) 587–608.

[367] C. R. B. Lister, J. G. Sclater, E. E. Davis, H. Villinger and S. Nagihara, *Heat flow maintained in ocean basins of great age: investigations in the north-equatorial West Pacific*, *Geophysical Journal International* **102** (09, 1990) 603–630.

[368] J. Buch, S. C. J. Leung and J. Fan, *Using Gaia DR2 to Constrain Local Dark Matter Density and Thin Dark Disk*, *JCAP* **04** (2019) 026, [1808.05603].

[369] J. W. Morgan and E. Anders, *Chemical composition of earth, venus, and mercury*, *Proceedings of the National Academy of Sciences* **77** (1980) 6973–6977.

[370] A. M. Dziewonski and D. L. Anderson, *Preliminary reference earth model*, *Phys. Earth Planet. Interiors* **25** (1981) 297–356.

[371] H. S. Wang, C. H. Lineweaver and T. R. Ireland, *The elemental abundances (with uncertainties) of the most earth-like planet*, *Icarus* **299** (2018) 460 – 474.

[372] W. McDonough, *2.15 - compositional model for the earth's core*, in *Treatise on Geochemistry* (H. D. Holland and K. K. Turekian, eds.), pp. 547 – 568. Pergamon, Oxford, 2003. DOI.

[373] J. Bramante, A. Delgado and A. Martin, *Multiscatter stellar capture of dark matter*, *Phys. Rev.* **D96** (2017) 063002, [1703.04043].

[374] J. R. Primack, D. Seckel and B. Sadoulet, *Detection of Cosmic Dark Matter*, *Ann. Rev. Nucl. Part. Sci.* **38** (1988) 751–807.

[375] R. H. Helm, *Inelastic and elastic scattering of 187-mev electrons from selected even-even nuclei*, *Phys. Rev.* **104** (Dec, 1956) 1466–1475.

Appendix A

Multi-Scatter Dark Matter Capture

In this Appendix, we provide further detail on the computation of the capture rate for dark matter transiting white dwarfs, in the limit that dark matter requires multiple scatters to slow down to sub-escape velocity. This is required to derive the results in Ch. 2, since there we considered dark matter masses in excess of 10^6 GeV. Although the same treatment is applicable for neutron stars, for the mass range we consider in Ch. 3, this treatment is unnecessary compared to the single-scatter capture limit.

Following Ref. [373], the total dark matter capture rate is expressed as

$$C_X = \sum_{N=1}^{\infty} C_N. \tag{A.1}$$

Where each C_N term in the sum corresponds to the capture rate for dark matter that underwent N scatters before losing sufficient energy to become gravitationally bound to the white dwarf star (with C_1 correctly reproducing the single-scatter limit). Note that, depending on the mass of the dark matter and its velocity in the halo, there will be a minimum number of scatters required in order to capture the dark matter.

Each of these terms is given by

$$C_N = \pi R^2 p_N(\tau)\sqrt{\frac{6}{\pi}}\frac{n_X}{\bar{v}}\left[(2\bar{v}^2 + 3v_{esc}^2) - (2\bar{v}^2 + 3v_N^2)\exp\left(-\frac{3(v_N^2 - v_{esc}^2)}{2\bar{v}^2}\right)\right]. \quad \text{(A.2)}$$

Here R is the radius of the star, n_X the dark matter halo number density, v_{esc} is the escape velocity from the star surface ($v_{esc} \ll 1$) and $\bar{v}$ is the average halo speed of dark matter. The quantity v_N is defined as $v_{esc}(1 - \beta_+/2)^{-N/2}$ with $\beta_+ = 4m_X m_a/(m_X + m_a)^2$, and it accounts for the energy loss in successive momentum exchanges as a particle undergoes N scatters. The function

$$p_N(\tau) = 2\int_0^1 dy\ \frac{ye^{-y\tau}\,(y\tau)^N}{N!}, \quad \text{(A.3)}$$

is a Poisson weighting that gives the probability of N scatters in the star for stellar optical depth $\tau \equiv 3\sigma_{aX}M/(2\pi R^2 m_a)$, where $y = \cos\theta$ defines the angle at which the dark matter entering the star and M is the white dwarf mass, σ_{aX} is the dark matter nuclear scattering cross-section, R is the radius of the white dwarf, and m_a is the mass of a nucleus in the white dwarf, see Ref. [373]. The optical depth is proportional to the ratio between the dark matter-nuclei cross section and the saturation cross section for which a dark matter particle typically scatters about once as it traverses a travels through the star, $\sigma_{sat} \equiv \pi R^2 M/m_a$. We assume the fraction of energy lost in a collision follows a uniform distribution over $0 < \Delta E/E_0 < \beta_+$, where E_0 is the initial energy carried by the dark matter particle in the star's rest frame. Let us emphasize that, although the capture rate is proportional to the area projected by the star, it also depends on the optical depth which includes the information about interactions between dark matter and the stellar constituents and scales as

R^{-2}. Therefore, multiscatter capture is more relevant for more compact stars.

Expression (A.2) is valid for capture in white dwarfs; the exact capture rate depends on the white dwarf's composition. Here we conservatively assume the inner composition of white dwarfs is predominantly ^{12}C nuclei. Dark matter possessing spin-independent interactions (*e.g.* a vector or scalar current) will coherently scatter off the nucleons within these nuclei for low energy exchanges. In contrast, at higher energies and momentum exchange, the scattering cross-section becomes suppressed as the dark matter begins to scatter with individual nucleons. To account for this, we make the following substitution for the dark matter-nuclear cross section, which determines the optical depth τ,

$$\sigma_{aX} \ \rightarrow \ \sigma'_{aX} = A^2 \left(\frac{\mu_{aX}}{\mu_{nX}}\right)^2 S(q) F^2(\langle E_R \rangle) \ \sigma_{nX}, \tag{A.4}$$

where σ_{aX} is the dark matter-nuclear cross section for a nucleus with A nucleons, written in terms of the dark matter-nucleon cross section σ_{nX} (here assumed to be velocity-independent), μ_{aX} is the dark matter-nuclear reduced mass, and μ_{nX} is the dark matter-nucleon reduced mass. The function $S(q)$ is the static structure factor that accounts for correlation effects in an ion lattice, and depends on the momentum transfer $q \simeq m_a\sqrt{2E/m_X}$, in the limit $m_a \ll m_X$. For the recoil energies involved during capture, however, it evaluates to unity. This structure factor becomes relevant for both thermalization and gravitational collapse of the captured dark matter, which we discuss below. The second factor $F^2(\langle E_R \rangle)$ is the Helm form factor [374, 375, 116] evaluated at the average recoil energy

$$\langle E_R \rangle \equiv \frac{\int_0^{E_R^{max}} E \; F^2(E) \; dE}{\int_0^{E_R^{max}} F^2(E) \; dE} \simeq 1 \text{ MeV} \tag{A.5}$$

for heavy dark matter scattering off ^{12}C at velocity $v_{esc} \simeq 10^{-2}$, making the average Helm form factor correction of order ~ 0.5. Momentum exchanges with recoil energies much in excess of $\sim$ MeV are suppressed by this form factor. To account for the Helm form factor in the energy loss expression, we replace the factor of 1/2 that multiplies β_+ in v_N by $\langle E_R \rangle / E_R^{Max}$, where $E_R^{Max} = 4 m_a v_{esc}^2$ is the maximum recoil energy. Applying these corrections to (A.2), and truncating (A.1) at a sufficiently large value of N such that the higher order terms removed are negligible, we arrive at the capture rate for heavy dark matter passing through white dwarfs.

Appendix B

Composite Dark Matter Stopping through Dissipation Processes

In this Appendix, we detail how a dark matter composite state slows down due to nuclei losing kinetic energy from various dissipation processes occurring in their interior. As discussed in the main text, the stopping of the composite state as it travels through matter is paramount to determine the parameter space that can be probed by an underground experiment, as well as the potential astrophysical signatures of the model. The stopping process can be understood from considering momentum and energy conservation: if a nucleus loses kinetic energy while transiting the composite, then when it exits the composite its momentum will be more aligned with the direction of motion of the composite. The net result is that the dark matter composite slows down. Below we confirm that the decrease in dark matter composite kinetic energy matches the kinetic energy transferred to the nucleus inside the composite, in the non-relativistic limit considered in this work. This treatment will be specific to the case that nuclei are accelerated by an attractive potential inside the dark matter composite – in the case of a repulsive potential, standard two body kinematics apply.

Let us consider a single nucleus entering the composite volume while the composite moves through a given stellar (or planetary) medium with an initial speed v_i in the stellar rest frame. In what follows, we assume the center-of-mass (CM) frame for this system is equivalent to the composite rest frame, since we are always in the limit $m_N \ll M_X$. Upon acceleration from the composite potential, energy conservation in the CM frame reads

$$\frac{1}{2}m_N v_i^2 = \frac{1}{2}m_N v_N^2 + \varphi, \tag{B.1}$$

where v_N is the velocity of the nucleus after accelerating to the final kinetic energy and $\varphi < 0$ is the potential energy, with $|\varphi| \ll m_N$ in the non-relativistic limit, *cf.* Eq. (4.15). In the stellar rest frame, this velocity is $(v_N)_{\rm sta} = v_i - (v_i - 2\varphi/m_N)^{1/2}$, and momentum conservation imposes

$$M_X v_i = M_X(v_X)_{\rm sta} + m_N(v_N)_{\rm sta}. \tag{B.2}$$

This yields a velocity for the composite after the nucleus has accelerated given by $(v_X)_{\rm sta} = v_i - (m_N/M_X)\left(v_i - (v_i - 2\varphi/m_N)^{1/2}\right)$. Note that since $m_N \ll M_X$, the composite barely recoils in the process.

As discussed in the main text, the nucleus can undergo several inelastic processes while inside the composite state that reduce its kinetic energy by an amount we denote here by $\delta E < 0$. Furthermore, we assume $|\delta E| \ll |\varphi|$, which is the case throughout this work. If $\delta E \sim \varphi$ then the nucleus would remain bound to the composite and the analysis below would be different. Upon deceleration, energy conservation in the CM frame now is,

$$\frac{1}{2}m_N(v_N')^2 + \varphi = \frac{1}{2}m_N(v_N'')^2, \tag{B.3}$$

where the velocity v_N' now is related to v_N above via $\delta E = (m_N/2)(v_N'^2 - v_N^2)$. Then, $v_N' = -\left(v_N^2 + 2\delta E/m_N\right)^{1/2} = -\left(v_i^2 + 2(\delta E - \varphi)/m_N\right)^{1/2}$, and we solve for v_N'' in the above equation to obtain $v_N'' = -\left(v_i^2 + 2\delta E/m_N\right)^{1/2}$. Boosting back to the stellar rest frame, conservation of momentum now requires

$$M_X(v_X)_{\rm sta} + m_N(v_N')_{\rm sta} = M_X(v_X')_{\rm sta} + m_N(v_N'')_{\rm sta}, \tag{B.4}$$

where the unknown velocity above is $(v_X')_{\rm sta}$. The two velocities computed above in the stellar rest frame are $(v_N')_{\rm sta} = v_i - \left(v_i^2 + 2(\delta E - \varphi)/m_N\right)^{1/2}$ and $(v_N'')_{\rm sta} = v_i - \left(v_i^2 + 2\delta E/m_N\right)^{1/2}$. Solving for $(v_X')_{\rm sta}$ above yields,

$$(v_X')_{\rm sta} - v_i = \frac{m_N}{M_X}\left(v_i - \left(v_i + \frac{2(\delta E - \varphi)}{m_N}\right)^{1/2} - v_i + \left(v_i^2 - \frac{2\varphi}{m_N}\right)^{1/2} - v_i + \left(v_i^2 + \frac{2\delta E}{m_N}\right)^{1/2}\right) \tag{B.5}$$

In the limit $|\delta E| \ll |\varphi|$, the first four terms on the right hand side cancel out. Similarly, we can expand $\left(v_i^2 + 2\delta E/m_N\right)^{1/2} = v_i\left(1 + 2\delta E/m_N v_i^2\right)^{1/2} \simeq v_i(1 + \delta E/m_N v_i^2)$ in the limit $|\delta E| \ll m_N v_i^2$. Therefore,

$$(v_X')_{\rm sta} - v_i \simeq \frac{\delta E}{M_X v_i}. \tag{B.6}$$

Squaring this expression and multiplying by $M_X/2$ yields,

$$\frac{1}{2}M_X(v_X')^2_{\rm sta} = \frac{1}{2}M_X\left(v_i + \frac{\delta E}{M_X v_i}\right)^2 \simeq \frac{1}{2}M_X\left(v_i^2 + \frac{2\delta E}{M_X}\right) \tag{B.7}$$

Thus, in the stellar rest frame, the kinetic energy of the composite is reduced by

$$\frac{1}{2}M_X(v_X')^2_{\rm sta} - \frac{1}{2}M_X v_i^2 \simeq \delta E < 0. \tag{B.8}$$

This result implies that for nuclei traveling through an attractive potential inside a dark matter composite, any dissipation processes that contribute to its cool down, such as heat conduction, radiation or endothermic reactions, will continuously decrease the dark matter composite kinetic energy, as viewed in the stellar rest frame. On the other hand, if there are processes that reheat the nuclei, such as exothermic nuclear reactions, the stopping power would be subsequently reduced.